Superconducting proximity effect in monocrystalline bismuth nanowires

Anil Murani

To cite this version:

Anil Murani. Superconducting proximity effect in monocrystalline bismuth nanowires. Quantum Physics [quant-ph]. Université Paris Saclay (COmUE), 2017. English. NNT : 2017SACLS093 . tel-02057273

HAL Id: tel-02057273
https://theses.hal.science/tel-02057273

Submitted on 5 Mar 2019

NNT : 2017SACLS093

THÈSE DE DOCTORAT DE L'UNIVERSITÉ PARIS-SACLAY PRÉPARÉE À L'UNIVERSITÉ PARIS SUD, AU LABORATOIRE DE PHYSIQUE DES SOLIDES

Ecole doctorale n°564
Physique en Île de France
Spécialité de doctorat : Physique
par

M. ANIL MURANI

Supraconductivité par effet de proximité dans des nanofils de bismuth monocrystallins

Thèse présentée et soutenue à Orsay, le 12 Avril 2017.

Composition du Jury :

M.	CRISTIAN URBINA	Directeur de recherche CEA Saclay	(Président du jury)
M.	CHARLES M. MARCUS	Professeur Niels Bohr Institute	(Rapporteur)
M.	WOLFGANG BELZIG	Professeur Université de Konstanz	(Rapporteur)
M.	MANUEL HOUZET	Directeur de recherche CEA Grenoble	(Examinateur)
M.	TRISTAN MEUNIER	Chargé de recherche Institut Néel	(Examinateur)
M.	BENOÎT FAUQUÉ	Chargé de recherche ESPCI	(Examinateur)
Mme	HÉLÈNE BOUCHIAT	Directrice de recherche Laboratoire de Physique des Solides	(Directrice de thèse)
Mme	SOPHIE GUÉRON	Directrice de recherche Laboratoire de Physique des Solides	(Codirectrice de thèse)

Remerciements

Mes remerciements s'adressent tout d'abord au groupe MESO, chez qui j'ai passé mes trois années de thèse, dans le cadre le plus agréable que peut souhaiter un doctorant. Tout d'abord je souhaite remercier Hélène, pour m'avoir proposé un sujet de thèse original quand j'ai poussé la porte du labo pour la première fois, et puis de l'avoir encadrée avec bienveillance. Les discussions de physique avec toi sont toujours passionnantes, ta culture semble intarrissable. Je dois également admettre que ton intuition est souvent très juste, meme si on a pu avoir de longs débats, que ce soit sur des questions comme la règle de somme ou bien sur les élections présidentielles. Par ailleurs, tu n'as jamais compté ton temps pour donner un coup de main, à moi comme à d'autres, que ce soit pour un transfert d'Helium, une soudure, ou un conseil. Merci à Sophie, ton énergie et ta motivation sont capables de venir à bout de toutes les misères qui pouvaient arriver aux échantillons. Tu as su seconder Hélène dans cette lourde tache qu'a du etre de m'encadrer, et grace a tes conseils et tes encouragements, la nanofabrication était comme un jeu, que ce soit pour la lithographie ou bien pour transférer du graphène (paf). Je me souviendrai longtemps que tu ne m'as pas laissé mourir de faim, alors que j'avais été oublié au sous-sol en train d'installer l'IBE, et que l'heure d'aller à la cantine était passé ! Un grand merci à Alik, tu es non seulement un expert dans la fabrication de nanofils, mais aussi du FIB, grace à quoi nous avons pu les mesurer. Ce n'est cependant qu'une partie infime de ton talent, et je ne connais pas d'égals à ta virtuosité et à ta créativité dans l'art de la nanofabrication. Et de plus, ta bonne humeur et ton sens de l'humour ont toujours accompagné nos repas ou bien nos excursions au CSNSM. Merci à Richard, tu as toujours su répondre aux questions qu'on te posait avec des explications à la fois précises, concises et perspicaces. Ta clarté d'esprit est telle que tu es la seule personne dont je puisse lire le code labview protéiforme sans m'arracher les cheveux. Merci aussi énormément pour m'avoir aidé à déménager ! Many thanks to Shamashis, it was a pleasure to share some projects and ideas with you, as well as the office for the last part. I especially appreciated your joy to share the indian food you brought. I also really enjoyed the discussions with you on subjects varying from correlated materials to indian politics. I wish you good luck for your new position at CSNSM ! Merci à Alexei, qui est arrivé au labo au moment où je démarrais ma thèse. Tu m'as beaucoup appris, et je garde bien en mémoire ta technique imparable pour régler un PID. Merci aussi pour les milles services rendus. Merci à Meydi et Bastien, car meme si vous etes partis au tout début de ma thèse et revenus à la toute fin, j'ai pu quand meme vous croiser et discuter avec vous lors de vos visites au labo ou autres congrés. Votre interet pour les manips qui se déroulaient à Orsay était toujours moteur, merci pour les questions et conseils. Merci à Chuan, je te dois beaucoup. Tu m'as beaucoup inspiré, et ta force pour fermer les Lleybolds fera école j'espère, ils n'avaient qu'a bien se tenir. Merci à Raphaelle d'avoir partagé le bureau avec moi pendant la majeure partie de ma thèse. S'il y a probablement moins de yaks qu'au Ladakh, j'espère que la Suisse saura te convenir, au moins le chocolat (au lait) y a bonne réputation ! Merci a Taro, qui a toujours été sympa dans toutes les circonstances. Tu as été le parfait compagnon de cordée pendant l'été quand nous étions seuls à faire tourner les manips dans le labo. Et puis, merci à Sandrine et aussi à Jean-Pierre, grace à vous j'ai eu la chance d'assister à la fabrication d'une dilu maison de A a Z, et aussi d'avoir fait partie des premiers à l'utiliser !

Ces remerciements ne sauraient etre complets si il n'incluaient pas les nombreux chercheurs, étudiants, ingénieurs, techniciens et personnels du LPS et d'ailleurs avec qui j'ai pu interagir, et dont la contribution a été importante pour cette thèse. Ils sont nombreux, et je souffre ne pas pouvoir tous les nommer ici. Parmi eux, je remercie en particulier Frank Fortuna pour la sympathie et le grand talent au FIB, Julien Gabelli pour m'avoir toujours secouru micro-ondément, Tom Dvir pour m'avoir mis la puce a l'oreille sur l'EBSD, Francois Brisset pour avoir fait de l'EBSD sur nos puces, Raphael Weil pour son grand talent, Aris Alexandradinata pour me dire que simuler du Bismuth ce n'est pas la mer a boire, Alberto Zobelli pour m'avoir laissé utiliser le cluster. Laissez moi encore remercier : Francesca, Charis, Julien Basset, Marco Aprili, Jérome Estève, Pierre Février, Cyril, Alexis, Mathieu, Gianluca, Freek, Marko, Miguel, Emilie, Pascale Sanzier, Gilles Guillier, Sambat, Marie-France, Sam, Diyana, Alena, Tom, Alexandre, Camille, Audrey, Pascal Simon, Christophe Texier, Mark Goerbig, Gilles Montambaux, Marc Gabay, Marcello Civelli, Jean-Noel Fuchs, Jérome Cayssol, Francois Konschelle, Christina Bena, Julia Meyer, Manuel Houzet, Vincent Bouchiat, Mathieu Kociak, Landry, Jean-Damien, Benjamin Huard, Philippe Joyez et Hugues Pothier.

Pour finir, je remercie mes proches qui m'ont toujours témoigné leur soutien qu'il soient mes amis d'enfance à Claix, Seyssins, Echirolles, Grenoble, Toulouse, Amsterdam, Paris ou ailleurs : Thomas, Mickael, Alix, Margaux, Benoit, Adrien, Amélie, Lulutte, Louise, Rudy, Macha, Esther, Mathieu S, Fredo, Arnaud S, Arnaud M, Vincent, Lena, Zbyszek, Arnaud B, Paul, Neven, Baptiste, Ari, Benjamin, Felix, Martin, David, Mathieu, Lise K/, Alex, Constance, Yonglong et tous les autres. Enfin, merci a mes grandes soeurs et a mes parents pour leur bonté infinie, et merci a ma très chère Ania qui partage et égaye ma vie.

Résumé

Dans cette thèse je me suis interessé au transport électronique à l'échelle mésoscopique dans des nanofils monocrystallins de Bismuth et d'Argent. Le terme mésoscopique signifie que l'on considère des nanofils de “grande” taille, pouvant mesurer typiquement quelques micromètres de longueur, mais où pourtant la mécanique quantique joue un role important.

Diffusion électronique et effet de taille finie dans des nanofils monocristallins

Les matériaux étudiés ici ont des propriétés électroniques assez différentes. L'Argent est un métal plutot standard, la longueur d'onde de Fermi des électrons vaut typiquement une fraction de nanomètre. Au contraire, le Bismuth est semi-métallique, ce qui signifie que la longueur d'onde de Fermi λ_F est beaucoup plus grande en volume (50 nm) qu'en surface (1 nm). Par conséquent un nanofil de Bismuth de 100 nm de diamètre aura jusqu'à 200 fois plus de canaux de conduction surfaciques que de canaux de conduction volumiques.

Malgré le fait que ces nanofils soient tous des monocristaux ne contenant que très peu d'impuretés (moins d'un ppm), leurs propriétés de transport éléctronique à basse température se révèlent décevantes. En effet, pour différents nanofils de longueur croissante, la résistance augmente proportionnellement. Or pour obtenir cela, il est nécessaire que les électrons subissent un très grand nombre de collisions afin d'équilibrer le potentiel éléctrostatique uniformément dans le fil. Autrement dit ces nanofils obéissent à la loi d'Ohm, avec un libre parcours moyen qui s'avère être dans tous les cas à peine plus grand que la dimension transverse des fils (fig 1A,B). Nous expliquons cela par l'inévitable rugosité présente à la surface des fils, due par exemple à l'oxidation. Les collisions électroniques avec la surface sont alors nombreuses et après une distance de l'ordre du diamètre du nanofil, la vitesse initiale du paquet d'onde électronique est perdue : on dit que les éléctrons sont diffusifs. Dans le Bismuth, nous avons observé de façon similaire que les électrons sont diffusifs (fig 1C). Or ceux-ci étant majoritairement des canaux surfaciques, cette conclusion ne peut s'appliquer qu'à ces derniers. D'autre part, les canaux volumiques ayant une longueur d'onde de Fermi plus grande qu'en surface, on pourrait penser qu'ils sont moins affectés par le désordre que les états surfaciques, car le désordre serait moyenné. Nous avons montré qu'en réalité ce n'est pas le cas grâce à la mesure des oscillations quantiques de la résistance à fort champ magnétique dans nos nanofils. Ces oscillations sont le résultat d'interférences quantiques se produisant lorsque le rayon cyclotron $r_C = mv_F/eB$ est de l'ordre d'un multiple de λ_F, et sont d'autant plus prononcées que le champ est fort

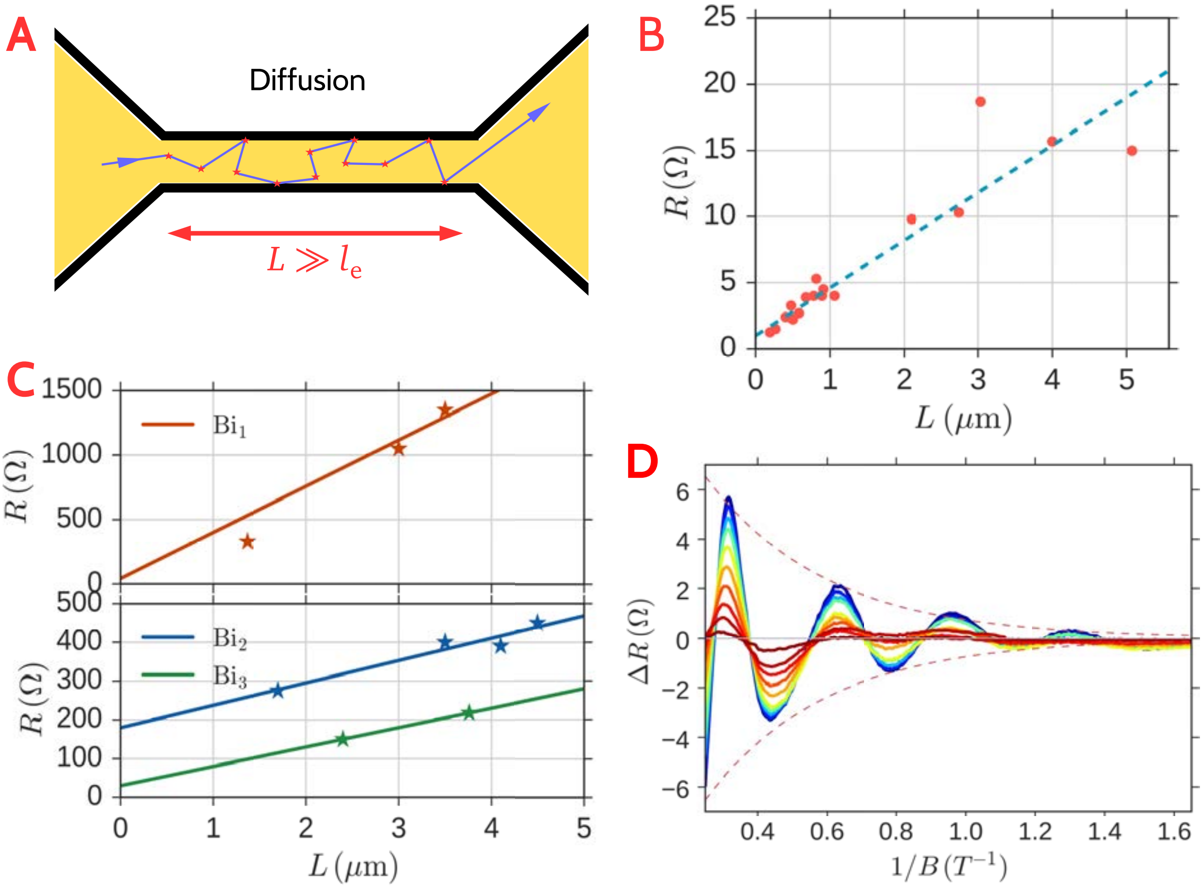

Figure 1: Diffusion par effet de taille finie dans les nanofils monocristallins d'Argent et de Bismuth. A : Lorsque les électrons subissent de multiples collisions, leur comportement est diffusif. La résistance est alors proportionnelle à la longueur. B : Résistance en fonction de la longueur dans les nanofils d'Argent. Le libre parcours moyen $l_e \simeq 70\,\mathrm{nm}$ est proche de leur diamètre $\varnothing \simeq 50\,\mathrm{nm}$. C : Résistance en fonction de la longueur dans les nanofils de Bismuth. Le libre parcours moyen $l_e \simeq 200\,\mathrm{nm}$ est proche de leur diamètre $\varnothing \simeq 150\,\mathrm{nm}$. D : Oscillations quantiques de la résistance dans les nanofils de Bismuth. On en tire une estimation du libre parcours moyen des états de bulk $l_e \simeq 200\,\mathrm{nm}$, également de l'ordre du diamètre du fil.

et le désordre faible[1]. Cela nous donne un moyen experimental d'estimer le libre parcours moyen pour des porteurs de charge dont on peut aussi déterminer λ_F. Le résultat est que les états volumiques sont diffusifs avec un libre parcours moyen similaire aux états surfaciques, c'est à dire limité par le diamètre du fil (fig 1D).

En résumé, le transport électronique dans ces nanofils monocristallins d'Argent et de Bismuth est diffusif, quel que soit le type de canaux : volumiques ou surfaciques.

Propriétés topologiques du Bismuth

Mais il existe un autre ingrédient qui distingue le Bismuth de l'Argent : c'est le couplage spin-orbite. Or ce dernier est colossal dans le cas du Bismuth grace au fait que son noyeau est très lourd. Cette forte interaction entre le spin et le mouvement orbital aura pour conséquence de former des états électroniques sur les bords du crystal. Pour comprendre pourquoi, il faut d'abord comprendre comment se forment les états de bord dans l'effet Hall Quantique entier. Dans le cas d'un gaz d'éléctrons à deux dimensions à fort champ magnétique, lorsque les interférences associées aux oscillations quantiques sont très fortes, des résonnances apparaissent dans la densité d'état (les états de Landau) qui correspondent à des orbites cyclotrons alors qu'aucun état n'existerait entre deux résonnances : le gaz deviendrait isolant. En réalité les orbites cyclotron sont incomplètes sur les bords, ce qui induit une conduction par des états de bord. Ces états sont chiraux : ils suivent le bord de l'échantillon dans un sens déterminé par l'orientation du champ magnétique. Ainsi, une collision avec une impureté ne peut pas changer leur vitesse : ces états sont donc ballistiques (fig 2A).

Il est possible de généraliser cette situation sans champ magnétique, et donc sans briser l'invariance par renversement du temps requise dans le cas de l'effet Hall Quantique entier : il suffit de considérer un champ magnétique de signe différent pour des spins différents (fig 2B). Afin de garantir l'invariance par renversement du temps, nous sommes forcés de choisir une interaction du type $\sigma \times \mathbf{k}$ ou bien $\sigma \cdot \mathbf{k}$: c'est à dire un couplage spin-orbite[2]. Un matériau avec de telles propriétés s'appelle un isolant topologique. C'est précisément cette idée qui a été mise en oeuvre dans les travaux fondateurs de Kane et Mele, où ils ont étudié l'effet du couplage spin-orbite dans le graphène. Il y a seulement deux types de couplage spin-orbite que l'on peut ajouter dans le graphène : le spin-orbite Rashba ou le spin-orbite intrinsèque, qui se distinguent par leurs différentes symmétries. Kane et Mele ont montré que seul le couplage spin-orbite intrinsèque conduit à la formation d'états de bords, alors que le couplage spin-orbite de type Rashba a tendance a les détruire s'il est trop fort. Ce résultat très surprenant nous dit qu'en réalité le graphène serait un isolant topologique ! En pratique le spin orbite intrinsèque du graphène est tellement faible que cet effet serait très difficilement observable. En revanche, ce que nous dit cette théorie c'est que c'est bien du coté des matériaux à fort spin orbite intrinsèque qu'il faut chercher un candidat : le Bismuth est donc tout indiqué.

Pour des matériaux avec d'avantage de symétries comme c'est le cas du Bismuth, il y

---

[1] C'est d'ailleurs au Bismuth que l'on doit la découverte des oscillations quantiques par Kapitza dans les années 1930, car le champ requis pour les observer est très bas, du fait de λ_F grand pour les états volumiques. Si on voulait observer les memes oscillations dans l'Argent il faudrait appliquer des champs magnétiques de l'ordre de 30 T !

[2] En toute rigueur il faudrait associer une fonction impaire en $\mathbf{k}$ au spin σ, mais nous nous limitons ici au premier ordre.

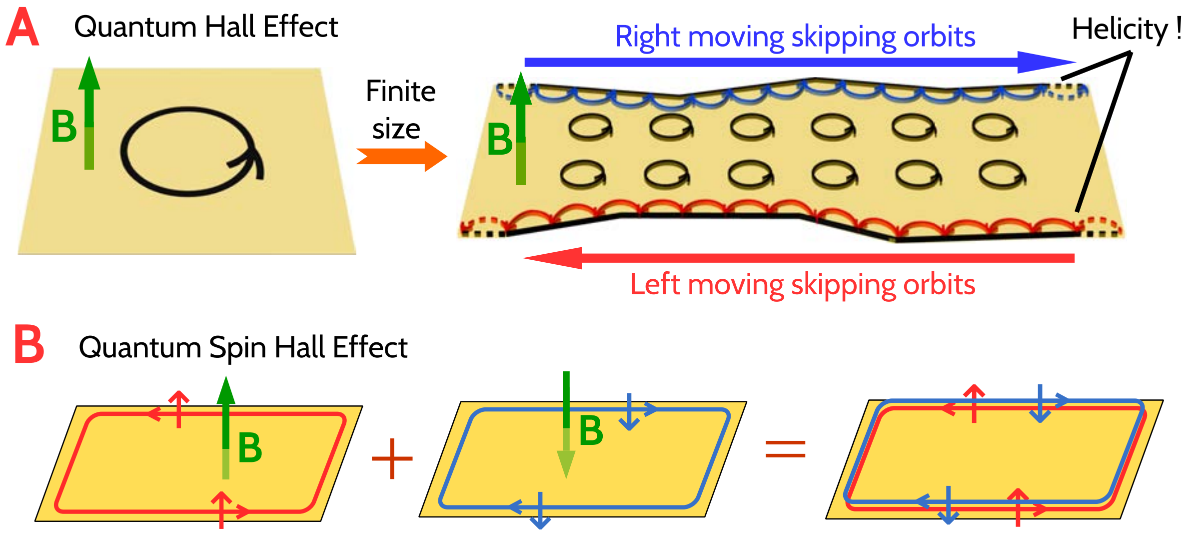

Figure 2: De l'effet Hall quantique entier aux isolants topologiques. A : Lorsque l'on applique un fort champ magnétique sur un gaz électronique à 2 dimesions des niveaux de Landau peuvent se former. Entre deux niveaux de Landau d'energies successives, la conduction est assurée par des états de bord, qui transportent le courant de manière chirale, donc sans rétro-diffusion. B : L'effet Hall quantique de spin est l'analogue de l'effet hall quantique entier, sauf qu'on applique un champ magnétique effectif opposé pour des spins opposés. Cela revient à avoir un couplage spin orbite dans le matériau.

a d'avantage de possibilités pour la forme du couplage spin-orbite, ce qui signifie que l'on ne peut pas appliquer directement le résultat de Kane et Mele. Or il se trouve que la bi-couche de Bismuth est un isolant topologique grace à son spin orbite « naturel », comme l'a démontré théoriquement Murakami : il est isolant en volume et conducteur sur les bords avec des états hélicaux (fig 3B). Cette spectaculaire prédiction a été partiellement confirmée en 2012 par l'équipe d'Ali Yazdani à Princeton. Pour cela ils ont utilisé un microscope à effet tunnel à balayage (en anglais Scanning Tunneling Microscope ou STM), qui permet de cartographier la conductance tunnel (proportionnelle à la densité d'états) avec une grande sensibilité, sur des surfaces de matériaux clivés in-situ. Ils ont alors observé sans ambiguité l'existence d'états unidimensionnels, mais seulement sur la moitié des bords (fig 3C). Pour comprendre pourquoi, il faut remonter à la façon dont les bords du défaut cristallin sont couplés aux états volumiques sous-jacents : soit le bord se termine par un atome en haut de la bi-couche et alors l'état de bord survit, soit le bord se termine par un atome en bas de la bi-couche et alors l'état électronique se délocalise (fig 3B). Néanmoins, cela rapelle fortement les états de bords prédits par Murakami.

J'ai alors voulu étendre la prédiction théorique de Murakami au cas des nanofils de Bismuth. Pour cela, j'ai utilisé le meme modèle de liaisons fortes que lui, mais considéré des systèmes plus épais : jusqu'à une dizaine de bicouches empilées en hauteur, et confiné latéralement à une dizaine d'atomes. Le résultat est sans appel : en calculant la densité d'états locale, nous voyons que la signature des états de bords uni-dimensionnelle survit, meme à la présence des états de surface à laquelle elle se superpose (fig 3D).

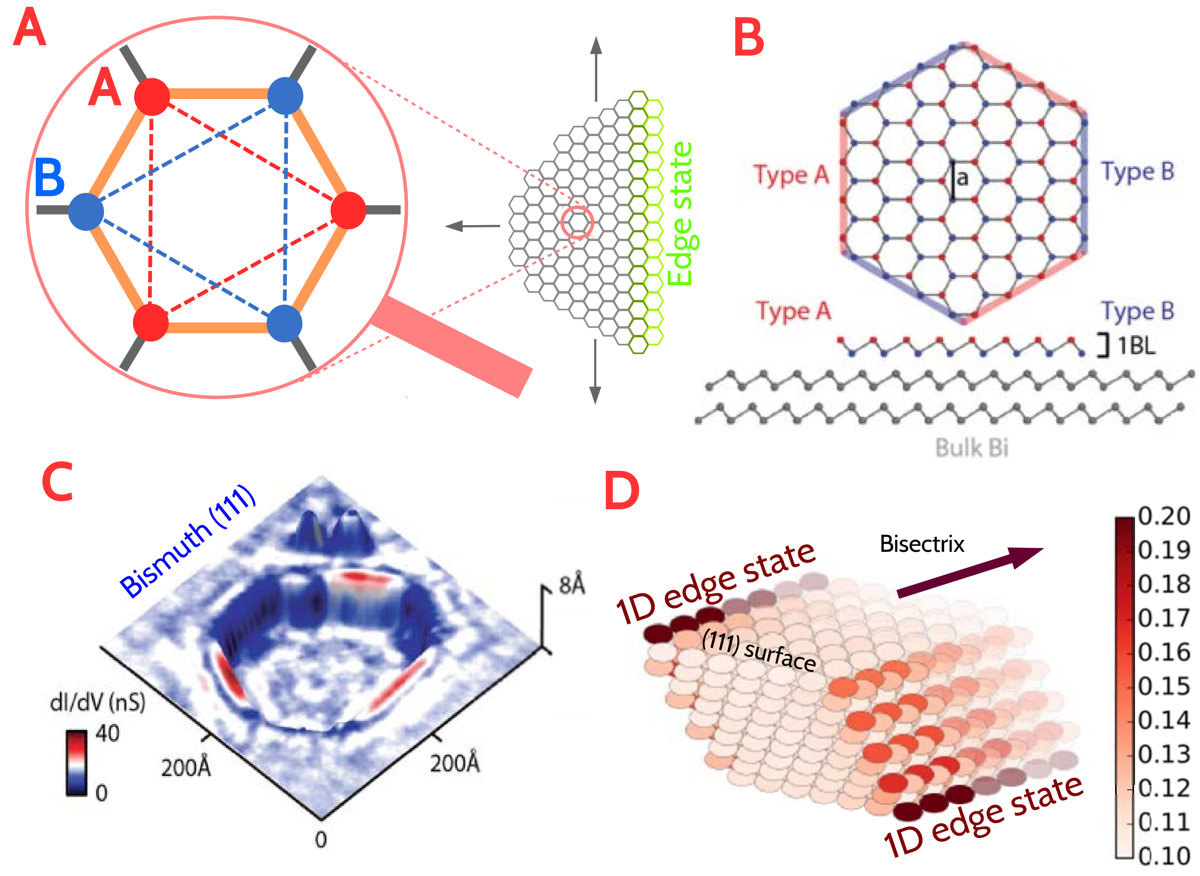

Figure 3: Du modèle de Kane et Mele à la topologie dans le Bismuth. A : Le modèle de Kane et Mele est un modèle de liaison fortes basé sur celui du graphène. La seule différence est l'ajout d'interaction spin-orbite intrinsèque qui couple les atomes de meme site. Cela conduit à la formation d'états de bords. B : La bi-couche de Bismuth est très semblable au modèle de Kane et Mele : réseau hexagonal et fort couplage spin orbite intrinsèque. En revanche, les atomes de site différent n'appartiennent pas au meme plan. C : Cartographie de la densité d'états locale par STM par l'équipe de Yazdani. D : Densité d'états locale simulée avec un modèle tight binding de nanofils de Bismuth. Les états de bord apparaissent directement à partir de cette simulation.

La supraconductivité par effet de proximité

Mais comment observer ces états de bords, et surtout comment démontrer le caractère ballistique, sachant que le transport est dominé par des états surfaciques diffusifs ? Nous utilisons pour cela la supraconductivité par effet de proximité.

Lorsque l'on connecte un nanofil métallique avec des contacts supraconducteurs, le transport électronique dans le fil hérite des propriétés supraconductrices des contacts. On peut ainsi faire passer un courant sans résistance dans la jonction, jusqu'à une valeur maximale permise : le courant critique I_C. Microscopiquement, pour pouvoir transporter des paires de Cooper d'un contact supraconducteur à l'autre, il est nécessaire de les décomposer dans la base des états propres du fil. Les états qui en résultent sont des superpositions cohérentes de quasparticules de type électron et de type trou : ce sont les états (ou paires) d'Andreev. Ce sont des états hybrides, qui héritent à la fois des caractéristiques du métal normal mais aussi des caractéristiques supraconductrices. Par exemple la longueur de cohérence ξ, qui mesure la taille d'une paire, est modifiée quand on passe du supraconducteur au métal. Le fait le plus marquant est que les états d'Andreev dépendent de la différence de phase φ pouvant exister entre les deux contacts supraconducteur.

Lorsque la longueur de la jonction L est telle que $L \ll \xi$ (on parle de « jonction courte ») ce sont surtout les propriétés supraconductrices qui dominent. Le courant critique est alors déterminé par le gap Δ et la conductance du fil G_N. A l'inverse, lorsque $L \gg \xi$ (on parle de « jonction longue ») ce sont les propriétés du nanofil qui dominent : le courant critique dépend toujours de G_N mais l'échelle d'énergie Δ doit être remplacée par l'energie de Thouless $\epsilon_T = \hbar/\tau_D$ où τ_D est le temps nécessaire pour faire traverser une paire d'un contact à l'autre.

L'effet du champ magnétique est de déphaser les paires d'Andreev qui empruntent des chemins différents. Cette différence de phase, d'origine orbitale, est égale à $\Phi_0 B/S$ où S est l'aire entre les deux différents chemins vue par le champ B et $\Phi_0 = h/2e$ est le quantum de flux supraconducteur. Cela signifie que le champ magnétique déphase d'autant plus deux paires qu'elles empruntent des chemins éloignés spatialement. Dans le cas typique où la jonction est constituée d'un métal diffusif avec un grand nombre de canaux comme l'Argent ($N \simeq 10^4$), la somme de toutes ces trajectoires déphasées va résulter en des interférences déstructrices, dès que la valeur du champ magnétique dépasse le champ caractéristique $B_C = S_t/\Phi_0$, où S_t est l'aire du fil vue par le champ magnétique.

Experimentalement, dans le cas des nanofils d'Argent connectés avec du Tungstène[3] ou du Niobium, nous observons effectivement une diminution de I_C en fonction de B, et une suppression de I_C au delà de B_C qui vaut à peine plus de 0.1T, ce qui correspond bien à un quantum de flux dans la surface du fil. En revanche, dans le cas des nanofils Bismuth connectés avec du Tungstène, le champ caractéristique dépasse systématiquement les 10T (nous sommes alors limités par notre bobine supraconductrice), ce qui correspondrait à une surface au moins 100 fois plus petite que celle du fil (fig 4A)! Ce résultat très fort confirme que les états d'Andreev sont très peu nombreux et sont également très confinés. De façon encore plus spectaculaire, au lieu d'observer une suppression de I_C à partir de

---

[3] Le Tungstène utilisé est plutot un alliage désordonné contenant du Tungstène, du Carbone, de l'Oxygène et du Gallium. Il a des propriétés supraconductrices bien meilleures de celles du Tungstène pur : il a un gap Δ et un champ critique H_C^2 beacoup plus élevés.

$B > B_C$, nous avons observé des oscillations du courant critique en fonction de B, avec une période de B_C (fig 4B). Ceci met en évidence des interférences de type SQUID entre canaux situés de part et d'autre du fil.

Notons toutefois que le champ magnétique peut avoir d'autres conséqences que l'effet orbital. Par exemple, lorsque nous avons connecté les nanofils d'Argent avec de l'Aluminium, nous avons observé que le courant critique a tendence à d'abord augmenter en fonction du champ magnétique avant d'etre supprimé, ce qui est très différent de l'effet orbital ! Nous avons interprété ce résultat par un effet de chauffage : lorsque l'on injecte un courant dans la jontion afin mesurer I_C, une partie des électrons de la jonction devient plus chaude que le bain de phonons du substrat. Le champ magnétique permet alors de les thermaliser en créant de nombreuses quasiparticules dans les contacts, qui sont plus larges que le nanofil, et donc mieux connectées thermiquement aux phonons du substrat. La jonction refroidit alors quand on augmente le champ : I_C augmente. Cet effet de chauffage n'a toutefois été observé que pour des contacts en Aluminium, dont les quasiparticules ont des longs temps de vie, mais pas pour les contacts en Tungstène ni en Niobium.

Finalement, en caricaturant, mesurer le courant critique d'une jonction à fort champ magnétique (au delà de la limite B_C habituelle), ce serait comme l'observer à travers un filtre qui favorise les états se propageant à une seule dimension. Grace à cela, nous avons pu mettre en évidence le caractère unidimensionnel des états qui portent le supercourant dans les nanofils de Bismuth. Par ailleurs, nous avons pu mettre en évidence des interférences entre ces canaux, dont la période en champ magnétique correspondrait à des états situés sur les bords du nanofil. Ces états pourraient bien etre les états de bord prédits par la théorie... Pour tester plus finement la prédiction, il nous faut aller plus loin, et imaginer une expérience qui puisse distinguer clairement le type de transport : ballistique ou diffusif.

La mesure de la relation courant-phase

Comme expliqué plus haut, les états d'Andreev héritent des propriétés supraconductrices notamment grace à leur dépendence en phase φ, mais aussi des propriétés du métal normal qui constitue la jonction. En particulier, les états d'Andreev sont beaucoup plus sensibles à φ pour une jonction ballistique que pour une jonction diffusive. Il est donc naturel que la dépendence en φ du courant passant dans la jonction, ce que l'on appelle la « relation courant-phase » de la jonction, possède des signatures très claires du régime de transport dans la jonction : ballistique ou diffusif. Il se trouve justement que lorsque $\varphi \simeq \pi$, la relation courant-phase change de signe de façon très raide dans le cas d'une jonction ballistique, et de façon arrondie dans le cas d'une jonction diffusive.

Afin de mesurer cette relation courant-phase, il faut donc pouvoir réussir à imposer une différence de phase φ aux bornes de la jonction. Cela est impossible si l'on garde une géométrie simplement connexe, car la phase ne peut alors pas etre manipulée par un champ électromagnétique. Nous avons donc fabriqué un SQUID dont un des bras est donné constitué par un nanofil de Bismuth déjà caractérisé, et l'autre bras par une jonction dont le courant critique est connu (fig 4C). Si ce dernier est suffisamment grand par rapport au I_C du nanofil, alors la mesure du courant critique du SQUID en fonction du champ magnétique permet d'extraire la relation courant-phase de la jonction à base de nanofil. C'est ce que nous avons appliqué, et nous avons alors observé la relation courant-phase la plus raide jamais alors observée pour ce type de système (fig 4D). Les états de bords sont donc bien ballistiques.

Conclusions, perspectives

Nous avons étendu numériquement la théorie de Murakami pour des géométrie de type nanofil de Bismuth, qui prédit l'existence d'états de bords topologiques dans la bi-couche de Bismuth. Le fait que ces états de bords vivent en parallèle avec beaucoup d'autres états, qui sont diffusif à cause de la rugsoité de surface, empèche à priori de les distinguer dans une expérience de transport à l'état normal. Nous avons donc utilisé la supraconductivité par effet de proximité agit justement comme un filtre révélateur pour les états de bord ballistiques unidimensionnels. Nous avons alors accumulé des preuves expérimentales qui vont dans le sens de la prédiction d'états de bords unidimensionnels ballistiques : observation d'un courant critique à très fort champ magnétiques, intérférences de type SQUID, relation courant-phase en dent de scie.

Bien que ces preuves soient déjà très convaincantes, il nous faudra aller encore plus loin pour savoir si ces états sont réellement topologiques, en particulier si il existe une relation rigide entre le spin et la vitesse. L'un des tests possibles serait par exemple de faire une mesure de temps de vie dans une expérience où l'on rajoute à la phase statique φ une phase $\delta\varphi(t)$ qui oscille à haute fréquence. On detecte alors le courant à la meme fréquence : la composante en phase donne la partie réactive, le composante hors phase donne la partie dissipative. Si les états sont topologiques, la partie dissipative devrait etre très piquée à $\varphi \simeq \pi$, et ce pic devrait croitre lorsque l'on diminue la température. Un autre test serait de mesurer la différence de moment magnétique entre chaque bord lorsqu'on polarise fortement un nanofil en courant, dans une expérience de gradiométrie, par exemple en utilisant des SQUIDs ou des capteurs à magnétorésistance géante (GMR).

Un autre travail qu'il faudra mener sera de caractériser finement ces nanofils, pour des orientations crystallographiques et des facettes différentes, ainsi que pour différentes orientations de champ magnétiques, afin d'extraire les propriétés de ces états de bords : extension spatiale, facteur g.

Ces expériences nous montrent que le Bismuth, qui est historiquement l'un des matériaux les plus fascinants de l'histoire de la matière condensée, continue encore de nous surprendre aujourd'hui. Ses propriétés topologiques combinées à la supraconductivité par effet de proximité pourraient permettre de réaliser des qubits d'un genre nouveau en émulant des particules égales à leur anti-particule : les fermions de Majorana.

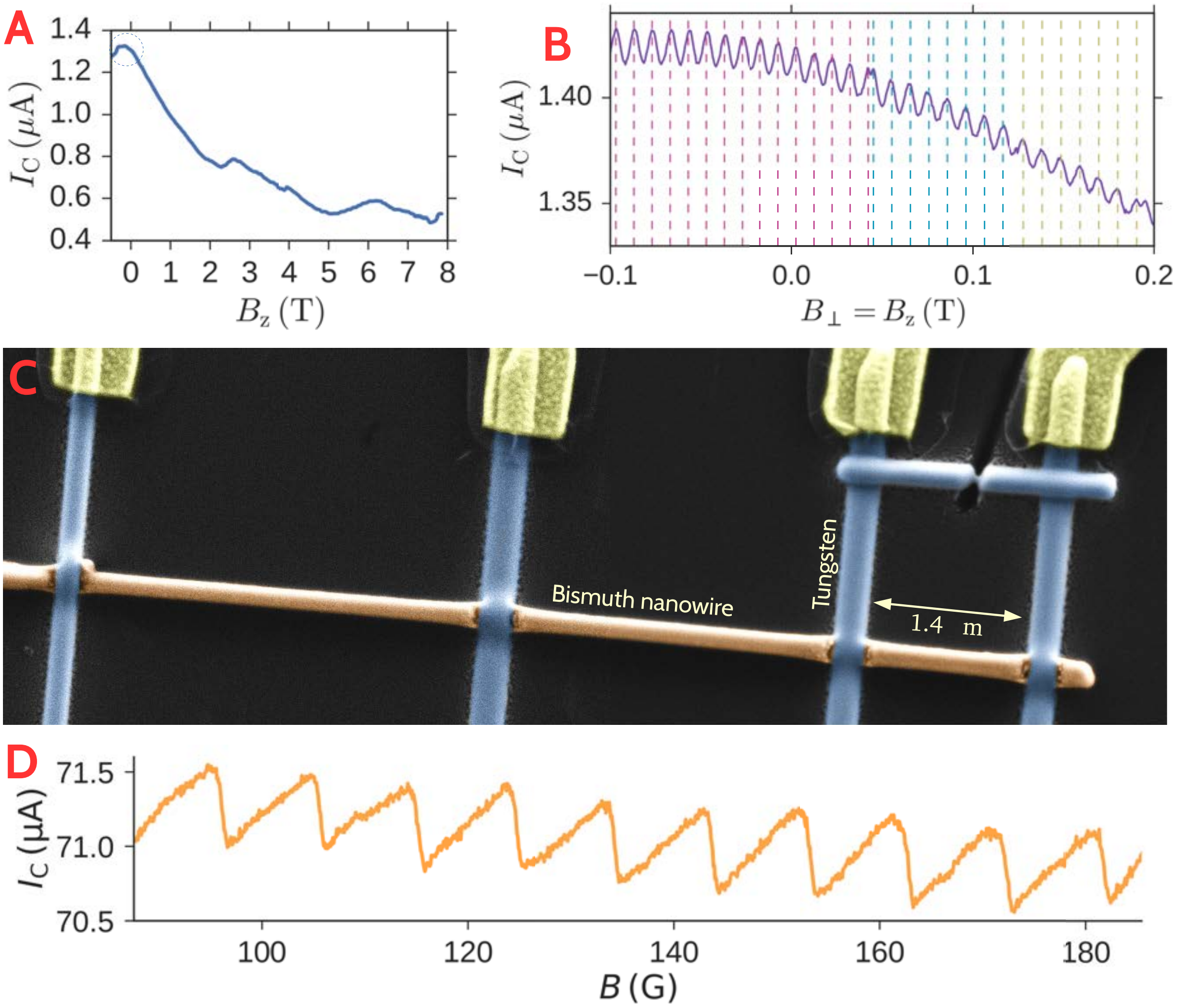

Figure 4: Signatures experimentales des états de bords dans les nanofils de Bismuth. A : Le supercourant résiste aux forts champs magnétiques. Cela implique qu'il existe un petit nombre d'états unidimensionnels dans les nanofils. B : En zoomant à bas champ magnétique, on observe des interférences de type SQUID, dont la période correspond a l'aire du fil vue par le champ magnétique. Les états sont donc localisés sur les bords. C : Nous avons fabriqué un SQUID avec une constriction en Tungstène autour du nanfofil pour mesurer sa relation courant-phase. D : La relation courant-phase est en dent de scie : les états de bords sont ballistiques.

Contents

Introduction

In this introduction, I give in the first place a general definition of mesoscopic physics, and briefly describe the concepts and the context of this field. Then I detail specifically the directions that lead to the work achieved during this thesis. I also give the introductory references that I find important for the understanding of this rapidly moving field. I finish by providing an overview of the structure of the manuscript.

The beginning of the 20^{th} century was marked by great advances in the understanding of the laws of physics, and in particular by the discovery of quantum mechanics, that is the theory describing matter at very small distances, for example atom or even smaller particles. It also describes the interaction between light and matter via exchange of quanta of energy $h\nu$, ν being the frequency of the photon and h the Planck's constant, and one of its important early success was that it solved the ultraviolet catastrophe problem of the blackbody radiation. However, it seems that we do need to apply the laws of quantum mechanics to explain the physics of our everyday life : for example there is very little probability of passing through a chair as we are sitting on it. Therefore a boundary must exist between the macroscopic world which is governed by the laws of classical physics, and the microscopic world which is governed by the laws of quantum mechanics. The field of physics dealing with large objects that can still be described by quantum mechanics is called mesoscopic physics (Imry, 2002).

The beginning of 20^{th} was also marked by great advances in the experimental techniques, among which the dawning field of cryogenics : the science of low temperatures. Superconductivity, one of the greatest discovery of that century, was discovered in mercury in 1911 by K.Onnes, in a celebrated experiment (fig 5A) initially motivated by the understanding the resistivity of some metals at low temperatures (Tinkham, 2004). It consists in the property of some metals to display a vanishing resistance below a given temperature T_{C}. A satisfactory theory by L.Landau and V.Ginzburg using a free energy functional describes most of the thermodynamical properties of superconductors, but it was only in 1957 that a comprehensive microscopic theory developed by J.Bardeen L.Cooper and J.Schrieffer (BCS) successfully explained the phenomenon at play. At low temperatures, the attractive effective interaction between the electrons of a metal that are mediated by phonon leads to a pairing between electrons having opposite spin and opposite momentum. These so called Cooper pairs form a ground state that is described by a single macroscopic wavefunction $\Psi \equiv \Delta \mathrm{e}^{i\varphi}$. For this reason, superconductors are certainly the most striking examples of mesoscopic physics : they are macroscopic objects governed by the laws of quantum mechanics. Furthermore, the BCS ground state breaks the global gauge symmetry, which in practice implies that it will remain invariant with respect to small changes in the electromagnetic potential in the static and long range limit ($\omega \to 0$, $q \to 0$). This property, termed “rigidity” of the wavefunction by F.London with respect to these perturbations, implies that a superconductor is a perfect diamagnet : it expels entirely a small, externally applied magnetic field : this is the Meissner effect. This effect was successfully predicted by BCS, and is related to the ability of superconductors to carry a current without dissipation.

Many other macroscopic systems can be described by the laws of quantum mechanics : cold atoms gases, quantum dots, tunnel junctions, Josephson junctions, entangled photons over large distances, etc. Importantly, all these experimental systems are not isolated systems. On the contrary, they are coupled to many external degrees of freedom, generally termed the environment. For example solid state systems are coupled to phonons bath at finite temperatures, to photons populating the electromagnetic environment, to the fluctuations of the magnetic moment of nuclear spins, etc. By coupling the system to these numerous degrees of freedom it exchanges energy by small amounts, thereby at the same time mixing its wavefunction with the wavefunction of the environment. As a result, the original wavefunction of the system soon becomes ill defined and loses its quantumness. This latter property can be quantified by the timescale over which the phase of the wavefunction of a subsystem becomes random : the phase coherence time τ_φ. Generally, this time gets smaller as the object gets larger, or the temperatures gets higher (Akkermans & Montambaux, 2007).

At low temperatures, the electrons in circuits also behave quantum mechanically. The sub-field of mesoscopic physics dealing with the electronic degree of freedom is called quantum transport (Nazarov & Blanter, 2009). It extends the known concepts of electronic engineering to the realm of quantum mechanics, and in return aims at describing the electronic components and circuits by the laws of quantum mechanics. The most celebrated demonstration of phase coherence in quantum transport is the Aharonov Bohm effect. Similarly to a Michelson interferometer, where a laser beam splits and further recombined interferes either constructively or destructively depending on the phase difference between the two paths depending on their relative lengths, split trajectories of quantum coherent electrons also display interferences. The difference between the two situations lies in the fact that in the latter, tuning of the phase difference is achieved by changing the magnetic flux encircled by the loop (fig 5B).

Moreover one usually probes these systems similarly to classical circuits, that is via the measurement of resistances, inductances, capacitances, phase shifts, frequency shifts, power spectral densities (of e.g. the noise), etc. This is interesting technologically because standard techniques and apparatus are developed to measure e.g. voltages with high sensitivity, but also in the time domain and especially for frequencies in the microwave range. Importantly, a way to access the quantum dynamics of a mesoscopic system, and to measure its phase coherence time, is to perform quantum interference experiments in the time domain. The microscopic description of interaction between a mesoscopic system with resolved energy levels and a time dependent perturbation is done through the coherent exchange of energy between the states of the mesoscopic system and the photon states. This is analogous to the quantum interaction of light and matter at the atomic scale, described by the theory of quantum electrodynamics (QED). Therefore mesoscopic circuits can mimic atomic physics, although they can themselves be composed by a few 10^{15} atoms or even more. In order for quantum coherence of a circuit not to be lost in the electromagnetic environment, it is necessary to control it, for example by confining the circuit within a cavity that can be made on a chip (Schuster, 2007).

In parallel, the physics of condensed matter was the stage of important developments during the last two decades, both experimentally and theoretically. The discovery in 2004 by K.Novoselov and A.Geim of the mechanical exfoliation technique applied to produce graphene, which is an atomically thin crystal of carbon atoms ordered in a honeycomb

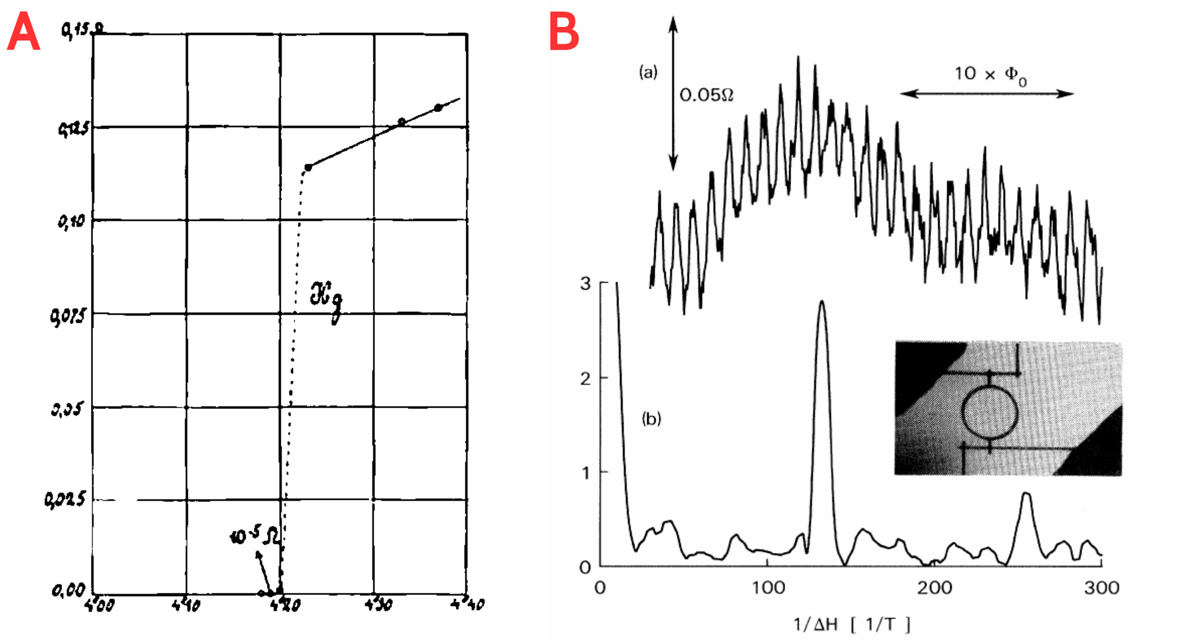

Figure 5: Measurements of two different systems displaying phase coherence on a macroscopic scale. **A** : Temperature dependence of the resistance of Hg, showing a superconducting phase transition at 4.2 K. This is the historic curve of the discovery of superconductivity by K.Onnes in 1911. **B** : Measurement of the Aharonov Bohm effect in a Au ring at 10 mK. Top : Magnetic field dependence of the resistance at low temperatures of the ring. The signal displays clear oscillations, periodic in the flux thread in the ring, with period $\phi_0 = h/e$. Bottom : Fourier transform. Inset : SEM image of the device. Taken from (Webb et. al., 1985)

lattice, has enabled the production and study of a variety of other two dimensional systems : hBN, MoS_2, WS_2, NbSe_2, etc. Using this technique, one can even produce hybrid structures by stacking two dimensional materials (Geim & Grigorieva, 2013), thereby extending the existing techniques of nano-fabrication ranging from electronic lithography to chemical vapor deposition of carbon nanotubes. Importantly, the electrons in graphene behave relativistically as their dispersion relation is linear, hence they are termed Dirac fermions. Subsequently, topological insulators were predicted : they consist in band insulators with strong spin-orbit interaction having the property to conduct through edges, which are Dirac fermions propagating on the surface (Hasan & Kane, 2010). Moreover, these edge states are helical, meaning that their spin and momentum are locked, and their number depends only on the topology of the sample.

With this in mind, mesoscopic physics has now the ability to shed a new light on old problems of condensed matter, such as the Kondo effect (Basset, 2011), (Delagrange, 2016), (Iftikhar, 2017), but also new ones such as topological insulators : this is the object of the present thesis.

1 Phase coherent electronic transport

As previously stated, phase coherent electronic transport deals with the physics of electrons in metals or other condensed matter systems that maintain quantum coherence. On the other hand, the system will unavoidably couple to an external bath, consisting in a system at thermal equilibrium with infinitely many degrees of freedom such as thermal photons, phonons or magnetic impurities to a bath, which will lead to an irreversible loss of coherence.

I now give an overview on some active problematics in this field.

1.1 Disorder and dissipation in mesoscopic physics

Mesoscopic conductors fabricated by lithography are generally disordered systems because the metals are formed by individual grains that can be very small, and therefore scatter at relatively short distances. However, for static disorder, the processes of exchanging momentum between electrons and scatterers are elastic : they only affect trajectories but do not affect phase coherence. For this to be valid, the length L of the conductor should be smaller than the coherence length L_φ, which is the scale over which phase coherence is lost. L should also be smaller than the thermal length L_T, which is the characteristic length after which an initial (non thermal) energy distribution is lost. For weak disorder, there is a quantum correction of the conductance of the order of $2e^2/h \simeq 7.74 \cdot 10^{-5}\,\mathrm{S}$, due to quantum interferences between unscattered trajectories and backscattered trajectories : this is weak localization. This effect is washed out as one applies a magnetic field such that the flux across the area of the sample is greater than $\phi_0^\mathrm{N} \equiv h/e \simeq 4 \cdot 10^{-15}\,\mathrm{Wb}$, because the interferences corresponding to the different trajectories across the sample are averaged out. In the limit of strong disorder $k_\mathrm{F} l_\mathrm{e} \simeq 1$, where k_F is the wavevector and l_e is the mean free path, transport can be strongly modified and even completely suppressed, a phenomenon termed Anderson localization (Imry, 2002).

On the contrary, if no disorder is present in a wire, and if the transmission is perfect, then the conductance is necessarily quantized, equal to $2e^2/h$ per conducting channel, where the factor 2 comes from spin degeneracy. For an arbitrary conductor, the conductance is given by

$$G = \frac{2e^2}{h}\mathrm{Tr}\left(\mathbf{t}^\dagger \mathbf{t}\right) \tag{1}$$

where $\mathbf{t}$ is the transmission matrix of the conductor. This is the celebrated formula of Landauer and Buttiker (Imry, 2002). A very important point in this description is that while phase coherence is preserved along the wire, the dissipation necessarily happens in the reservoirs (fig 6A).

The presence of phase breaking mechanisms in these reservoirs is thus crucial for this description of quantum transport. In fact, this description can break in some cases e.g. with several quantum conductors connected in a network. Due to the presence of plasmons, which are low frequency collective modes with the restoring force given by the screened electron-electron interaction, some correlations take place between the coherent quantum conductors, resulting in important corrections to the conductance, and the noise (Altimiras, Portier & Joyez, 2016), (Fevrier, 2017).

An other case where the Landauer Buttiker description fails is when the reservoirs are superconductors and the normal metal in between is phase coherent. Then the superconducting correlations are transmitted from the superconductor to the normal metal, which therefore inherits superconducting properties, and in particular a zero resistance. This effect is called the superconducting proximity effect. The critical current, that is the maximal current one can apply before the junction switches to a resistive state, cannot directly be expressed using the transmission matrix of the conductor in the most general cases, but only if the length of the junction is small enough.

1.2 Superconducting proximity effect

In 1962, B.D. Josepshon made the following prediction : when two superconductors are separated by a thin insulating barrier then the voltage across the barrier and the current are related to the phase difference φ between the superconductors through

$$\begin{cases} V(t) = \dfrac{\hbar}{2e}\dfrac{\partial\varphi}{\partial t} \\ I(t) = I_0 \sin\varphi \end{cases} \tag{2}$$

where I_0 is the critical current of the junction which depends on the gaps of the superconductors (that I assume to be equal in the rest of the manuscript) and the resistance of the junction in the normal state. The first equation result from Maxwell equations, relating the scalar potential and the vector potential, while the second results from the coupling of the two superconductors by Cooper pair tunneling. A consequence of these equations is that if one applies an external bias current on the SIS junction, one measures a zero resistance as long as the phase difference is constant, that is for $I < I_0$, and one recovers a finite resistance for $I > I_0$. This is the DC Josephson effect. It was confirmed experimentally by Anderson and Rowell short after the prediction (Anderson & Rowell, 1963).

If one replaces the oxyde barrier by a normal metal, a similar effect takes place if $L \ll L_\varphi$, L_T, where L_T is the thermal length that measures the loss of coherence due to the finite energy width of the Fermi occupation function, but in this case the Cooper pair have to be decomposed on the states of the normal metal. From the perspective of an electron in the normal metal, a new reflection process can occur at the interface with the superconductor (the NS interface) by reflecting it as a hole of opposite spin and velocity thereby creating a Cooper pair solution inside the superconductor. If this process, called Andreev reflection, is performed a second time on the second NS interface converting the hole back into an electron, then a bound state can exist at the condition that the total accumulated phase is an integer multiple of 2π (fig 6E)

$$2\frac{\epsilon L}{\hbar v_{\mathrm{F}}} + 2\arccos\left(\frac{\epsilon}{\Delta}\right) \pm \varphi = 2n\pi \tag{3}$$

where v_{F} is the Fermi velocity and ϵ is the energy of the bound state. When the first term dominates (resp. is negligible), the junction is said to be long (resp. short). As a result, the superconducting pair correlations can propagate through a normal metal thanks to the formation of bound states called the Andreev bound states (ABS), leading to a zero resistance state at small bias currents. For a junction with few electronic states, the ABS spectrum is discrete (fig 6F). On the contrary, for a long junction that has many channels and a lot of disorder, the spectrum is continuous (fig 6G). In general, the sub-gap structure can be very rich and a more complicated description than (3) is necessary. This will be described in more details in chapter 3.

The simplest Andreev spectrum is the one of a junction in the atomic limit and can be realized experimentally in break junctions, where the number of channels can be controlled by mechanically stretching an Al wire just before it breaks. In this system, only two ABS exist, and the supercurrent is simply given by the sum of the current carried by each individual level. However, as one allows many-body occupation of these states, the supercurrent can vanish as soon as the parity of the occupation is odd (Bretheau, 2013). This phenomenon termed poisoning is general, and result from the coupling of ABS to the reservoirs, which may contain quasiparticles not belonging to the superconducting condensate, that exist even at zero temperature (about 10 per μm^3 in Al). Poisoning is thus a form of dissipation resulting from the coupling to reservoirs, that complicates the physics of superconducting proximity effect.

1.3 Orbital and Zeeman dephasing

It is a known fact that a s wave superconductor is weakened as one applies a magnetic field. However, there are two possible causes responsible for this. Indeed, Cooper pairs are formed by pairing electrons of opposite spin and opposite momenta with respect to the frame of the condensate's center of mass. This provides two ways to break a Cooper pair : one can either split the pair apart in spin space or in momentum space. A magnetic field does both as it splits the spin through the Zeeman effect, and splits momenta through the Lorentz force. These effects are termed paramagnetic and orbital respectively. In general, the orbital effect is the main cause of destruction of superconductivity. This can be understood by a simple scaling argument : the Lorentz force acts on a lengthscale of the order of the size of a Cooper pair $\xi_{\mathrm{S}} = \hbar v_F/\pi\Delta$, which has a velocity of the order of v_{F}.

Therefore applying a magnetic field B costs the Cooper pair an energy

$$E_{\mathrm{orb}} \sim 2ev_{\mathrm{F}}B\xi_{\mathrm{S}} \sim 2\Delta\frac{2\pi B\xi_{\mathrm{S}}^2}{\phi_0} \tag{4}$$

On the other hand, the Zeeman energy will scale as

$$E_{\mathrm{Z}} \sim 2\hbar eB/m \sim 2\Delta\frac{B\lambda_F\xi_{\mathrm{S}}}{\phi_0} \tag{5}$$

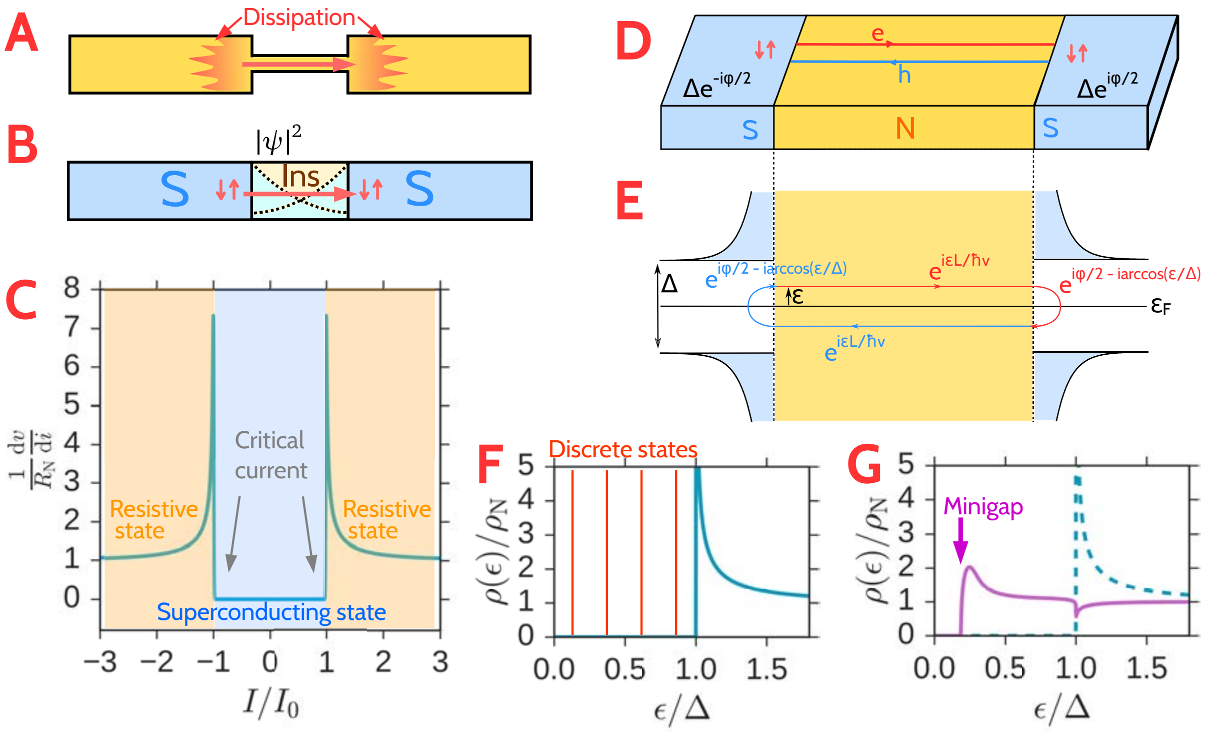

Figure 6: The physics of transport in some mesoscopic devices. **A** : Cartoon of a thin metallic nanowire transporting electrical current, where the dissipation occurs inside the large reservoirs. **B** : Cartoon of a SIS junction. The wavefunction of the superconducting reservoirs penetrates inside the insulator by tunneling (black dotted lines), allowing a supercurrent to propagate through the junction. **C** Differential resistance versus bias current in a superconducting tunnel junction. The junction switches from a superconducting state at low bias current to a resistive state at higher bias current. One defines the critical current by the maximal current at which the junction displays a zero resistance. **D** : Cartoon of a SNS junction. The superconducting reservoirs are coupled through the normal metal junction. Bound states are formed in the junction from the coherent superposition of counterpropagating electrons and holes. **E** : Semiconductor picture showing the formation of an ABS inside an SNS junction. The curves represent the density of states : which displays a gap in the superconductors. **F** : Sub-gap structure of a SNS junction with few states, forming a discrete ABS spectrum (orange lines). Solid blue curve : normalized BCS superconducting density of state composing the spectrum at energies $\epsilon > \Delta$. **G** : Sub-gap structure in the case of a long, disordered SNS junction with many channels (purple). In this case, a smaller gap arises, termed the minigap. Dashed blue : normalized BCS density of states, which is not part of the spectrum here.

where I have used $\lambda_F v_F = h/m$ and a g-factor $g = 2$.

For clarity, I should stress two points : first, although the work done by the Lorentz force on a charge particle is locally zero, its work done on a closed trajectory can be finite. Second, although the externally applied magnetic field should be screened in a bulk superconductor due to the Meissner effect, it is not screened for films that are much thinner than the London penetration length λ_L, which is the case we have in mind. In any case, the magnetic field seen by a Cooper pair is the same for both contributions.

As a result

$$E_\mathrm{Z}/E_\mathrm{orb} \sim (k_\mathrm{F}\xi_\mathrm{S})^{-1} \sim \Delta/E_\mathrm{F} \ll 1 \tag{6}$$

which is a small quantity for most superconductors.

In the realm of proximity effect as well, the Andreev bound states are dephased due to both the orbital and Zeeman effect. However, the orbital dephasing dominates even more in the proximity effect compared to a superconductor, while the Zeeman effect is unchanged. Indeed, because there is no Meissner screening in the normal metal, the gauge potential $\mathbf{A}$ is a varying quantity of space in the normal metal. This means that two Andreev pairs following different trajectories in real space sense a difference in $\mathbf{A}$. This results in a difference in the total accumulated phase generating an interference pattern. As one integrates on all the possible trajectories, scrambling interferences will occur, resulting in a destruction of the supercurrent. In other words, the scale E_orb will now given by

$$E_\mathrm{orb} = 2\mathrm{min}(\Delta, E_\mathrm{T})\frac{BS}{\phi_0} \tag{7}$$

where S is the surface of the normal metal. Therefore, a typical magnetic field scale is set by $B \sim \phi_0/S$, that is one flux quantum per unit area, after which no supercurrent is expected.

However, the precise dependence of the decay of the supercurrent resulting from this orbital dephasing depends on several factors. The resulting interference pattern depends in particular on the geometry (Montambaux, 2007)

$$I(B) = \begin{cases} I_0 \dfrac{\frac{\pi}{\sqrt{3}}\frac{\phi}{\phi_0}}{\sinh\left(\frac{\pi}{\sqrt{3}}\frac{\phi}{\phi_0}\right)} & w \ll L \\ I_0 \left|\dfrac{\sin\left(\pi\frac{\phi}{\phi_0}\right)}{\pi\frac{\phi}{\phi_0}}\right| & w \gg L \end{cases} \tag{8}$$

This has been recently demonstrated experimentally in Au junctions (Chiodi et al., 2012). The oscillatory behaviour in the regime $w \gg L$ is closely related to the appearance of vortices inside the N part (Cuevas & Bergeret, 2007), a fact that has been recently observed with STM (Roditchev et al., 2015).

It is therefore interesting to measure the critical current of a SNS junction as a function of magnetic field because it can give information on Andreev trajectories through the mechanism of orbital dephasing.

1.4 Towards measurements without contacts

Measuring of the critical current as a function of an applied magnetic field can therefore reveal some interesting information on the ABS. However, in this two wires setup (fig 7C), the phase difference φ between the superconductors is not controlled. It turns out that the ABS depend crucially on φ, and so does the supercurrent. The resulting current-phase relation (CPR) is characteristic of the propagation and reflection of Andreev bound states : for example it is a sine for the case of tunnel junctions or SNS junctions with disorder or bad transmission. To measure such a relation, one can insert the junction inside a superconducting loop (fig 7C) thereby realizing a SQUID. By making a suitable gauge choice, it can be shown that the electron-hole superposition is described by a wavefunction living on a periodic ring of size $2L$ verifying twisted boundary conditions :

$$\Psi(x+2L) = \Psi(x)\mathrm{e}^{2i\pi\frac{\phi}{\phi_0}} \tag{9}$$

where $\phi_0 = h/2e$ is th superconducting flux quantum. The space on which the system lives being periodic, the phase should only differ from the phase of Bloch wavefunction by a integer multiple of 2π, thus defining a quasi-momentum

$$k_n = \frac{\pi}{L}\left(n + \frac{\phi}{\phi_0}\right) \tag{10}$$

The application of an Aharonov Bohm flux inside the loop thus realizes an analogue to the crystal momentum in solids.

Some very interesting physics lies in the dynamics of the ABS. It was recently shown that although DC transport is dissipationless, AC transport has a dissipative component resulting from the finite relaxation time of ABS if they are excited (Chiodi, 2010), (Dassonneville, 2013). In order to achieve a measurement at finite frequency, a possibility is to insert it inside a superconducting resonator, that acts as a frequency filter. By placing an NS loop at the magnetic field antinode of the resonator, one can add an AC flux component $\delta\phi_{\mathrm{AC}} \propto \mathrm{e}^{i\omega t}$ to the DC flux that phase biases the SNS junction (fig 7C,D). The reflection coefficient of the cavity thus measures a response function that is nothing but a magnetic susceptibility

$$\chi(\varphi,\omega) \equiv \frac{\delta i}{\delta\phi_{\mathrm{AC}}} \tag{11}$$

which is complex, the imaginary part describing to dissipation and the real part the reaction. The information contained in $\chi(\varphi,\omega)$ being phase and frequency resolved is well suited to probe the properties of the Andreev spectrum, likewise the energy and momentum resolved response function $\chi(q,\omega)$ routinely measured in solids with ARPES probes their band dispersion.

2 Topologically protected transport

2.1 Spin-orbit coupling

In metals, the positively charged ions exert an attractive electric force on the free conduction electrons gaz due to Coulomb interaction. Moreover, these electrons move with a velocity $v_{\mathrm{F}} \simeq 10^6\,\mathrm{m.s^{-1}} \simeq \alpha c$, where $\alpha \simeq 1/137$ is the fine structure constant and $c \simeq 3\cdot 10^8\,\mathrm{m.s^{-1}}$ is the speed of light. As a result, one expects relativistic terms in the hamiltonian of the order of α. However, we know from special relativity that an electric field in a moving referential will also produce a magnetic field $\mathbf{B} = \mathbf{v}\times\mathbf{E}$. Since the electrons have a definite spin, they interact with a magnetic field according to

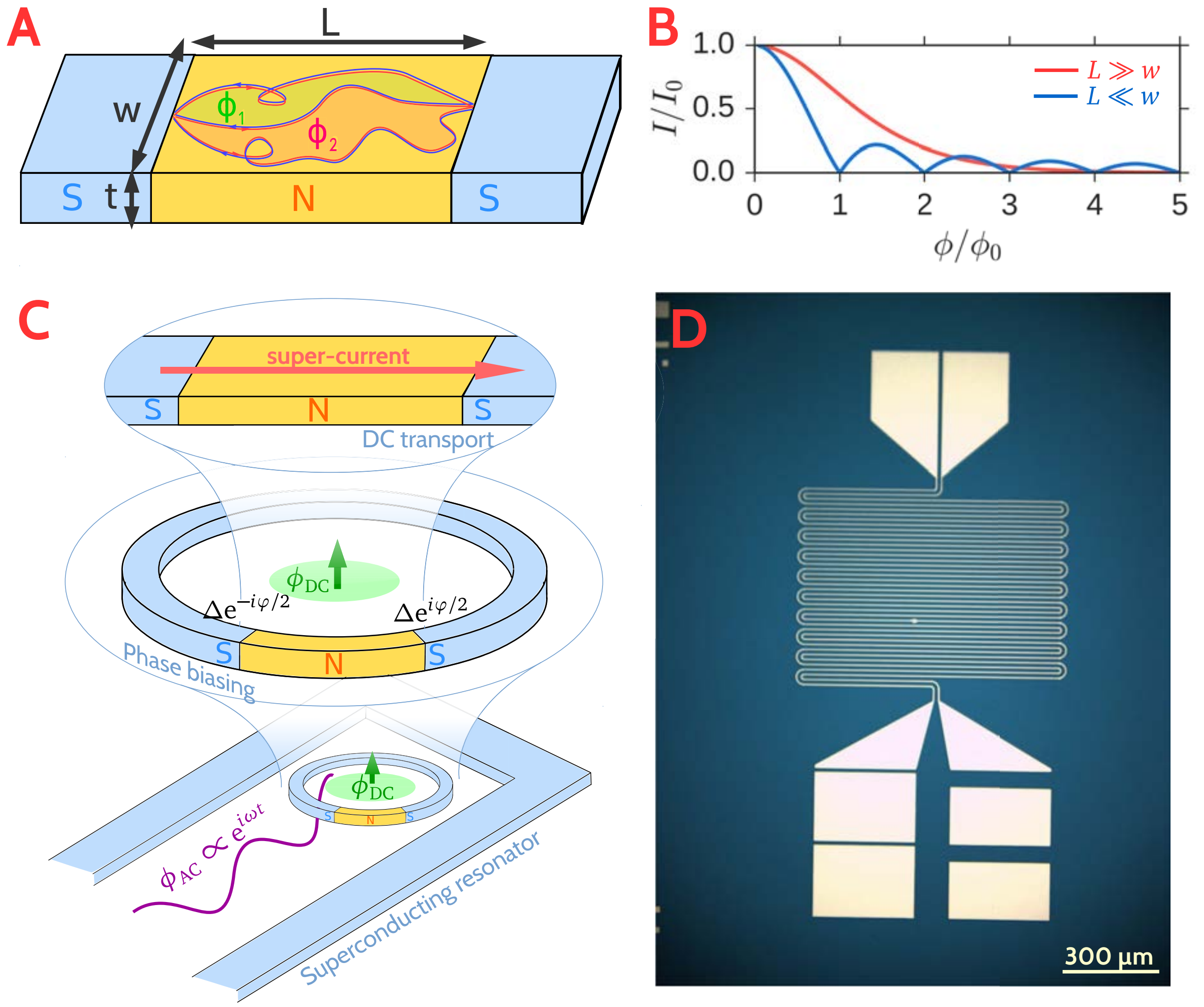

Figure 7: Insertion of a NS loop inside a resonator. **A** : SNS junction with multiple channels. The ABS trajectories enclose different fluxes, leading to scrambling interferences in a finite magnetic field. **B** : Supercurrent vs magnetic flux penetrating a SNS junction with many channels, for different geometries. In any case, the supercurrent is significantly reduced as soon as $\phi > \phi_0$ **C** : Cartoon of the insertion. Top : In DC one can only measure the critical current, that is the maximal value of the supercurrent. Middle : In order to fix the superconducting phase, one way is to build a loop, thereby making a SQUID (an RF-SQUID here). The phase difference is tunable through the DC flux bias ϕ_{DC}. Bottom : In order to probe the dynamics, one can insert the SQUID inside a superconducting resonator. **D** : Optical image of a bifilar resonator, similar to those used and developed in this thesis

$$H_{\mathrm{SO}} \equiv \frac{\hbar}{2m^2c^2}\left(\mathbf{p} \times \boldsymbol{\nabla} V\right) \cdot \boldsymbol{\sigma} \tag{12}$$

where m is the electronic mass, $\mathbf{p}$ is the momentum, $\boldsymbol{\sigma}$ is the spin, V is the attractive potential. This is the spin-orbit interaction.

Depending on the symmetries of a given crystal, the spin-orbit can take different forms. In particular, one distinguishes two kinds of spin-orbit interaction : the Rashba spin orbit that occurs if inversion symmetry is broken and the Dresselhaus spin orbit, which is of lower symmetry.

2.2 From Integer quantum Hall effect to Quantum Spin Hall Effect

As one applies a strong magnetic field on a clean conducting 2D electron gaz, it becomes insulating with conduction occurring only at the edges (fig 8A) : this is the integer quantum Hall effect (IQHE). An interesting question is raised from this observation : can similar physics exist without the application of a magnetic field, that inherently breaks time reversal symmetry ?

The answer is yes. The idea is to take one copy of the QHE system for each spin, with a different direction of the external magnetic field in each copy (fig 8B) : this is the quantum spin Hall effect (QSHE). In the seminal work of Kane and Mele (Kane & Mele, 2005), an elementary model was made by adding spin orbit interaction terms to the tight binding model of graphene (fig 8C)

$$\begin{aligned} H \equiv\ & t \sum_{\langle i,j\rangle \alpha,\beta} \hat{c}^{\dagger}_{i,\alpha}\hat{c}_{j,\beta} \\ & + \frac{i\lambda_{\mathrm{SO}}}{2} \sum_{\langle\langle i,j\rangle\rangle \alpha,\beta} \nu_{i,j}\sigma^{z}_{\alpha,\beta}\hat{c}^{\dagger}_{i,\alpha}\hat{c}_{j,\beta} \\ & + i\lambda_{\mathrm{R}} \sum_{\langle i,j\rangle \alpha,\beta} \nu_{i,j}\left(\left(\boldsymbol{\sigma}_{\alpha,\beta} \times \mathbf{d}\right) \cdot \mathbf{e_z}\right)\hat{c}^{\dagger}_{i,\alpha}\hat{c}_{j,\beta} \end{aligned} \tag{13}$$

where $\nu_{i,j} = \pm 1$ depending on the orientation of the link being clockwise (+1) or anticlockwise (-1), $\mathbf{d}$ is the vector corresponding to the bond considered in the sum. The indices i, j denotes the summation on cells, while the indices α, β denotes the atom type (A or B). The first term is the hopping term of graphene, the second term is the intrinsic spin-orbit coupling term, and the third term is the Rashba interaction. In the continuous limit, this spin-orbit interaction yields the intrinsic spin orbit mentioned above, which takes the form $H_{\mathrm{SO}} \rightarrow \lambda_{\mathrm{SO}}\psi^{\dagger}\tau_z\sigma_z s_z\psi$. Under the condition that $\lambda_{\mathrm{R}} < \lambda_{\mathrm{SO}}$ and $\lambda_{\mathrm{SO}} > 0$, chiral edge states are indeed found (fig 8C,D). Importantly this topological phase is also found for $\lambda_{\mathrm{R}} = 0$ and $\lambda_{\mathrm{SO}} \neq 0$, which signifies that the QSH is likely to be found in materials with a strong intrinsic spin orbit coupling (and comparatively small Rashba interaction).

As a matter of fact, Bismuth bilayer was soon after predicted to be in the topological phase (Murakami, 2006). Later, an STM experiment from the Yazdani group (Drozdov et al., 2014) demonstrated the existence of one dimensional states at the edges of (111) bismuth, located in a mesa (fig 8E). However, only one edge state on two was found to exist. The reason for this is that Bismuth bilayer contains next-nearest neighbors in different atomic planes, therefore a bilayer coupled to bulk Bi, will have only half of edges protected. Depending on the termination of the edge, it will remain uncoupled from the

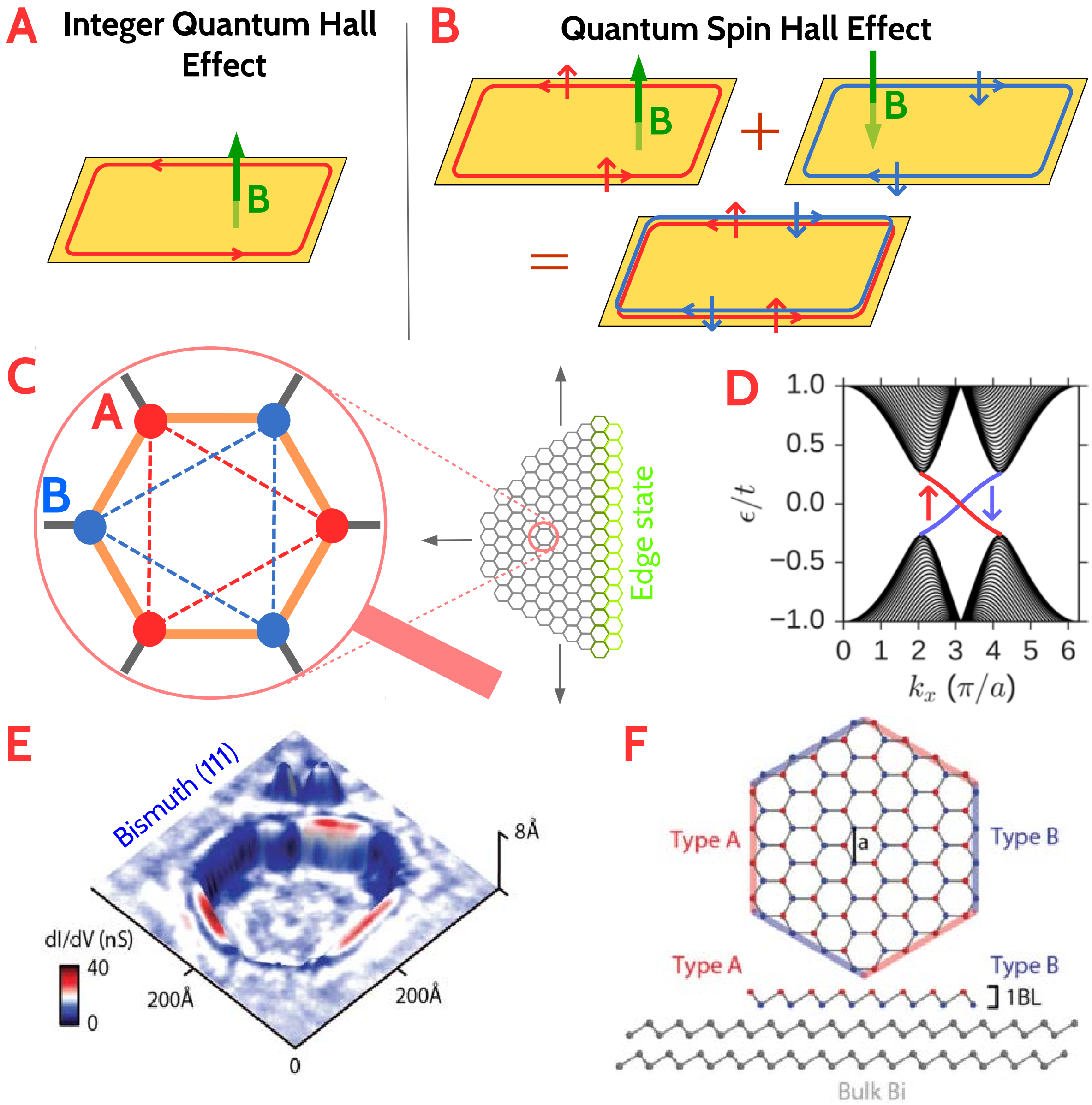

Figure 8: Two dimensional topological systems. **A** : Cartoon of the IQHE effect : a clean 2D electron gas under a strong magnetic field has some conduction through the edges **B** : In the QSHE, two copies of the IQHE system for each spin with an opposite magnetic field are combined into a single one. This results in the existence of two counterpropagating edge states. **C** : Graphene lattice with intrinsic spin orbit coupling, as computed by Kane and Mele. This model displays edge states. **D** : Energy dispersion at one edge. The gap closes thanks to two chiral edge modes. **E** : STM measurement of the LDOS on a surface depression of a (111) Bi surface, displaying 1D edge states. **F** : Schematics of the Bi lattice. The zigzag termination of the edges can lead to two types of behaviour : in the zigzag type A edge the top atom terminates the edge and the edge states is decoupled from the edge, contrarily to the zigzag type B edge.

bulk if it is terminated from the top atom, whereas the edge state can hybridize with the bulk in the opposite case (fig 8F).

2.3 Predictions for the proximity effect

In the superconducting proximity in the most common case the electrodes have the s wave pairing : Cooper pairs are formed by electrons of opposite spin. In presence of spin-orbit interaction, the spin is however not a good quantum number : it is not generically conserved along time evolution. This implies that the original s wave pairing of Cooper pairs will mix into a triplet component. As a result, the usual conversion of phase difference φ into an electrical supercurrent can now be supplemented by a conversion into spin current : this is the Edelstein effect. An inverse Edelstein effect exists as well : applying a magnetic field can result in a phase shift φ_0 of the CPR (Konschelle, Tokatly & Bergeret, 2015). Another effect can happen in materials that are very sensitive to magnetic field : the ABS can cross, thereby changing the sign of the supercurrent, or equivalently shifting the CPR by π.

If the junction is made of a material with topological protection, then one should measure ballistic transport because of the spin-momentum locking. This simple statement was not verified experimentally to our knowledge. Moreover, the spin-momentum locking implies that Andreev reflection should not mix with normal electron-electron reflection, therefore the CPR should be very sharp at $\varphi = \pi$, regardless whether the junction is in the long or the short regime.

Additionally, in this case an interesting prediction is that the current-phase relation should be 4π periodic, which is related to the existence of Majorana fermions (Fu & Kane, 2009). These are special ABS that are made of a delocalized fermion of the junction and are very interesting to observe because they should obey anyonic statistics (Kitaev, 2001). A signature of these excitations has been recently observed in non topological semiconducting nanowires with Rashba spin spin orbit coupling using tunnel spectroscopy experiments (Mourik et al., 2012) , (Albrecht et al., 2016). However, the 4π periodicity should be difficult to observe in a DC experiment due to quasiparticle poisoning (Beenakker, Pikulin, Hyart, Schomerus & Dahlhaus, 2013). A way to circumvent this is to work at finite frequencies for example by using AC Josephson effect (Bocquillon et al., 2016), or in the linear response regime by using a detection setup with a superconducting cavity as described above.

3 Organisation of the thesis

In **chapter 1**, I present the measurement of Ag nanowires. I could observe the crossover from long to short junction, with a systematic reduction of the $R_\mathrm{N} I_\mathrm{C}$ product as compared to the theoretical predictions. A reentrance phenomenon of the supercurrent vs magnetic field was also observed for Ag connected with Al electrodes, that I attribute to a competition between heating and magnetic field suppression of the order parameter inside the contacts.

The **chapter 2** is devoted to the measurement of DC transport properties of Bismuth nanowires, in the normal state and in the superconducting proximity regime. In the normal state, I show that the transport from the surfaces can be discriminated from the bulk via Shubnikov - de Haas measurements. Importantly, I show that it is diffusive in both cases. I also show a linear magnetoresistance found in a cleaved sample. I then show measurement of the supercurrent-flux dependence for different types of wires, which shows that few ABS carry the supercurrent and moreover that are confined to very narrow channels. This interpretation is corroborated by numerical simulations. I finally show a very special case of induced superconductivity by local alloying at the vicinity of sputtered Pd contact.

The CPR of Bi based Josephson junctions is shown in **chapter 3**. I start by recalling the cases of ideal junction, then I present the fabrication technique and measurement setup. The result confirm the interpretation of the previous chapter, and shows that the supercurrent is carried by two channels located on the edge of the nanowire. Besides, the application of an in plane magnetic field could help to resolve $0-\pi$ transitions, as well as signatures of φ junctions. Some measurements of the switching probability as a function of the magnetic field are also shown at the end of the chapter.

Chapter 1

Induced proximity effect in monocrystalline Ag nanowires

1 Introduction

The advances in growth techniques allows mesoscopic physics to encounter a new object : monocrystalline nanowires. These nanowires are mainly studied for their potential applications, ranging from plasmonics (Oulton et al., 2009) to transparent, flexible metallic electrodes (Langley et al., 2013), or polarization selective electronics (Park, Bae & Huh, 2016). They can be interesting from a low energy electronic transport point of view as well. First, nanowires are interesting because they have a well defined one-dimensional geometry. By further inheriting the properties of the Fermi surface of bulk crystals, they can additionally display characteristics which would be averaged out in presence of disorder, such as anisotropy of the mass tensor. Therefore, crystalline nanowires should in principle lead to the possibility of bringing the projection of the ideal bulk system along the growth axis. I will demonstrate in the following how the importance of surfaces undermines this idea. Second, thanks to their crystalline nature, one can hope to access ballistic transport. In particular, disorder free systems could be interesting in order to observe low dissipation electronic transport, and non-local in the phase coherent regime as well as interference effects. For the case of Ag nanowires studied in this chapter, I will demonstrate again that the role of disorder at the surface generally reduces the mean free path and prevents the observation of ballistic transport.

This chapter is organized in three sections. In the first section I describe the well known bulk properties of Ag, along with the growth and characterization of the Ag nanowires. In the second part I describe a comprehensive set of measurements of the superconducting proximity effect in Ag nanowires, over the entire range from short to long junction regimes. These data show a smaller value than predicted value of the $R_\mathrm{N} I_\mathrm{C}$ product.

In the third part, I explore the effect of applying an external magnetic field in particular a reentrance of the switching current, which illustrates the importance of nonequilibrium physics in SNS junctions.

2 Band structure and bulk properties

Ag crystallizes in a face centered cubic structure. It is a noble metal, and as such it has an half filled s ($5s^1$) conduction band. This band is almost spherical, however it has “necks”

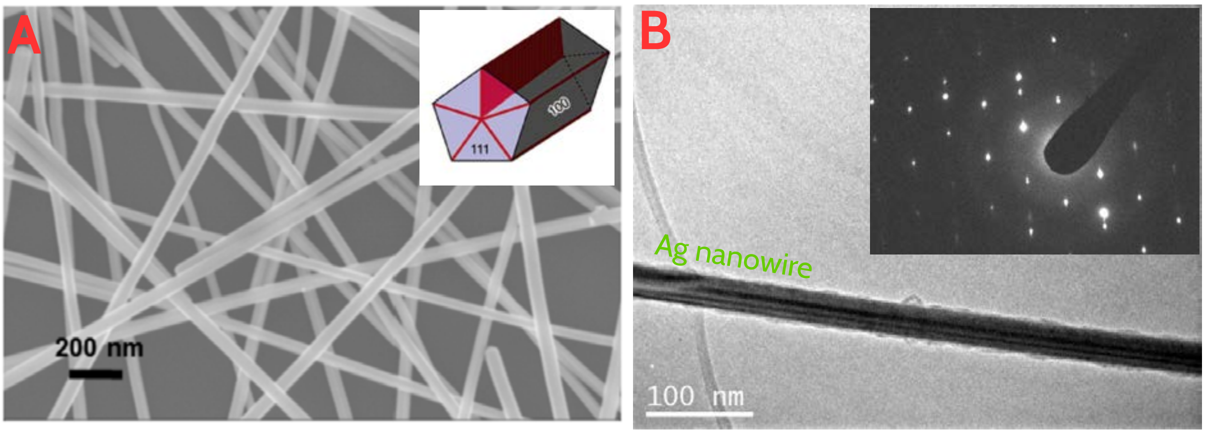

Figure 1.1: Growth and characterization of Ag nanowires. **A** : SEM image of a random network of Ag nanowires similar to those studied in this chapter. Inset : Schematics of the nanowire with pentagonal section, (111) growth axis and (100) facets. **B** : High resolution TEM of an Ag nanowire deposited on a TEM grid. Inset : Bragg peaks in reciprocal space showing the good crystallinity of the nanowires all along their length. The contrast could result from interferences patterns that are attributed to strain induced by the fivefold symmetry.

at the eight L points in the Brillouin zone. This feature implies that electrons can have non closed orbits as one applies a magnetic field and therefore its magnetoresistance is strongly anisotropic in the bulk (Ashcroft & Mermin, 1976).

Similarly to (111) surface of Au, the (111) surface of Ag should have a noticeable Rashba spin-orbit splitting, predicted to be only about 4 times smaller, which would yield a splitting in momentum space $k_{\mathrm{SO}} \simeq 0.063\,\mathrm{nm}^{-1}$. This spin splitting has not yet been observed in inverse photoemission (Nicolay, Reinert, Hüfner & Blaha, 2001), as it would require a very high resolution in energy. However, the (111) surfaces of the Bi/Ag, Au/Ag have been determined to have a large spin-orbit gap, with respectively $k_{\mathrm{SO}} \simeq 1.3\,\mathrm{nm}^{-1}$ and $k_{\mathrm{SO}} \simeq 0.23\,\mathrm{nm}^{-1}$ (Ast et al., 2007), (Popović et al., 2005). There are two interesting remarks to be made on these results. The first one is that these intermetallic alloys mostly involve Ag atoms (two atoms on three). The second is that the spin splitting of the (111) surface of the Bi/Ag alloy which is the largest ever observed $k_{\mathrm{SO}} \simeq 1.3\,\mathrm{nm}^{-1}$, not only overweighs the splitting in (111) Ag, but also the one in (111) Bi which is around two times smaller $k_{\mathrm{SO}} \simeq 0.7\,\mathrm{nm}^{-1}$ (Koroteev et al., 2004).

3 Growth and characterization

The growth of the nanowires has been done in CEA Grenoble by the team of J.P. Simonato (Langley et al., 2013). They are of typical diameter $t \simeq 50\,\mathrm{nm}$.

To fabricate our devices, a drop of solution containing nanowires is deposited on a Si/SiO$_2$ substrate. The nanowires are searched for with an optical microscope, equiped with a polarizer to enhance the contrast. The contacts are defined by e-beam lithography followed by deposition of superconducting contacts either by evaporation (Ti/Al (5nm/100nm)) or sputtering (Pd/Nb (6nm/100nm)), (Pd/ReW (6nm/100nm)) or FIB deposition (W (50-100nm)). In the case of evaporation and sputtering, an Ar$^+$ ion etching step is performed in order to remove the oxyde or residues on the nanowires surface.

The nanowires deposited on a TEM grid were characterized using high resolution TEM with Mathieu Kociak. The data performed on 12 Ag nanowires show monocrystallinity over their entire length ($25\,\mu$m) with identical (111) growth axis.

4 Transport in the normal state

4.1 Length dependence of the resistance

Similarly to the case of an optical waveguide, the Dirichlet boundary conditions for the wavefunction at the surface of a nanowire implies that only a finite number of modes can propagate through it. The number M of conducting channels depends only on the geometry and can be computed according to :

$$M = \frac{k_{\mathrm{F}}^2 S}{4\pi} \tag{1.1}$$

where S is the area of the nanowire's section, and k_{F} is the Fermi wavevector. The resistance R_{b} that would be measured in this situation if transport is ballistic is

$$R_{\mathrm{b}} = R_{\mathrm{Q}}/M \tag{1.2}$$

where R_{Q} is the quantum of resistance. Therefore, the resistance of a ballistic nanowire does not depend on its length. For an Ag nanowire of diameter 50 nm, Fermi wavelength $\lambda_{\mathrm{F}} = \frac{1}{2}\frac{hv_{\mathrm{F}}}{E_{\mathrm{F}}} = 0.49\,\mathrm{nm}$ ($v_{\mathrm{F}} = 1.36 \cdot 10^6$m/s, $E_{\mathrm{F}} = 5.49$ eV), we find $M = \frac{8}{3}\frac{\pi S}{\lambda_{\mathrm{F}}^2} = \frac{8}{3}\pi \times \pi(50\,\mathrm{nm})^2/(0.49\,\mathrm{nm})^2 = 2.7 \cdot 10^5$ channels.

Disorder leads to an increase of the resistance, scaling linearly with the length of the nanowire.

$$R(L) = R_{\mathrm{b}}(1 + L/l_{\mathrm{e}}) \tag{1.3}$$

where l_e is the mean free path. It should be noted that this equation is valid only if $k_F l_e \gg 1$. In the opposite limit $k_F l_e \ll 1$, the conducting modes become localized in the phase coherent regime $L \gg L_\varphi, L_{\mathrm{T}}$ and the resistance diverges (Abrahams, Anderson, Licciardello & Ramakrishnan, 1979).

In addition to bringing about disorder, experimental reality adds an other turmoil to this picture. The measurement of the resistance of a sample traditionally implies making an electrical contact with some metallic leads, and as a result an extra contact resistance R_c must be added

$$R(L) = R_{\mathrm{C}} + R_{\mathrm{b}}(1 + L/l_{\mathrm{e}}) \simeq R_{\mathrm{C}} + R_{\mathrm{b}}L/l_{\mathrm{e}} \tag{1.4}$$

Moreover, the quality of this interface may vary from sample to sample since they depend on the fabrication conditions, therefore R_{C} can not be taken constant in general for samples made differently.

We measured the length dependence of the resistance for different nanowires connected with different types of contacts at low temperatures $T = 100\,\mathrm{mK}$ (fig 1.2). The length of the sections were determined by SEM observation. The value of the resistances of each of these segments was determined from the jump of the resistance as the current is increased above the critical current of each section (see next part).

The data of Ag nanowires connected with Al contacts display a linear behavior (1.4) characteristic of a diffusive behavior for all the samples with a linear coefficient $1.4\,\Omega/\mu$m strikingly constant for all the samples. Given that the ballistic resistance $R_\mathrm{b} = R_\mathrm{Q}/M = 0.095\,\Omega$ for the nanowires studied here, one can extract $l_\mathrm{e} \simeq 70\,\mathrm{nm}$. This result may be surprising given the good crystallinity of the nanowires, and illustrates the importance of finite size effects : by scattering multiple times at the surface of the nanowire, the electrons longitudinal momentum is randomized. The offset R_C corresponding to the contact resistance, vary from $0 - 10\Omega$ depending on the material of the electrodes.

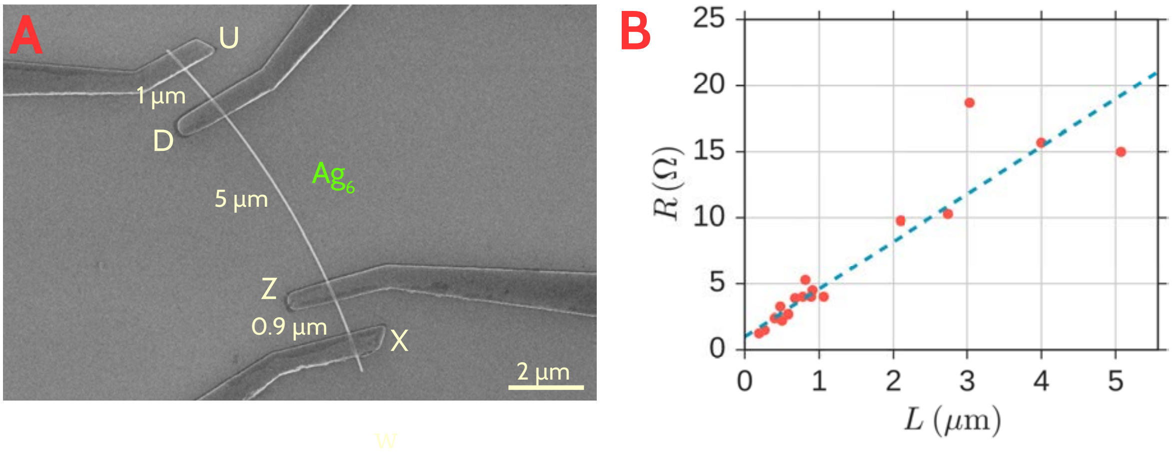

Figure 1.2: Resistance vs length for Ag nanowires connected with Al electrodes. **A** : SEM image of Ag_6. **B** : R vs L for 13 nanowires connected with Ti/Al contacts.

4.2 Temperature dependance of the resistance

As the temperature decreases, the resistance of a sample may vary depending on the dominant scattering mechanisms.

Recalling Mathiessen's rule for the transport time :

$$\tau^{-1} = \tau_\mathrm{ee}^{-1} + \tau_\mathrm{e-ph}^{-1} + \tau_\mathrm{el}^{-1} + \dots \tag{1.5}$$

then one sees that the equation for the longitudinal resistivity

$$\rho = m\tau^{-1}/ne^2 \tag{1.6}$$

can be interpreted as the equivalent serie resistance corresponding to each individual process.

If the dominant mechanism is electron-phonon scattering, then at temperatures lower than the Bloch-Gruneisen temperature T_BG, the resistivity scales as $\rho = \rho_0 + \beta T^5$. We could measure the temperature dependence of the sample Ag_8 of length $L = 3\,\mu\mathrm{m}$ contacted with FIB deposited W electrodes, and sample Ag_6 of length $L = 5\,\mu\mathrm{m}$ contacted with Al electrodes. Both samples displayed a T^5 law at low temperatures (fig 1.3). This means that the dominant inelastic scattering mechanism above 4K is the electron-phonon interaction.

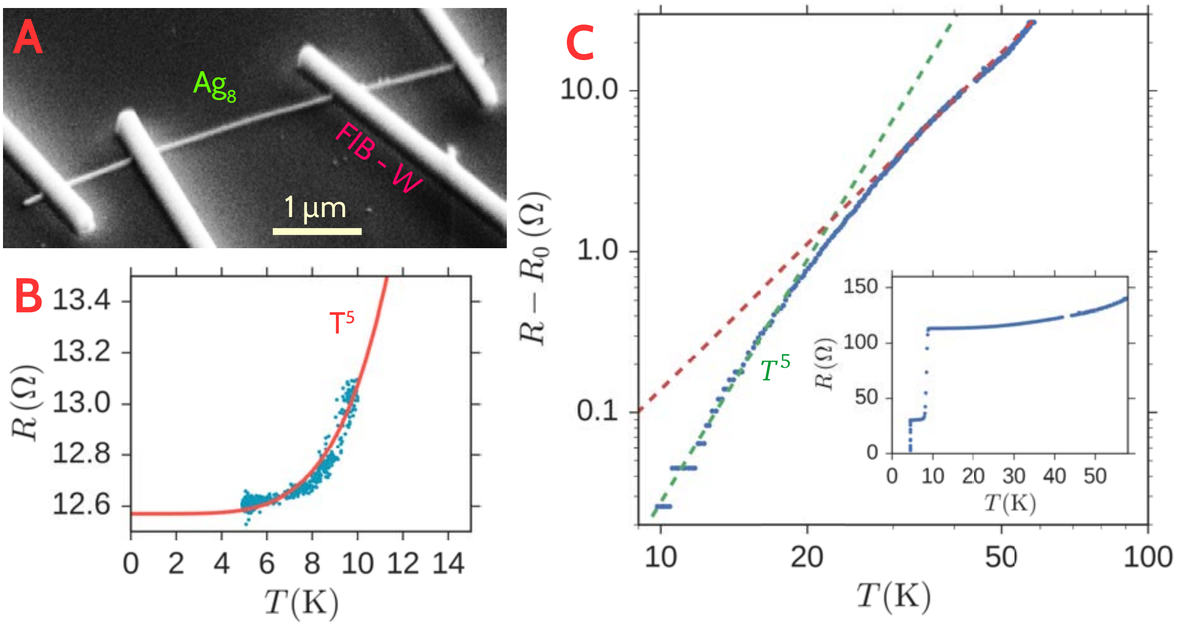

Figure 1.3: **A**: SEM image of the Ag nanowire connected with FIB electrodes. **B**: Temperature dependence of the resistance, measured in four probe configuration. A resistance jump of 85 Ω at 10 K indicates the superconducting transition of the contact region. The second jump of 25 Ω at 4 K is related to the induced proximity effect in the nanowire. **C**: Temperature dependence of the resistance for the sample Ag_8. The resistance is subtracted from the value of the resistance of the contact R_0 taken just before the transition to the superconducting state (inset). The result is plotted in log-log-scale. A T^5 law is represented for $T < 20K$ in green dotted lines. A T^3 law for $T > 20K$ is represented in red dotted lines. The latter is possibly an artefact resulting from a bad calibration of the thermometer at too high temperatures.

	$L \ll l_e$	$L \gg l_e$
$L \ll \xi_S$	$\pi M \frac{\Delta}{h} \sim 1$	$2.07 M \frac{\Delta}{h} \frac{l_e}{L} \sim 1/L$
$L \gg \xi_S$	$2M \frac{e v_F}{L} \sim 1/L$	$1.15 M \frac{e v_F}{L} \left(\frac{l_e}{L}\right)^2 \sim 1/L^3$

Table 1.1: Scaling of $I_C(L)$ for the short and the long junction limit for the diffusive and ballistic regimes.

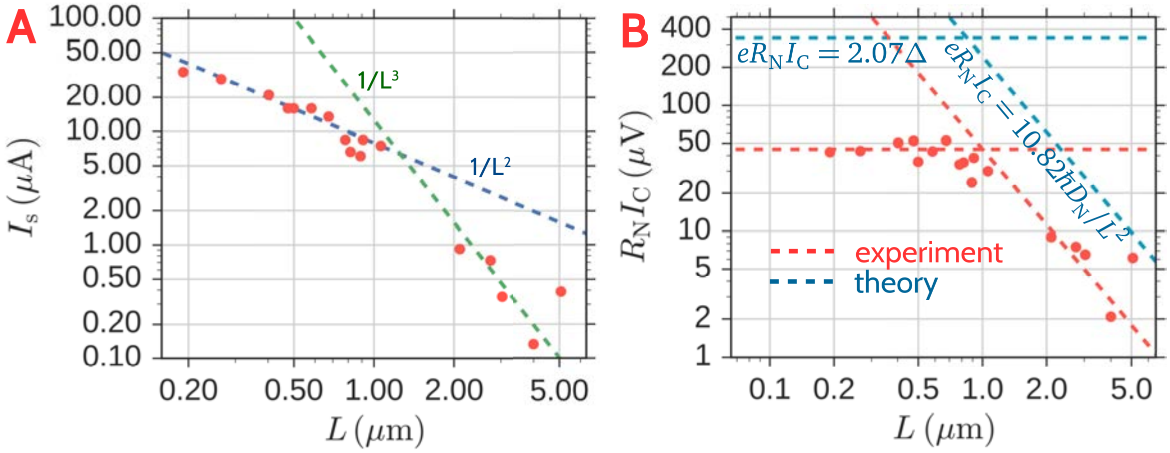

Figure 1.4: Crossover from short to long junction. **A**: $I_C(L)$ measured in two probes configuration at 100 mK. **B**: $R_N I_C$ product for different lengths. Dashed blue lines : Theoretical fit corresponding to the short diffusive junction limit $R_N I_C = \Delta_{Al} = 165\,\mu$V and long diffusive junction limit $R_N I_C = 10.82 E_{Th}$.

5 Superconducting proximity effect

5.1 Full range of proximity effect from short to long junction

We have induced superconductivity by proximity effect in a total of 27 Ag nanowires based junctions that we connected with superconducting electrodes of different materials. I will now focus on the 17 junctions connected with Ti/Al electrodes. The measured supercurrents range from 100 nA to 50μA for junction of lengths ranging from 5μm to 190nm. Thanks to this wide range of parameters, we could compare the value of the supercurrent to theoretical predictions.

Two regimes can be distinguished : the short junction limit where the energy scale of Andreev bound states is given by the order parameter Δ, and the long junction limit, where it is given by the Thouless energy $\epsilon_T = \hbar v_F/L$ for clean junctions and $\epsilon_T = \hbar D_N/L^2$ for diffusive ones. The characteristic length scale separating the two regimes is the superconducting coherence length $\xi_S = \hbar v_F/\Delta$ for the ballistic regime and $\xi_S = \sqrt{\hbar D_N/\Delta}$ for the diffusive one. Depending on how the length L of the junction compares with ξ_S and the mean free path l_e, one has different scaling laws for the supercurrent $I_C(L)$. Importantly, in the diffusive regime (which is the case of our Ag nanowires), this scaling is $I_C \sim 1/L$ for the short junction limit and $I_C \sim 1/L^3$ for the long junction limit as shown in the following table.

We could observe the crossover from the short junction limit to the long junction limit by measuring the critical current as a function of the junctions lengths (figure). From the crossover located at $L_{Cr} = 1\,\mu$m that is theoretically given by $\sqrt{10.82\hbar D_N/2.07\Delta}$, one can extract the coherence length $\xi_{\mathrm{S}}^{\mathrm{N}} = 0.43\,\mu m$ which is close to the estimated diffusive value $\xi_{\mathrm{S}}^{\mathrm{N}} = \sqrt{\hbar D_{\mathrm{N}}/\Delta} = 0.36\mu\mathrm{m}$, with $D_{\mathrm{N}} = v_{\mathrm{F}} l_{\mathrm{e}}/3 = 0.032\,\mathrm{m}^2/\mathrm{s}$. However, the value of the supercurrent per channel, measured by the $R_{\mathrm{N}} I_{\mathrm{C}}$ product was significantly lower than the predicted values. This reduction could be explained by a weakly induced superconductivity by our Al contacts of size $w \simeq 150\,\mathrm{nm}$ comparable to the coherence length inside the superconducting electrodes $\xi_{\mathrm{Al}} = \sqrt{\xi_{0,\mathrm{Al}} l_{\mathrm{e}}} \simeq 100\,\mathrm{nm}$. To conclude, let us mention that a systematic reduction of the $R_{\mathrm{N}} I_{\mathrm{C}}$ product has also been observed in graphene (C. Li, Guéron, Chepelianskii & Bouchiat, 2016), although it could not been explained by an inverse proximity effect in that case.

5.2 Reentrant proximity effect in Ag nanowires

We have measured the magnetic field dependence of the switching current in four probes and two probes geometry. A first difference between the two probes and four probes geometry is trivial : the two probes geometry includes the behavior of the entire superconducting electrodes leading to the sample. This is shown in (fig 1.6) where an abrupt jump is observed at 50 G which corresponds to the critical field of the large area $300\mu\mathrm{m} \times 300\mu\mathrm{m}$ Al pads. The critical field $B_0 = 300\,\mathrm{G}$ of the Al electrode closest to the Ag wire is larger by a factor ξ/w. This is the relevant magnetic field limiting the induced supercurrent in these narrow Ag wires. The second difference is more unexpected : in the four probes geometry the switching current does not decay monotonously with magnetic field as expected and observed in the two probes geometry. Surprisingly, it first increases with field up to about 200 G before decreasing again.

This non monotonous behvior is also observed for the retrapping current (from the normal to the superconducting state) both in 2 probe and 4 probe measurements. The difference between the switching and the retrapping current is known to be due to Joule heating that prevents hot quasiparticles from cooling and thus prevents the junction from returning to the superconducting state. This therefore suggests that non equilibrium effects may cause this non monotonous field dependence. More specifically, we relate this effect to the well known enhancement of pair breaking processes in superconductors by a magnetic field.

We assume that a small normal part exist at the vicinity of the contact, leading to Joule heating $R_{\mathrm{qp}} i^2$. We identify the corresponding energy $R_{\mathrm{qp}} i^2 \tau_{\mathrm{R}}$ lost on a timescale τ_{R} to the reduction of Josephson energy $\phi_0\,(i_0 - i)$, where τ_{R} is the characteristic time conversion of quasiparticles into Cooper pairs inside the junction (fig 1.7). Besides, we also suspect that the Joule effect depends on the length of the normal section in series with the Josephson junction considered.

Therefore, the switching current is solution of a balance equation

$$R_{\mathrm{qp}} i^2 \tau_{\mathrm{R}} = \phi_0\,(i_0 - i) \tag{1.7}$$

yielding

$$i(B) = i_0(B) \left(\frac{-1 + \sqrt{1 + 4\kappa^2 \tilde{\tau}_R(B)}}{2\kappa^2 \tilde{\tau}_R(B)} \right) \tag{1.8}$$

where I introduce the dimensionless magnetic field dependent recombination time $\tilde{\tau}_{\mathrm{R}}(B) = \tau_{\mathrm{R}}(B)/\tau_{\mathrm{R}}(0)$, and the dimensionless quantity $\kappa^2 = R_{\mathrm{qp}} \tau_{\mathrm{R}}(0) i_0/\phi_0$. The magnetic field dependent critical current $i_0(B)$ corresponds to the the one that would be measured without

Joule effect. A very simple choice for $i_0(B)$ modelling the decay of the supercurrent due to the depairing field induced inside the contact is

$$i_0(B) = i_0(0)\left(1 - \left(\frac{B}{B_0}\right)^2\right) \tag{1.9}$$

where B_0 is the characteristic magnetic field of the decay. On the other hand, the B dependence of $\tau_{\mathrm{R}}(B)$ is given by

$$\tau_{\mathrm{R}}(B)^{-1} = \tau_{\mathrm{R}}(0)^{-1}\left(1 + \left(\frac{B}{B_1}\right)^2\right) \tag{1.10}$$

which means that τ_{R} gets shorter as the magnetic field gets higher. The zero field recombination time $\tau_{\mathrm{R}}(0)$ is about $1 - 10 \cdot 10^{-9}\,\mathrm{s}$ in Al (Quay, Weideneder, Chiffaudel, Strunk & Aprili, 2015). There are three adjustable parameters in this fit. The magnetic field scale B_0 is adjusted independently from the decay of the supercurrent at large fields. On the other hand B_1 represents the dependence of the recombination time on the magnetic field and is adjusted from the reentrant part of the curve (positive $i(B)$ slope). Finally, the remaining parameter κ^2 measures the strength of the reentrance effect. This theory agrees qualitatively with the data (fig 1.7), leading to $B_0 \simeq 350\,\mathrm{G}$, $B_1 = 0.14 B_0$ and $\kappa^2 = 2.5$. This leads to $R_{\mathrm{qp}} \simeq 0.1\,\Omega$. The characteristic field B_0 is understood as the enhancement of the critical field of the contact of width w due to finite size effect $B_0 \simeq B_{0,\mathrm{bulk}}\xi/w \simeq 200\,\mathrm{G}$. On the other hand, the charactetistic field $B_1 = 50\,\mathrm{G}$ of the reentrance rather matches the bulk value, without the enhancement effect mentionned above. This could signify that the area over which the recombination takes place actually goes up to the large contact pad, which is probably the only part of the Al contacts that is well thermalized to the phonons of the substrate, given its large area.

A systematic study on all the sections of Ag_{10} as well as a more accurate description is under development.

5.3 Conclusion

We measured the electronic transport properties of crystalline Ag nanowires junctions connected with Al contacts. In the normal state, from the length dependence of the resistance, we showed that these junction are diffusive, with a mean free path $l_{\mathrm{e}} \simeq 70\,\mathrm{nm}$, of the order of the nanowires diameter $\varnothing \simeq 50\,\mathrm{nm}$, indicating a finite size limited diffusion. This result, which seems surprising given the high purity and crystallinity of the bulk of the nanowires, stresses the importance of surface scattering in nanowires of small dimensions.

In the superconducting proximity effect regime, we observed the crossover between the short and the long junction from the measurement of the critical current, and deduce $\xi_{\mathrm{S}}^{\mathrm{N}} \simeq 0.4\,\mu\mathrm{m}$. However, a significant reduction of the $R_{\mathrm{N}} I_{\mathrm{C}}$ product compared to the theory is observed similarly in both regimes, an effect that was observed in other systems such as graphene, and whose interpretation is yet still debated.

Additionally, we observed a surprising reentrance of the critical current as a function of the magnetic field in four probes geometry. We modelled this magnetic field reentrance behaviour by a Joule effect that is compensated by quasiparticle recombination whose rates increases as a function of the magnetic field. This model actually states that a superconductor gets weaker in presence of a bias current, due to the Joule effect. A more quantitative analysis is under development.

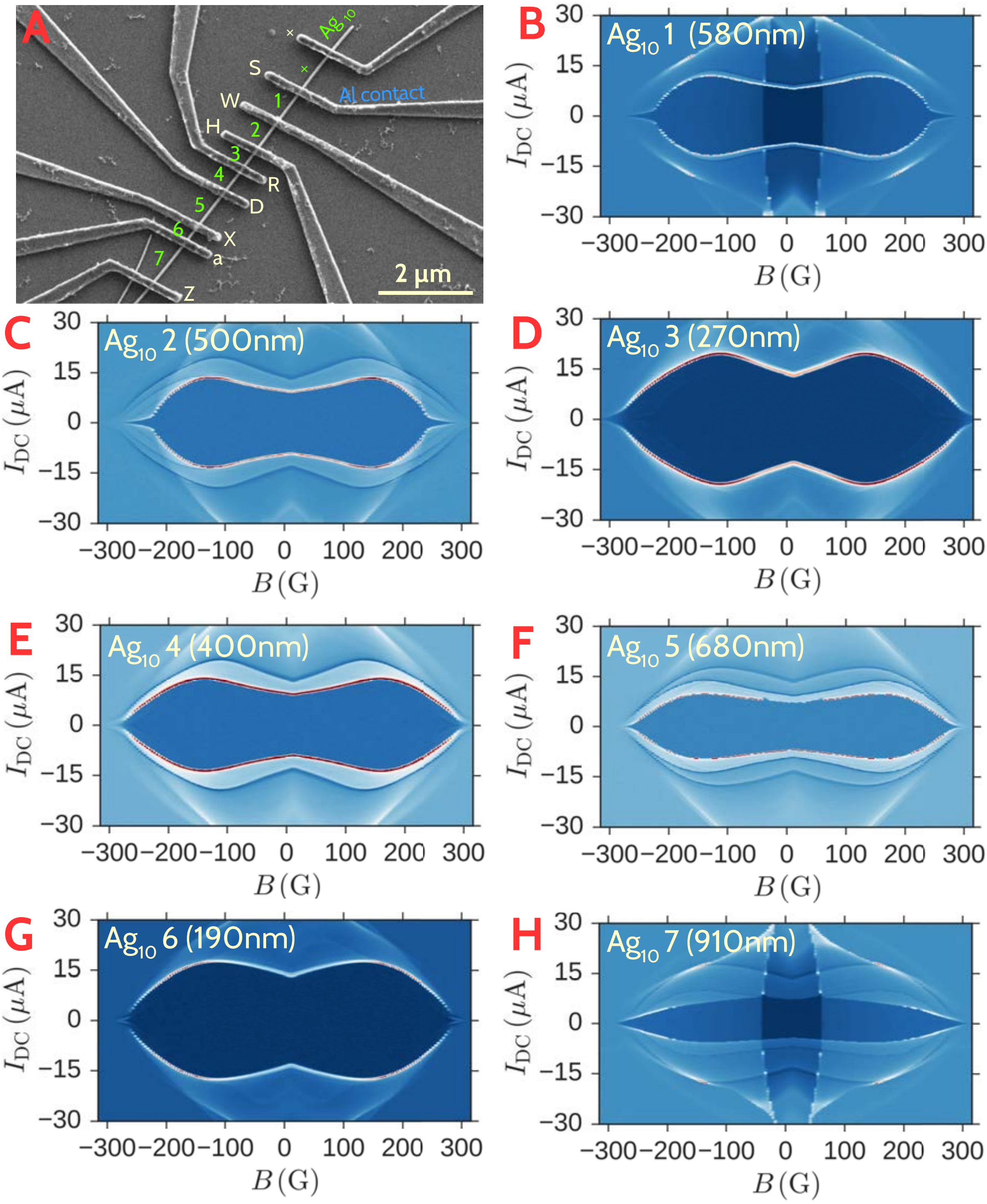

Figure 1.5: Reentrance of the supercurrent in a magnetic field for sample Ag_{10}. **A** : SEM image of the nanowire Ag_{10} contacted with Ti/Al electrodes along with the sections and the contacts names. The junction and contact marked with a cross were not connected. **B-H** : Colorplot of the dv/di of the different sections 1-7 marked on the SEM image as a function of the magnetic field B and the bias current I_{DC}.

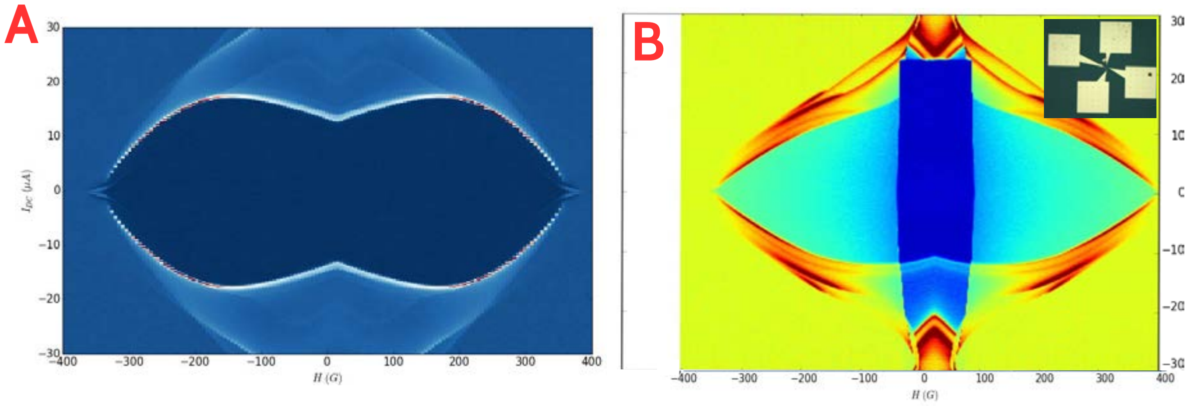

Figure 1.6: Critical current of $Ag_{10}6$ vs bias current and magnetic field for the two probes and four probes geometry. **A** : Four probes measurement **B** : Two probes measurement. The jump of critical current at 50 G is attributed to the superconducting transition of the large contact pad. Inset : optical image showing the large contacts ($300\mu m \times 300\mu m$) pads used for bonding to the sample holder of the dilution fridge.

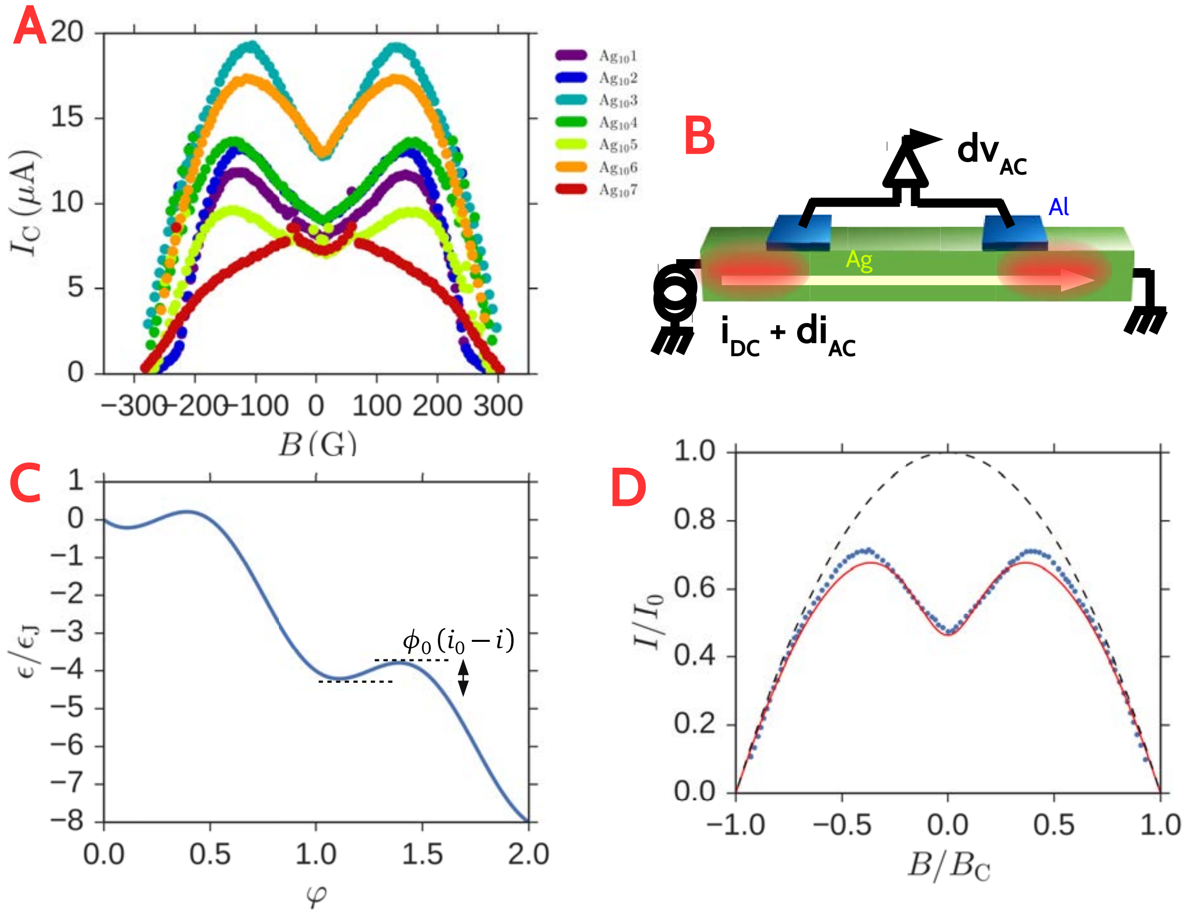

Figure 1.7: Model for the reentrance. **A** : Magnetic field dependence of the switching current for the different sections of Ag$_{10}$. The larger current correspond to smaller sections lengths. Note that Ag$_{10}$1 and $Ag_{10}7$ are measured in a 3 probes setup whereas all the other are measured in a 4 probes setup. **B** : Schematics of a measured section in four probes geometry. The injected quasiparticules flow is recombined into Cooper pairs inside the contact. **C** : Tilted washboard potential model for the current biased Josephson junction. The energy is measured in the units of the Josephson energy $\phi_0 i_0$ of the junction. **D** : Fit of the field dependent critical current on Ag$_{10}$4 assuming a field dependent recombination time of quasiparticles into Cooper pairs (see text).

Chapter 2

Transport properties of Bi nanowires in the normal and induced superconducting state.

In this chapter, I describe DC transport measurements of Bi nanowires in the normal state and the proximity effect regime, starting with a review of the electronic properties of Bi along with the description of the growth and characterization of the nanowires.

1 Introduction

The route towards the control and manipulation of the spin degree of freedom in electronic circuits has naturally led research to focus on metals and semiconductors with strong spin orbit interactions such as (In,Ga)As 2DEGs (Kato, Myers, Gossard & Awschalom, 2004) or Pt (Edwards, Ulrichs, Demidov, Demokritov & Urazhdin, 2012). In a subsequent effort to obtain an all electric quantum coherent control of the spin, nanowires quantum dots with strong spin orbit were proposed (Trif, Golovach & Loss, 2008). One dimensional systems such as nanowires can indeed prove to be interesting due to the importance of quantum effects, as strikingly observed for example through conductance quantization. The addition of superconducting proximity effect on these systems has also drawn a lot of attention due to the prediction that they could host anyonic quasiparticles near the contacts as one apply a magnetic field parallel to the nanowire, which are called Majorana fermions (Kitaev, 2001). A lot of efforts have been devoted to this search, focusing mainly on InAs and InSb semiconducting nanowires as potential candidates (Mourik et al., 2012). Bi nanowires could prove to be ideal candidates as well, due to their exceptional properties in addition to the presence of a very large spin orbit coupling.

Bismuth is one of the most studied compounds and is yet still not fully understood. It was the material where were first discovered diamagnetism, the Seebeck effect, the Nernst effect, Shunikov de Haas oscillations, and de Haas - van Alphen oscillations (Fuseya, Ogata & Fukuyama, 2015). Recently, a nematic phase was observed in Bi using magnetoresistance measurements (Zhu, Collaudin, Fauqué, Kang & Behnia, 2012) and was directly imaged through the observation of the Landau levels wavefunctions in STM (Feldman et al., 2016).

Bi nanowires were first studied due to their potential applications in thermoelectricity (Heremans & Thrush, 1999), although they may have now been supplanted Bi_2Te_3 (Zhou, Jin, Seol, Li & Shi, 2005) or even Si nanowires (Boukai et al., 2008). A measurement of the resistance in a magnetic field parallel to the nanowire displayed oscillations, indicative of a surface dominated transport (Konopko, Huber, Nikolaeva & Burceacov, 2013). The presence of strong spin orbit interactions has been observed experimentally through weak localization measurements (Kim et al., 2014). Finally, many studies displayed superconductivity in disordered Bismuth nanowires (Tian et al., 2006), which reinforce the conception that small modification of the structure of Bi can lead to a superconducting behavior.

On the other hand, little attention has been paid to crystalline Bi nanowires in the regime of superconducting proximity effect. This study is therefore interesting first to check the possibility that Bi nanowires are not intrinsically superconducting at zero magnetic field and low temperatures. Second, proximity effect can be used as a complementary tool in transport to reveal some information on the states carrying the supercurrent. Finally the presence of strong spin orbit is predicted to induce triplet superconducting correlations that could have strong consequences in transport such as very long spin lifetimes (Linder & Robinson, 2015).

This chapter is organized in five sections. I summarize the known properties of the bulk in the first section. I will also introduce the surface states of Bi, that are of great importance for the study of Bi nanowires. In the second section, I describe the growth and characterization of the nanowires. In the third section I describe how the measurement of the magnetoresistance in the normal state can reveal transport properties such as transport time, the effective masses, and finally the effective dimensionality of the system. In the fourth section I describe an experiment showing that superconductivity can be fully induced in Bi using normal metallic electrodes made of Pd thanks to local alloying at the interface between Pd and Bi. Finally, I will show a striking superconducting proximity effect in magnetic field along with different interpretations.

2 Crystal and band structures

2.1 Bi bulk

Bi crystallizes in rhombohedral structure (fig 2.1A) with the space group R$\bar{3}$m. It belongs to the group V semi-metals and thus has an odd number of electrons in its outer shell ($6s^2 6p^3$) and therefore should be metallic. A Peierls distortion of the lattice leads to a halving of the first Brillouin zone and an opening of a gap occurs, which would therefore result in an insulating behaviour (Fuseya, Ogata & Fukuyama, 2015). However, because this distortion is very weak, the band structure is that of a semi-metal. This means that it has pockets of electrons and holes which are close to compensation (fig 2.1C). This semi-metal behavior implies unusual bulk properties : a very low carrier density : $n = p = 2.7 \cdot 10^{17}\,\mathrm{cm}^{-3}$, a very low anisotropic effective mass. Moreover it has a very large g factor. Furthermore, the closeness of its bands leads to a very strong diamagnetism (Fukuyama & Kubo, 1970) that I will not discuss here.

- Fermi surface properties The effective mass tensor is very anisotropic and depend strongly on the band. They have been determined experimentally (Smith, Baraff & Rowell, 1964) using Shubnikov-de Haas oscillations measurements, and are given in the binary, bisectrix, trigonal coordinate system (fig 2.1A,B) by

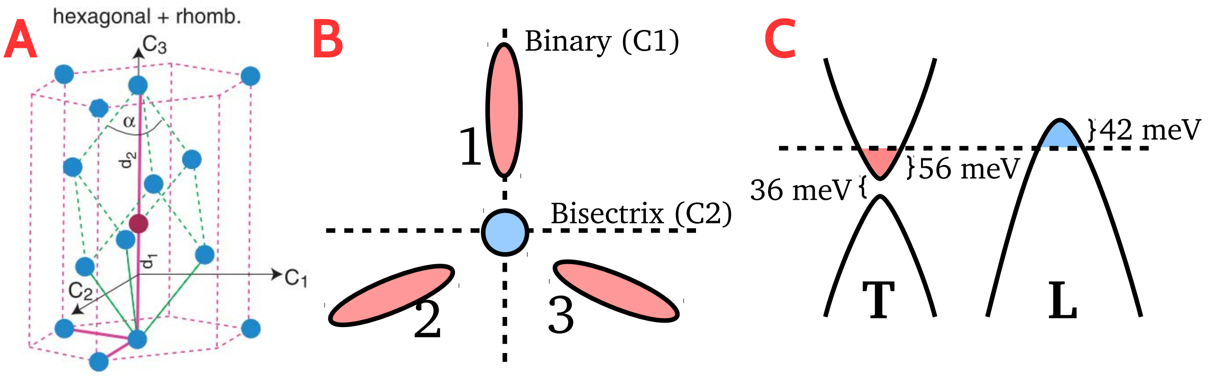

Figure 2.1: Atomic structure of Bi and cartoon of the band structure. **A**: Atomic structure of Bi in the hexagonal cell (pink dotted lines) and the rhombohedric cell (green dotted lines). Taken from (Hofmann, 2006). **B** : Electron pockets ellipsoids represented with respect to the symmetry axis. The pink pockets designates electron pockets, and the blue pocket is the hole pocket. **C** : Schematic view of the dispersion relation near the T point and the L point of the Brillouin zone.

Table 2.1: Fermi velocity for the different axes

$(10^6\mathrm{m/s})$	$v_{\mathrm{F},1}$	$v_{\mathrm{F},2}$	$v_{\mathrm{F},3}$	$\langle v_{\mathrm{F}} \rangle$
Electrons	0.089	1.000	0.750	0.613
Holes	0.252	0.838	0.838	0.643

$$\mathbf{m}^*_{\mathbf{e,1}} = \begin{pmatrix} 0.00521 & 0 & 0 \\ 0 & 1.20 & -0.09 \\ 0 & -0.09 & 0.0204 \end{pmatrix}, \\ \mathbf{m}^*_{\mathbf{e,2}} = \begin{pmatrix} 0.901 & -0.517 & 0 \\ -0.517 & 0.304 & -0.09 \\ 0 & -0.09 & 0.0204 \end{pmatrix}, \quad \mathbf{m}^*_{\mathbf{e,3}} = \begin{pmatrix} 0.901 & 0.517 & 0 \\ 0.517 & 0.304 & -0.09 \\ 0 & -0.09 & 0.0204 \end{pmatrix} \tag{2.1}$$

where 1, 2, 3 label the electron pockets (fig 2.1B). For the hole band :

$$\mathbf{m}^*_{\mathbf{h}} = \begin{pmatrix} 0.064 & 0 & 0 \\ 0 & 0.064 & 0 \\ 0 & 0 & 0.69 \end{pmatrix} \tag{2.2}$$

The components of the Fermi velocities are given by (Édel'man, 1977)

This anisotropy of masses and velocities implies that there is a large variety of carriers in Bi, each of them having different Fermi wavelengths λ_{F}, given by

$$\lambda_{\mathrm{F}} v_{\mathrm{F}} = \frac{h}{m_e m^*} = \frac{7.12}{m^*} 10^{-4}\,\mathrm{m^2/s} \tag{2.3}$$

In Bi, one has typically λ_{F} is 50 nm. This can lead to a finite size driven semimetal insulator transition for sufficiently thin nanowires whose transverse dimensions are smaller than λ_{F}.

The mobility tensor, on the other hand has been measured from quantum oscillations in magnetoresistance measurements in a single crystal at 20 K, and yields (Collaudin, 2014)

$$\boldsymbol{\mu}_{e,1} = \begin{pmatrix} 550 & 0 & 0 \\ 0 & 10 & -34 \\ 0 & -34 & 300 \end{pmatrix} \tag{2.4}$$

in $\mathrm{m}^2/\mathrm{V}/\mathrm{s}$ units, for the electron pocket 1, the other being deduced by $\pm 2\pi/3$ rotations with respect to the trigonal axis, and

$$\boldsymbol{\mu}_{h} = \begin{pmatrix} 11 & 0 & 0 \\ 0 & 11 & 0 \\ 0 & 0 & 20 \end{pmatrix} \tag{2.5}$$

for the hole pocket.

From this tensor, and the effective mass tensor, one can obtain the diffusion time tensor

$$\boldsymbol{\tau} = \frac{1}{e}\boldsymbol{\mu} \cdot \mathbf{m}^* \tag{2.6}$$

which is anistropic as well. Interestingly, the mean free path $l_\mathrm{e} = v_\mathrm{F}\tau$ is isotrope and nearly constant for all the bands. This means that regardless the type of carrier, the diffusion mechanisms acts the same way on them.

- g-factor

  The g tensor is related to the effective mass as

$$\mathbf{g} = \frac{\mathbf{m}}{\det(\mathbf{m}^*)} \tag{2.7}$$

  It can yield g factors as high as 1000 (Fuseya, Zhu et al., 2015). This expression is only valid in the presence of strong spin orbit interaction, contrarily to the case of graphene which has $g \simeq 2$ but a vanishing mass at the Dirac point.

- Atomic and bulk spin orbit coupling

  Being a heavy element, Bi has a strong spin-orbit coupling. Indeed, the atomic spin-orbit lifts the spin degeneracy of the last orbitals into two levels $6p^{1/2} - 6p^{3/2}$, with a large energy difference. Assuming the amplitude of the atomic spin-orbit coupling (Claude Cohen-Tannoudji, 1973)

$$\begin{aligned} W_\mathrm{SO} &= \frac{1}{2m_\mathrm{e}^2c^2}\frac{\partial_r U}{r}\mathbf{L}\cdot\mathbf{S} \\ &= \frac{1}{2m_\mathrm{e}^2c^2}\frac{Z_\mathrm{eff}e^2}{4\pi\epsilon_0 r^3}\mathbf{L}\cdot\mathbf{S} \\ &= \alpha^2 Z_\mathrm{eff}\mathrm{Ry}\left(\frac{a_0^3}{r^3}\right)\left(\frac{\mathbf{L}\cdot\mathbf{S}}{\hbar^2}\right) \end{aligned} \tag{2.8}$$

where $\alpha \simeq 1/137$ is the fine structure constant, $\mathrm{Ry} \simeq 13.6\,\mathrm{eV}$ is the Rydberg constant, $a_0 \simeq 0.5\,\text{Å}$ is the Bohr radius, $Z_{\text{eff}} = 13.84$ is the effective nuclear charge for the 6p shell of Bi, then one has an energy difference

$$\Delta E \sim \alpha^2 Z_{\text{eff}}^4 \left(\frac{2}{n}\right)^3 \mathrm{Ry} \tag{2.9}$$

where $n = 6$ is the principal quantum number, and I estimated $\left\langle \frac{1}{r^3} \right\rangle \simeq \left(\frac{2Z_{\text{eff}}}{na_0}\right)^3$. This would yield $\Delta E \simeq 0.98\,\mathrm{eV}$, that is the same order of magnitude with the experimentally determined value $\Delta E \simeq 1.5\,\mathrm{eV}$ (Hofmann, 2006).

However, the Bi crystal is centro-symmetric, therefore in absence of any process that breaks time-reversal symmetry such as a magnetic field, the hamiltonian H for conduction electrons in Bi verifies

$$\begin{aligned} HT &= TH \\ HP &= PH \end{aligned} \tag{2.10}$$

where P and T are the inversion operator and time reversal operator respectively. Therefore if $\epsilon_{k\uparrow}$ is an eigenvalue of H, then by applying T then P, one has

$$\epsilon_{k\uparrow} \overset{T}{=} \epsilon_{-k\downarrow} \overset{P}{=} \epsilon_{k\downarrow} \tag{2.11}$$

which means that no spin-splitting of the bands should occur in absence of an external magnetic field, a property termed Kramers degeneracy.

Nevertheless, spin orbit interactions strongly affect the band structure (Liu & Allen, 1995) even though the bands are spin-degenerate.

2.2 Bi surface states

At a surface, inversion symmetry is broken and therefore a spin splitting of bands can occur. This can be understood microscopically by the appearance of an electric field on the surface, which then acts as a magnetic field in the referential frame of conduction electrons, and couples with the spin. Surface states of Bi are known to be strongly spin-split (Hofmann, 2006), as measured by ARPES (Koroteev et al., 2004), or directly by spin resolved ARPES (Hirahara et al., 2007).

Bismuth surfaces are in general metallic, with a larger effective mass, that is closer to the bare electron mass. The (111) surface which is perpendicular to the trigonal axis and is the surface of natural cleavage, the effective mass for electrons is $m^* \simeq 0.16$ and for holes $m^* \simeq 0.2$. This surface is of particular interest for quantum transport as it may host edge states.

2.3 Bi edge states

Following the observation that Bi has a strong spin-orbit coupling and has a lattice similar to the one studied by Kane and Mele, it was predicted by Murakami that the (111) surface of Bi hosts topological edge states, making it a QSH system (Murakami, 2006), which means that these edge states are protected against disorder. This was done using the tight-binding hamiltonian derived by Liu and Allen (Liu & Allen, 1995), restricted to a zigzag edges terminated bilayer, that is infinite in the bisectrix direction. This model was obtained by fitting experimental data (electron density, anistotropic effective mass tensor, Fermi energy and momenta) to those obtained from a tight binding model with sp^3 orbital configuration. From this simulation, it was found that there are three energy level crossing at the Fermi energy, which is a consequence of the existence of three outer orbitals $p_\mathrm{x}, p_\mathrm{y}, p_\mathrm{z}$ in Bi. In a subsequent refinement using ab-initio based simulations, Murakami found edge states also for the $\bar{\Gamma} - \bar{M}$ direction, that is for armchair edges (Wada, Murakami, Freimuth & Bihlmayer, 2011). The group velocity of each of these states can vary by a factor 4 depending on the crossing considered.

An STM measurement performed by the Yazdani group showed distinctive 1D features of the local density of states (LDOS) situated on the atomically defined edges of a local depression of a (111) Bi surface. Besides, the energy dispersion of the DOS at these edges follows a $1/\sqrt{\epsilon}$ law, characteristic of a 1D system. Furthermore, the improvements in energy resolution in ARPES allowed to resolve a linear crossing of energy levels in the $\bar{\Gamma} - \bar{K}$ direction, that do not disperse in the perpendicular direction and can thus be interpreted as 1D (Takayama, Sato, Souma, Oguchi & Takahashi, 2015). From this measurement, we can extract a Fermi velocity $v_\mathrm{F} \simeq 2 \cdot 10^5\,\mathrm{m/s}$, which corresponds to the least steep energy dispersion at the Fermi level found in numerical simulations. In the rest of the manuscript, we take $v_\mathrm{F} = 6 \pm 2 \cdot 10^5\,\mathrm{m/s}$.

In order to understand whether these edge states can also exist in a nanowire, one can performed numerical tight binding simulations on a 3D ribbon-like system. To do so, I used the Liu-Allen tight-binding hamiltonian, as originally studied by Murakami, on a system that is finite in two directions and infinite in the third direction. By making use of twisted boundary conditions, one can therefore study the energy dispersion relation of a ribbon-like system. This was done using the Kwant package (**?**). The local density of states (LDOS) is then computed by summing the space-dependent spectral weights on an energy window situated ±100mV around the Fermi level. Beforehand, I reproduced the result of Murakami and mapped the LDOS, showing that it is strongly enhanced on the outer atoms of the Bi bilayer (fig 2.2).

I then studied a particular geometry of nanowire with (111) top surface, similar those studied in this thesis. The growth axis was taken to be the bisectrix axis, and with rhombic transverse shape, similarly to what can be hinted from SEM and EBSD measurement (see further). This choice implies that the lateral surface has the (100) direction, which is a natural choice for a growing nanowire because it minimizes the number of dangling bonds. For this type of simulated nanowire, the LDOS also shows the existence of edge states, located at the outer edges of the nanowire, which confirms our intuition. However in this case, the spectrum is much more complicated than in the bilayer case, due to the presence of surface states that coexist with the edge states on the (100) surface, whereas they are fully localized at the (111) surface. The dependence of the LDOS with the number of bilayers in the 3D ribbon (fig 2.2) can be fitted according to

$$\rho(x) = C\left(\alpha + \mathrm{e}^{-x/0.85}\right) \tag{2.12}$$

where x is the distance from the edge state measured in bilayer number, C is a normalization factor, and $\alpha = 0.7$. This means that on the (100) surface, edges states are localized within about 0.85 unit cell (which is about 0.5 nm long) and coexist with the remaining surface states that are delocalized, and possibly diffusive in an actual nanowire. However, the local spin density shows a strong signature of spin-momentum locking all along the (100) surface (fig 2.2G), which implies that the elastic scattering for these states could be strongly reduced. Therefore, even though the reminiscent topological edge states are localized within a few atomic length, the extended states may also be in the ballistic regime.

3 Growth, preparation, connections and characterization

3.1 Growth techniques

The nanowires studied during this thesis were grown using two different techniques : electrodeposition through a polycarbonate template and sputtering on a hot surface. Other growth techniques are possible such as the so called Taylor-Ulitovsky method which consist in rapid quenching of material in the melted state (Gitsu, Konopko, Nikolaeva & Huber, 2005), aqueous chemical reduction of $BiCl_3$ guided by PVP reagent (Y. Li, Zhao, Wu & Zhao, 2016), or laser ablation through superfluid helium (Kasumov, 2016).

Polycarbonate templating

This technique makes use of a template made of polycarbonate containing pores with small diameter $\varnothing \simeq 100\,\text{nm}$ (fig 2.3A) (Huang & Fung, 2006). An electrodeposition is done through the template by applying a voltage difference between an electrode placed at the bottom of the template and an electrode placed inside the solution. The solution is prepared by dissolving Bi nitrate in water in addition to an other electrolyte. The nanowires were fabricated by G.Tsirlina and coworkers from Moscow State University. This technique has the advantage that it can make a large number of nanowires of small diameter $< 90\,\text{nm}$. However, this technique has a few drawbacks. First, the surface characterization as well as high resolution TEM imaging can prove to be difficult because of the presence of the polymer coating surrounding the nanowire. Second, some cavities can occur during the growth process (fig 2.3B).

- Sputtering on hot surface

  Using sputtering, one first grows a wetting layer of Bi, then heats the substrate at a temperature chosen close to the melting point of Bi (271.3°C). Vanadium can also be used as a base wetting layer as well as Iron. Some nanowires can then grow in some parts of the substrate. The mechanism of growth is not clear, but could be related to the release of stress caused by the mismatch in thermal expansion of SiO_2 and the wetting layer of Bi, similarly to the ON-OFF method (Kim et al., 2014), (Shim et al., 2009).

  The Bi target used for sputtering is of very high purity (99.9999%). This is important because being a semi-metal, the number of conduction electrons per atom of the crystal is small (less than one conducting electron per 10^5 atom), which explains why such a high purity is desirable. The nanowires grown by this technique are single crystals (fig 2.4).

- Deposition on substrate

  The nanowires are then dry deposited on a substrate of Si/SiO_2 (500 nm of thermal oxide) for optical imaging. Due to their small dimension as well as the low plasma frequency of Bi, a lot of variation was observed in the reflected color of the nanowire when exposed to white light. We could not however completely rely on this information to characterize their thickness or their orientation.

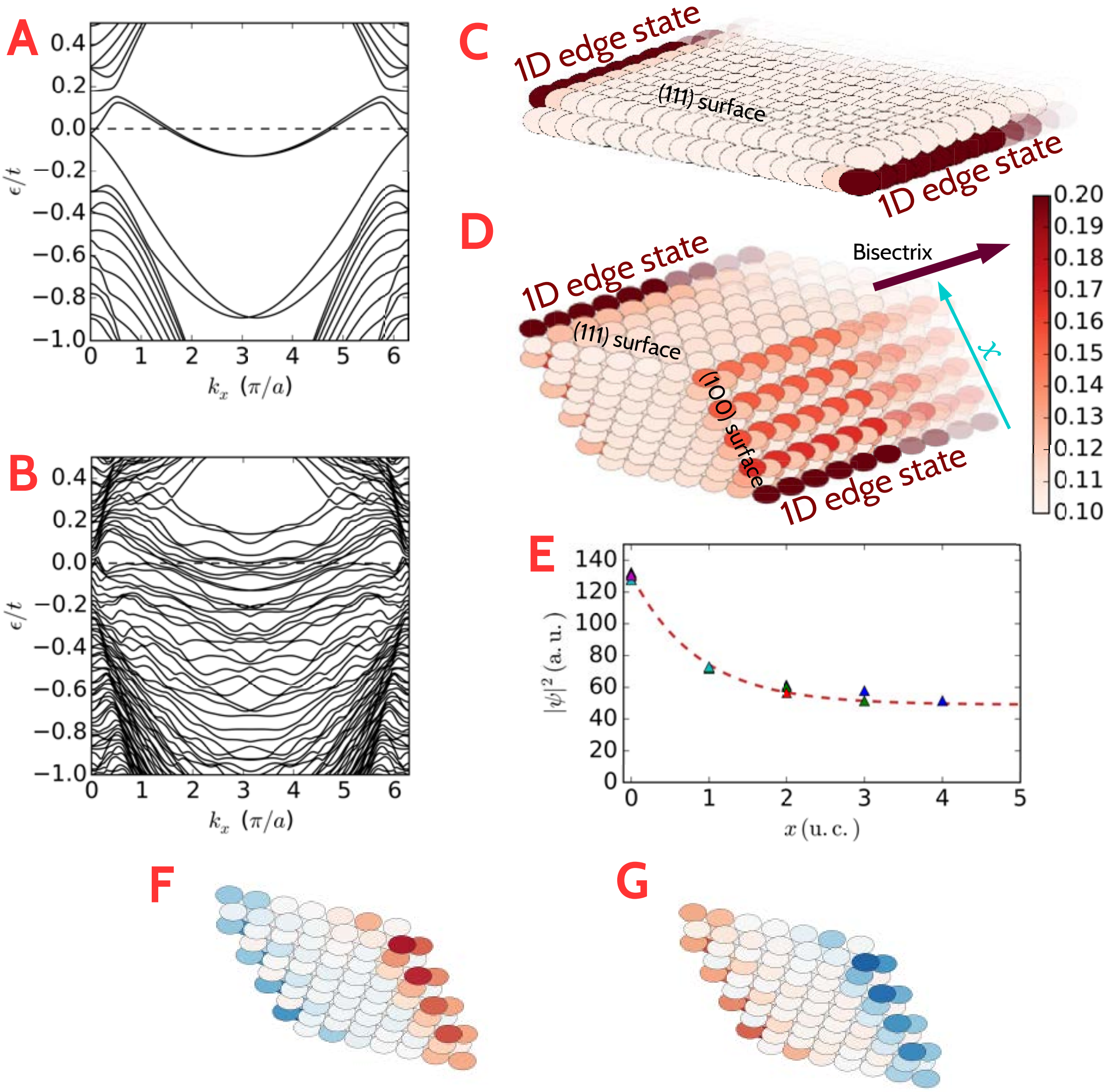

Figure 2.2: Numerical simulations on Bi nanowires. **A** Energy dispersion relation for a bilayer Bi. This is the same spectrum as the one calculated by Murakami. **B** Spectrum of the Bi nanowire obtained by stacking 5 Bi bilayers that are 7 atoms wide. **C** LDOS of the bilayer Bi.**D** : LDOS for the Bi nanowire. The units are arbitrary. **E** Non normalized LDOS at the (100) surface as a function of the distance from the edge, calculated on nanowires obtained by stacking an increasing number of bilayers. Orange dashed line : numerical fit yielding $\rho(x) \propto \left(0.7 + \mathrm{e}^{-x/0.85}\right)$. **F**,**G** : z component of the local spin density $\langle \sigma_z \rangle$ restricted for $0 < k < \pi/a$ (F) and $-\pi/a < k < 0$ (G). In blue are the negative value and in red are the positive values in arbitrary units.

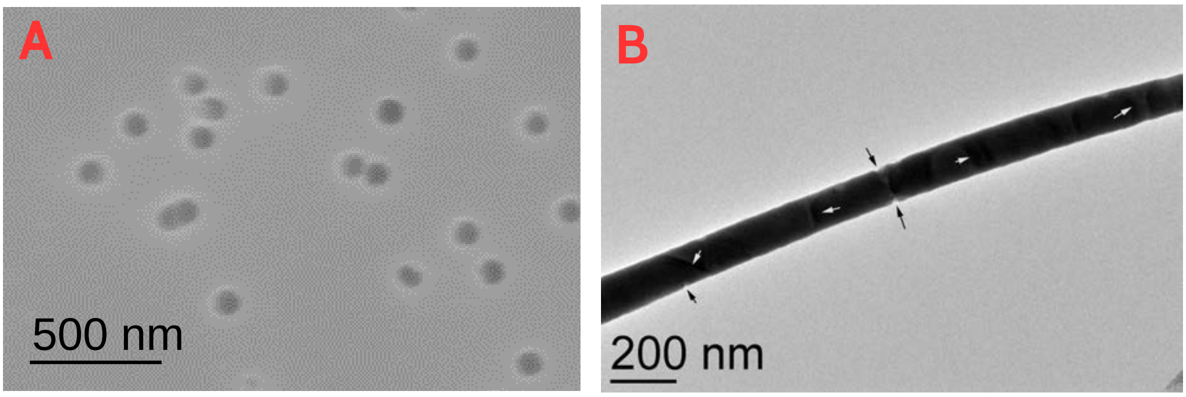

Figure 2.3: Fabrication of Bi nanowires using polycabonate templating. A: SEM image of the pores in the polycarbonate film used for the growth. B : High resolution TEM image of a typical nanowire grown by this technique. The white arrows indicate the crystal orientation, the black arrows indicate a cavity type malformations.

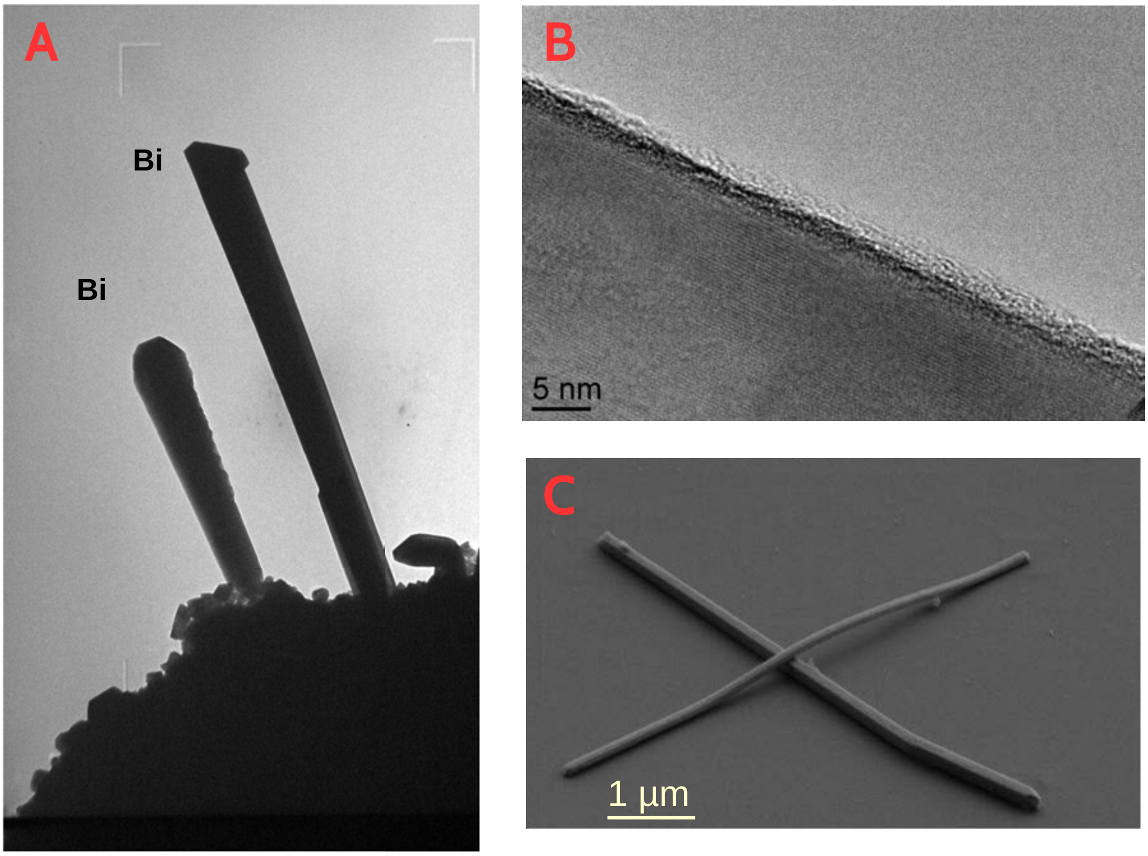

Figure 2.4: Fabrication of nanowires grown by sputtering on hot surface technique. A: TEM image of the nanowire directly after the growth process. The width of the nanowires is typically between 100 nm and 300 nm. B : High resolution TEM image of the nanowires showing their remarkable crystallinity. A thin oxide layer of less than 3 nm is visible, impeding direct electrical connection. C : TEM image of Bi nanowires deposited nanowires on a Si/SiO_2 substrate forming a cross.

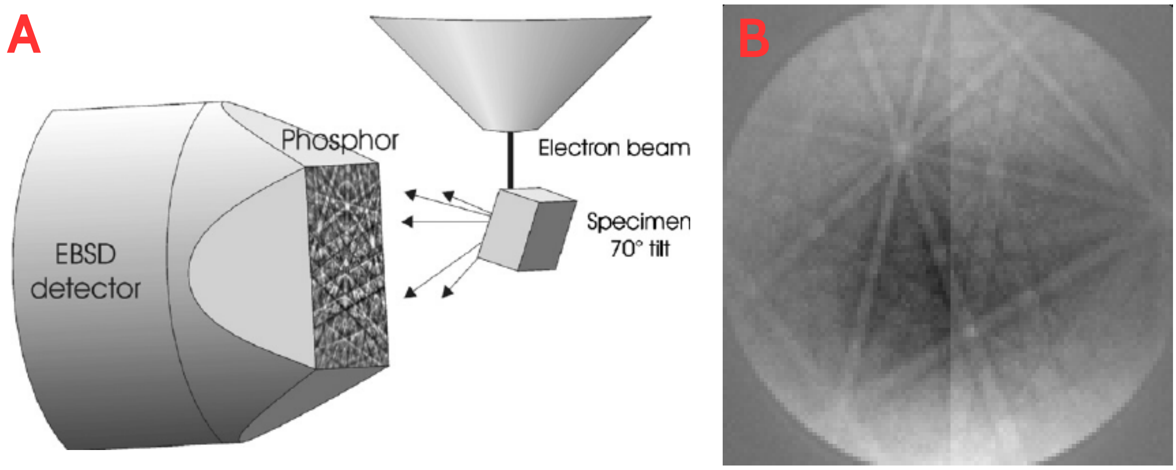

Figure 2.5: Principle of the EBSD technique. A: Schematics of the setup for EBSD detection. The sample is tilted 70° from the incident electron beam. The large detector catches backscattered electron in Bragg condition in the crystal. B: Typical diffraction pattern measured directly on a Bi nanowire, on a single image at $60\,\mu$A and $5\,$keV.

3.2 Characterization with EBSD

Besides the high resolution TEM that is used to check the crystallinity as well as the potential surface oxidation, we used an electronic diffraction technique to determine the crystalline orientation of the nanowires perpendicular to the substrate. This information can be crucial as different surfaces of Bi have very different electronic properties.

The technique uses a wide angle detector that is placed in a commercial SEM to collect the electrons that are diffracted from a sample, being in Bragg conditions with respect to the crystallographic planes. The resulting pattern, which depends on the precise position of the detector, results of the superposition of signals coming from different Kikuchi bands. In the usual case of a detector sufficiently off-centered from the beam, this pattern is formed by close parallel lines called Kikuchi lines. By fitting the pattern with the experimental data taken on a crystal with known orientation, one can recover the orientation of the surface of the sample perpendicular to the substrate. This technique was performed in collaboration with François Brisset.

3.3 Connection to electrodes

Due to the thin oxyde layer present at the surface, it is impossible to connect the nanowires without a preliminary etching step. Two techniques were employed : focused ion beam (FIB) milling followed by FIB induced CVD growth of the metal contacts, and Argon ion beam etching (IBE) in the same vacuum as the sputtering deposition. Both techniques proved to work.

- FIB deposited Tungsten

  The contacts made with FIB source used Ga^+ ions. The electrodes deposited with this technique were FIB induced CVD growth of tungsten carbide. The process results from the decomposition of $W(CO)_6$ molecule under ionic flow. The resulting superconductor has a very high critical field $H_C^2 \simeq 12\,$T and $T_C = 5.5 - 6\,$K. For all the measured nanowires, the distances between the W lines were chosen to be greater than 1 μm in order to avoid any shorting by superconducting contamination.

Indeed, when the precursor gas is decomposed by the Ga$^+$ beam, the major part is adsorbed on the substrate directly under the beam, but a small part can diffuse away from the spot. This can lead to a layer of aggregated materials such as W, C, Ga, O, which is termed contamination. If this contamination is conducting, there is a chance that it can become superconducting at low temperatures either intrinsically or by proximity effect. A previous characterization study done by Alik Kasumov shows that this can be the case if the distance between the FIB deposited W contacts is smaller than 200 nm. Away from this distance the contamination contains mainly C, and is of similar nature than the contamination that can be induced by the electron beam of a SEM. It is therefore highly resistive and does not short the connected device (fig 2.6A).

- Ion beam etching (IBE) and sputtering

  For the other technique, the contacts are defined by e-beam lithography, and then etched with IBE. The Ar etching rate for Bi was calibrated and found to be around 2 nm/s at an acceleration voltage of 200 V and $4 \cdot 10^{-4}$ mTorr. This rather large value could be related to the low melting point of Bi compared to other materials in similar conditions. Furthermore, given the appreciable diameter of the nanowires ($100 - 200$ nm), an e-beam evaporation would not be suitable. Indeed, e-beam evaporation being directional, the metal can be missing in some parts of the nanowire's contact and thus can lead to a bad electrical contact. Therefore sputtering is preferred, as it is not directional and can thus cover the whole perimeter of the nanowires.

  After this connection process, the electronic properties of Bi at the contact region are certainly strongly modified. This can have dramatic consequences, for example by locally forming an alloy, as will be described further.

3.4 Length dependence of the resistance

The measurement of the length dependence of the resistance at low temperatures can be instructive and help to determine the type of carrier dominating the transport. When a nanowire is diffusive, one can estimate the mean free path using the formula of the resistance in the diffusive case that was derived in the previous chapter

$$R(L) = \frac{R_{\mathrm{Q}}}{M}\frac{L}{l_{\mathrm{e}}} \tag{2.13}$$

Contrarily to Ag, Bi bulk is semi-metallic and hence has a large Fermi wavelength $\lambda_{\mathrm{F}} \simeq 50$ nm. On the surface however, the Fermi wavelength is smaller $\lambda_{\mathrm{F}} \simeq 4$ nm. As a result, for a Bi nanowire, the number of surface conducting channels $M_{\mathrm{S}} \equiv \frac{P}{(\lambda_{\mathrm{F}}^{\mathrm{S}}/2)}$ outweighs the number of bulk conducting channels $M_{\mathrm{B}} \equiv \frac{S}{(\lambda_{\mathrm{F}}^{\mathrm{B}}/2)^2}$, where P and S are the perimeter and the section's area of the nanowire, respectively. More quantitatively, one has

$$\frac{M_{\mathrm{B}}}{M_{\mathrm{S}}} = \frac{2\lambda_{\mathrm{F}}^{\mathrm{S}}}{(\lambda_{\mathrm{F}}^{\mathrm{B}})^2}\frac{S}{P} \lesssim \frac{2}{\sqrt{4\pi}}\frac{\lambda_{\mathrm{F}}^{\mathrm{S}}}{(\lambda_{\mathrm{F}}^{\mathrm{B}})^2}\sqrt{S} \tag{2.14}$$

where I made use of the inequality $4\pi S \leq P^2$. Consequently, in Bi nanowires of diameter $\sqrt{S} \lesssim 150$ nm, the transport is dominated by surfaces by a factor $\gtrsim 10$.

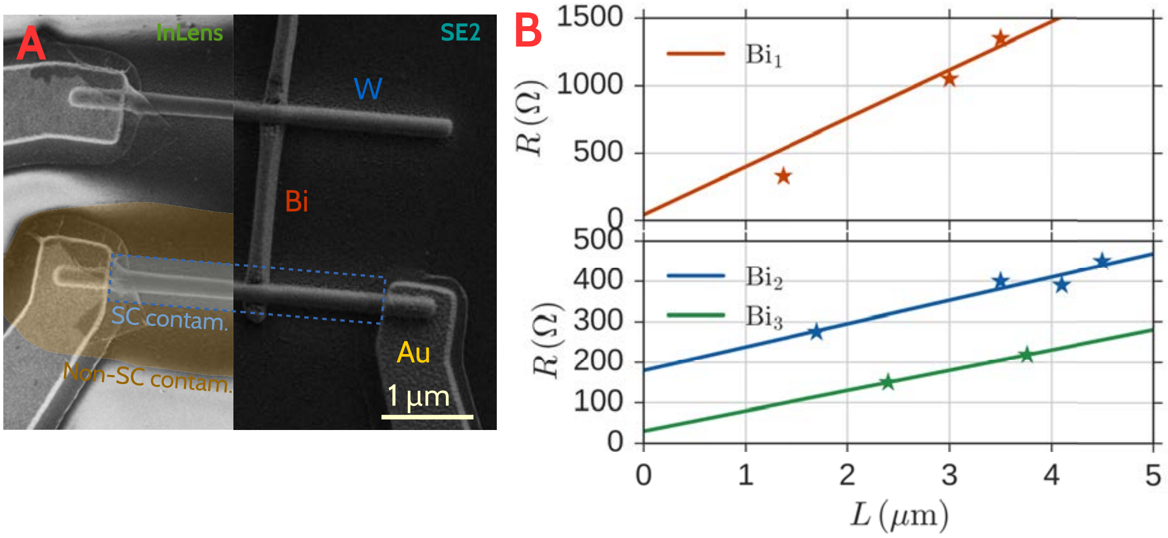

Figure 2.6: SEM image of a connected Bi nanowire and resistance vs length curve. **A** : SEM image using two different detectors. The blue shaded region of 200 nm around the contact corresponds to the possible superconducting contamination, as determined by previous characterization studies of W lines grown in the same conditions. The brown shaded region corresponds to the carbon contamination, which is very resistive. **B** : Resistance v.s. length for different sections of three crystalline Bi nanowires connected with FIB deposited W electrodes.

Furthermore, some surfaces of Bi, and in particular the (111) surface, may host only edge states but not surface states. Consequently, P can be reduced and so does the ratio $M_\mathrm{B}/M_\mathrm{S}$. Moreover, it can strongly depend on the aspect ratio of the nanowire.

We connected several nanowires with FIB deposited W, all of them having a (111) direction perpendicular to their substrate. The measurement was performed at low temperature (120 mK). For all three nanowires, the length dependence of the resistance is linear (fig 2.6) which indicates a diffusive behaviour. From these measurement, we extract $l_\mathrm{e} \simeq 200\,\mathrm{nm}$ for Bi_{32}, Bi_{33} and Bi_{34}.

4 Magnetic field behaviour in the normal state

4.1 Classical B^2 contribution

As one applies a magnetic field in addition to a voltage difference to measure the conductance of a sample, the classical trajectories of electrons deviate from straight lines, displaying a finite curvature thereby decreasing its conductance. This effect is weaker in presence of disorder, as the bending of the trajectories by a magnetic field is only meaningful for length below l_e.

If the magnetic field is small enough, one can treat it classically. The equation of motion for an electron under a magnetic field $\mathbf{B}$ and an electric field $\mathbf{E}$ is

$$\frac{\partial \mathbf{p}}{\partial t} = -e\left(\mathbf{E} + \frac{\mathbf{p}}{m} \times \mathbf{B}\right) - \frac{\mathbf{p}}{\tau_\mathrm{e}} \tag{2.15}$$

where τ_e is the elastic lifetime. In the steady state this leads to the conductance tensor defined through $\mathbf{E} = \boldsymbol{\rho}\mathbf{j}$:

$$\boldsymbol{\rho} = \rho_0 \begin{pmatrix} 1 & -\omega_\mathrm{C}\tau_\mathrm{e} \\ \omega_\mathrm{C}\tau_\mathrm{e} & 1 \end{pmatrix} \tag{2.16}$$

where $\omega_\mathrm{C} = eB/m_e m^*$ is the cyclotron frequency. The conductivity tensor follows from $[\boldsymbol{\sigma}] = [\boldsymbol{\rho}]^{-1}$

$$\boldsymbol{\sigma} = \frac{\sigma_0}{1 + (\omega\tau_\mathrm{e})^2} \begin{pmatrix} 1 & \omega_\mathrm{C}\tau_\mathrm{e} \\ -\omega_\mathrm{C}\tau_\mathrm{e} & 1 \end{pmatrix} \tag{2.17}$$

For a 2D sample, the resistivity ρ that comes into the resistance $R = \rho L/S$ finally measured, is related to $\boldsymbol{\rho}$ through a relation that depends exclusively on the geometry of the sample. As a result, a mixing of the longitudinal and transverse components in the resistivity tensor occurs. For example, in a square geometry, one has $\rho = \sqrt{\rho_\mathrm{xx}^2 + \rho_\mathrm{yy}^2} \simeq 1 + \frac{1}{2}(\omega\tau_\mathrm{e})^2$. For a sample with typically $L < w$, one will have generally

$$\frac{R(B) - R(0)}{R(0)} \sim (\omega_\mathrm{C}\tau_\mathrm{e})^2 \tag{2.18}$$

Therefore the measurement of the low field magnetoresistance provides information on the elastic time.

On the contrary, if the sample is purely 1D then no mixing occurs and one measures the component of ρ_xx without mixing with ρ_xy. Therefore no change is expected in the longitudinal magnetoresistance.

The interesting intermediate case can be treated with a multicomponent model, involving a surface and a bulk components. The equivalent resistances being in parallel, one has to compute the tensor

$$\boldsymbol{\rho} = \left(\boldsymbol{\rho_1}^{-1} + \boldsymbol{\rho_2}^{-1}\right)^{-1} \tag{2.19}$$

A mixing of the components will thus occur through this equation and a magnetic field dependence is obtained for the resulting ρ_xx. The result can be expressed in terms of the mobilities and electron densities (van Houten, Williamson, Broekaart, Foxon & Harris, 1988)

$$\frac{\Delta R(B)}{R(0)} = \frac{\sigma_1\sigma_2(\mu_1 - \mu_2)^2 B^2}{\sigma^2 + (\mu_1\mu_2 e(n_1 - n_2)B)^2} \tag{2.20}$$

This calculation shows that the magnetic field dependence results from the presence of a two component fluid, and it becomes constant if one takes $\mu_1 = \mu_2$ and $n_1 = n_2$. For low magnetic fields, one can neglect the B dependent term in the denominator.

As a result, one has

$$\frac{\Delta R(B)}{R(0)} = B^2(\mu_\mathrm{b} - \mu_\mathrm{s})^2 \frac{\sigma_\mathrm{b}\sigma_\mathrm{s}}{\sigma^2} \tag{2.21}$$

where the s and b indices are relative to the bulk and surface components. For the case of Bi, the surface density is much higher than the bulk density and the surface resistivity is smaller than for the bulk.

Moreover, for a 1 micron long wire of width 200 nm and height 100 nm, the two non-topological (100) surfaces contain roughly 100 times more carriers than the bulk. Thus we can assume that the greatest contribution to normal state conductance comes from

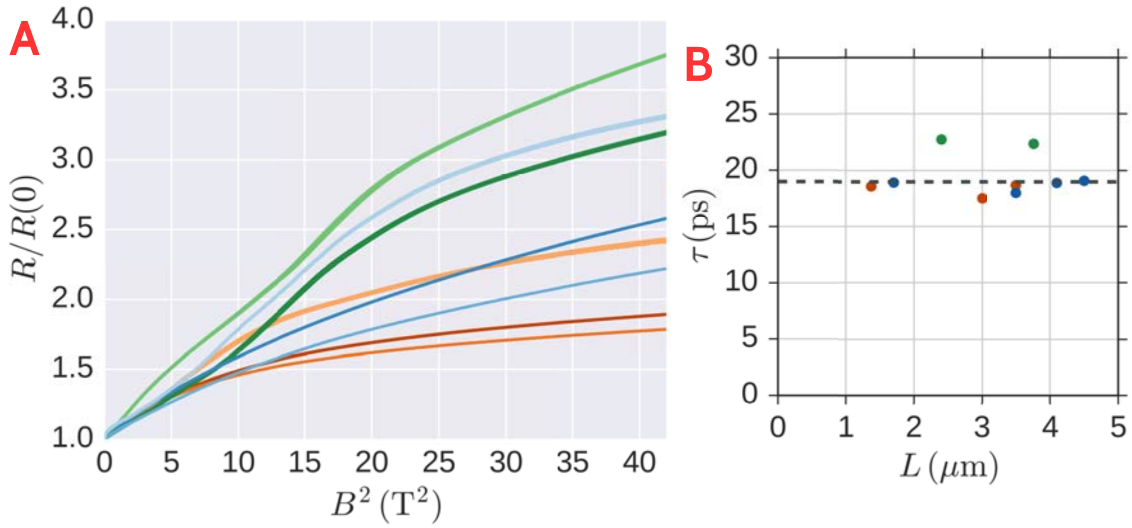

Figure 2.7: Magnetoresistance of the different sections measured in Bi_{32} (orange), Bi_{33} (green) and Bi_{34} (blue). **A** : Normalized resistances as a function of B^2. **B** : Extracted transport time as a function of the junctions lengths.

the surfaces, $G_\mathrm{N} = G_\mathrm{s} + G_\mathrm{b} \sim G_\mathrm{s}$. The mean free path on the surfaces is then deduced from the $300\,\Omega$ resistance of a 1 micron by 200 nm surface, via $\sigma S = G_\mathrm{Q} k_\mathrm{F} l_\mathrm{s} = GL/W = 1.7\,10^{-2}\,\Omega^{-1}$, from which we deduce a surface-state mean free path $l_\mathrm{s} \simeq 300\,\mathrm{nm}$, and transport time $\tau_\mathrm{s} \simeq 3\,\mathrm{ps}$.

Since the surface conductivity is greater than the bulk conductivity, equation (2.21) becomes

$$\begin{aligned}\frac{\delta\rho(B)}{\rho} &= e^2 B^2 \left(\frac{\tau_\mathrm{b}}{m_\mathrm{b}} - \frac{\tau_\mathrm{s}}{m_\mathrm{s}}\right)^2 \frac{\tau_\mathrm{b}}{\tau_\mathrm{s}} \frac{N_\mathrm{b}}{N_\mathrm{s}} \frac{m_\mathrm{s}}{m_\mathrm{b}} \\ &\sim e^2 B^2 \frac{\tau_\mathrm{b}^2}{m_\mathrm{b}^2}\end{aligned} \tag{2.22}$$

where $m_\mathrm{b} \simeq 0.065$, $m_\mathrm{s} \simeq 0.2$, $N_\mathrm{s}/N_\mathrm{b} = 100$.

The low field magnetoresistance has been measured for similar nanowires having the (111) top surface crystalline orientation (nanowires Bi_{32}, Bi_{33}, Bi_{34}) (fig 2.7). The data are plotted against B^2 and show a linear regime for B in the range $0 - 3\,\mathrm{T}$. The magnetoresistivity coefficient is nearly sample independent and yields

$$\frac{\Delta R(B)}{R(0)} \simeq \left((2\,\mathrm{ps})\frac{eB}{m_e}\right)^2 \tag{2.23}$$

This means that $\tau_\mathrm{b} \simeq 2\,\mathrm{ps}$ or equivalently $l_\mathrm{b} \simeq 200\,\mathrm{nm}$, in agreement with the value determined with the measurement of the resistance vs length.

Thus the mobility of the bulk states is two times larger than the mobility of the surface states.

4.2 Shubnikov de Haas oscillations

When the magnetic field is strong enough, the cyclotron radius will decrease : $r_\mathrm{C} = v_F/\omega_\mathrm{C}$ where $\omega_C = eB/m$ is the cyclotron frequency. For a bare electron with $v_\mathrm{F} = 10^6\,\mathrm{ms}^{-1}$, one has $r_\mathrm{C} \simeq 75\mathrm{nm}/B[\mathrm{T}]$. Standing waves will exist at the condition that $k_\mathrm{F} r_\mathrm{C} = 2\pi n$, therefore, one expects a quantization of the energy $E_n = n\hbar\omega_\mathrm{C}$. However, a quantum mechanical calculation for a massive band gives

$$E_n = (n+\gamma)\hbar\omega_\mathrm{C} \tag{2.24}$$

where γ is a shift, which depends on the band structure (Fuchs, Piechon, Goerbig & Montambaux, 2010). These resonances are called the Landau levels. For an uncoupled quadratic band $\epsilon = \hbar^2 k^2/2m$ one has $\gamma = 1/2$. For two strongly coupled bands which is the case of of the electron band at the T point of Bi then one has $\gamma = 0$. In general, this extra shift is related to the Berry phase Γ

$$\gamma = \frac{1}{2} - \frac{\Gamma}{2\pi} \tag{2.25}$$

The consequence of the formation of Landau levels in electronic transport is a higher concentration of the density of states around these levels (Goerbig, 2009). As one increases the magnetic field, the energy of the Landau levels will increase, and one of them will eventually cross the Fermi level, which remains fixed. As a result, the resistance oscillates as a function of $\epsilon_F/\hbar\omega_\mathrm{C}$. These oscillations are called the Shubnikov de Haas oscillations.

The orbits are less well defined by the presence of disorder, and therefore there is a lifetime τ_q associated to the Landau levels. This time is in principle different (shorter) than the transport time defined above. Thus, disorder will smooth the density of states as well as the oscillations.

The change of longitudinal and transverse resistivity with respect to the classical magnetoresistance is given by (Coleridge, Stoner & Fletcher, 1989)

$$\frac{1}{2}\frac{\Delta\rho_\mathrm{xx}}{\rho_0} = -\omega_\mathrm{C}\tau_\mathrm{q}\frac{\Delta\rho_\mathrm{xy}}{\rho_0} = \sum_{s=1}^{\infty} D\left(\frac{2\pi^2 s k_\mathrm{B} T}{\hbar\omega_\mathrm{C}}\right)\exp\left(-\frac{\pi s}{\omega_\mathrm{C}\tau_\mathrm{q}}\right)\cos\left(\frac{2\pi s\epsilon_\mathrm{F}}{\hbar\omega_\mathrm{C}} - s\pi + 2\pi\gamma\right) \tag{2.26}$$

where τ_q is the quantum time modelizing the damping of plane waves in momentum space, $D(x) \equiv x/\sinh(x)$ is the Dingle function. The index s denotes anharmonicity of the oscillations that can exist in case of ballistic transport. It is discarded in the following.

The resistance of the sample Bi$_4$ (section 2) was measured in four wires as a function of the perpendicular magnetic field, for different temperatures (fig 2.8A). Clear oscillations as a function of $1/B$ can be observed in the range of B between 0.6 T and 3 T, with a period $1/B_\mathrm{p}$ of $0.34\,\mathrm{T}^{-1}$. One can relate B_p to k_F through

$$\frac{\phi_0}{B_\mathrm{p}} k_\mathrm{F}^2 = 2\pi \tag{2.27}$$

Therefore, $\lambda_\mathrm{F} = 2\pi/k_\mathrm{F} = 65\,\mathrm{nm}$. The oscillation pattern was then high pass filtered to isolate the contribution of this mode (fig 2.8D). The remaining low frequency part also displayed some oscillations features with period $1/B_\mathrm{p} = 0.16\,\mathrm{T}^{-1}$ however with only two clearly visible periods. The corresponding Fermi wavelength is $\lambda_\mathrm{F} = 45\,\mathrm{nm}$.

It is interesting to observe that the Shubnikov de Haas oscillation for this bulk mode has a phase shift of 1/2 in the oscillations (fig 2.8A,B). This corresponds to a Berry phase of π, and thus shows that the mode $\lambda = 45\,\mathrm{nm}$ has a Dirac-like dispersion relation.

At low temperature, the Dingle factor is equal to 1, and the exponential decay of the oscillations $\exp(-B/B_\mathrm{d}) = \exp(-\pi/\omega_\mathrm{C}\tau_\mathrm{q})$ provides the information on the mobility of these carriers, or alternatively on the mean free path $l_\mathrm{e} = v_\mathrm{F}\tau_\mathrm{q}$. One has :

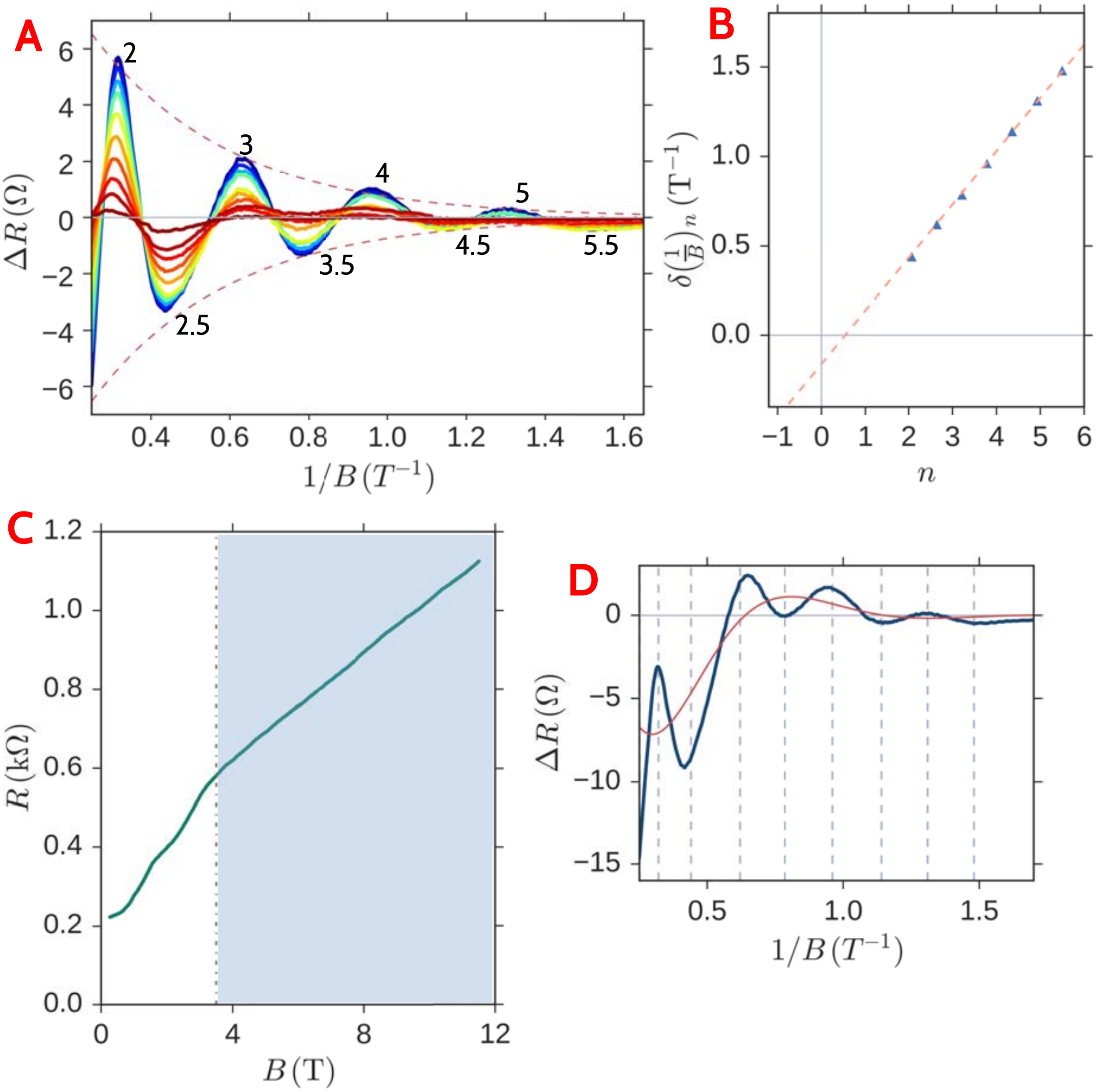

Figure 2.8: Shubnikov de Haas oscillations of the four wire magnetoresistance for Bi-Pd sample (section 2). A: Resistance subtracted from the resistance at the highest temperature for different temperatures ranging from 5 K to 80 K. The data was filtered to select the higher frequency contribution as explained in the text. Dashed line : exponential envelope functions $\pm 13.6\exp(-2.5/B)$. B : Phase of the oscillations as a function of their index, displaying a linear behaviour. Triangle : extracted phase, fine dotted line : extrapolation. The extrapolated curve crosses 0 at $n = 0$ indicating a Berry phase of π. C : Magnetoresistance. The shaded area corresponds to the extreme quantum limit. D : Low frequency (pink) - high frequency (blue) separation. The half periodicity of the oscillations were shown.

$$l_{\mathrm{e}} = \frac{\phi_0 k_{\mathrm{F}}}{B_{\mathrm{d}}} \tag{2.28}$$

The mode $\lambda_{\mathrm{F}} = 65\,\mathrm{nm}$ has a slower decay giving rise to $l_e \simeq 200\,\mathrm{nm}$, whereas the mode $\lambda_{\mathrm{F}} = 45\,\mathrm{nm}$ has $l_e \simeq 140\,\mathrm{nm}$. These values are consistent with diffusion limited by the diameter of the nanowire.

One can define a quality factor for Shubnikov de Haas oscillations which counts the number of $1/B$ periodic oscillations that can be observed before being damped

$$Q_{\mathrm{SdH}} \equiv \frac{B_{\mathrm{p}}}{B_{\mathrm{d}}} = \frac{k_{\mathrm{F}} l_{\mathrm{e}}}{2\pi} \tag{2.29}$$

which is a central quantity in mesoscopic physics. The limitation of the mean free path by the diameter $l_{\mathrm{e}} \lesssim d$ implies that as the size of the nanowire is reduced, bulk modes become more and more diffusive. The signature of this behaviour is the disappearance of Shubnikov de Haas oscillations for large λ_{F}, as it would lead to a small Q_{SdH} and thus a strong damping of the oscillations. Therefore, a consequence of finite size effects for narrow nanowires is the bad conductivity of bulk modes that can be directly observed through the damping of Shubnikov de Haas oscillations.

However, finite size effects could manifest themselves in a more drastic way : the quantization of small wavevectors should directly filter out bulk modes. We provide arguments along this line in the following section.

4.3 Linear magnetoresistance

We observed a linear magnetoresistance from $B = 0$ for a part of a nanowire with (111) oriented top surface that was cleaved, contrarily to the magnetoresistance measured for the non cleaved part of the same nanowire. The latter showed a quadratic instead of a linear behaviour, similarly to the magnetoresistance measured in all other samples studied during this thesis. Linear magnetoresistances were already observed about 100 years ago (Kapitza, 1929), and have been mainly explained by two theories : by the motion of a single Landau Level in the so called extreme quantum limit (Abrikosov, 1969) or by a diffusion driven mechanism in homogeneously disordered 2D gas (Parish & Littlewood, 2003). A great number of recent studies in various systems displayed linear magnetoresistances (Veldhorst et al., 2013), but the responsible mechanism is still debated. Recently, the Abrikosov theory was revisited to explain this phenomenon in 3D materials by the diffusive motion of guiding centers leading to a mixing of the resistivity tensor components (Song, Refael & Lee, 2015). I will now detail our measurement.

We found a naturally cleaved Bi nanowire of diameter $\varnothing \simeq 100\,\mathrm{nm}$ (fig 2.9B). The EBSD characterization indicated a (111) top surface orientation. We connected it with FIB-W electrodes after etching 100 nm thick Au electrodes that were deposited by e-beam evaporation beforehand and that did not make a good electrical contact to the nanowire. However, no induced superconductivity was found in both samples.

The connected lengths of the cleaved part (Cl) were $L = 2.3\,\mu\mathrm{m}$ and $L = 3.7\,\mu\mathrm{m}$ for the non cleaved part (Ncl). The resistance measured at $120\,\mathrm{mK}$ were $224\,\Omega$ for (Cl) and $248\,\Omega$ for (Ncl).

The magnetoresistance was measured at $130\,\mathrm{mK}$ with a lockin amplifier at $1\,\mu\mathrm{A}$ bias, and leads to very different results (fig 2.9A). For the non-cleaved sample, the magnetoresistance follows the usual quadratic law at low fields followed by an almost linear Kapitza

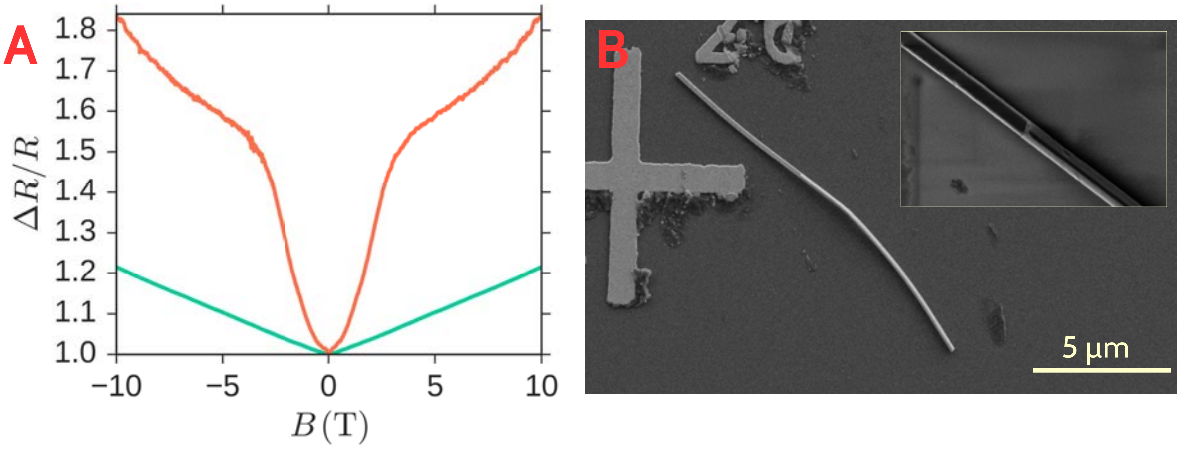

Figure 2.9: Linear magnetoresistance. A : Magnetoresistances measured at 4.2 K. The green curve corresponds to the non cleaved sample, the blue curve corresponds to the cleaved sample. B: SEM image of the long nanowire showing a cleaved part and a non cleaved part. Inset : zoom of the cleaved-non cleaved junction using a different electron detector

law at $|B| > 4\,\mathrm{T}$. On the contrary, the cleaved sample displayed a linear magnetoresistance from $B = 0$.

For very strong magnetic fields such that $\hbar\omega_\mathrm{c} \gg \epsilon_\mathrm{F}$, one enters the extreme quantum limit for bulk states. This regime is characterized by a linear magnetoresistance.

The hamiltonian for Landau levels in 3D for an isotropic model is

$$H = \hbar\omega_\mathrm{c}\left(n + \frac{1}{2}\right) \mp g\hbar\omega_\mathrm{c} + \frac{\hbar^2 k_\mathrm{z}^2}{2m} \tag{2.30}$$

where the magnetic field is applied along the z direction and the minus (resp plus) sign designates the up (resp down) spin. Importantly, the motion of electrons along z is free.

For a very strong magnetic field, only the $n = 0$ Landau level (LL) will be populated. The number N_e of electrons in this state, which is the total number of electrons in the system, is related to k_z through

$$N_e = \frac{k_\mathrm{z} t}{2\pi^2}\frac{BS}{\phi_0} \tag{2.31}$$

which has to be understood as the product of the number of transverse modes $k_\mathrm{z} t$ where t is the transverse size, times the LL degeneracy BS/ϕ_0. It is valid only in the continuous limit, and one can equivalently compute the electron density $n_\mathrm{e} = k_\mathrm{z} B/2\pi^2\phi_0$.

In this extreme quantum limit, the scattering with an impurity is non perturbative, and one has to sum an infinity of impurity diagrams. A simplification arises in the limit of sufficiently diluted impurities with concentration $n_\mathrm{i} \ll n_\mathrm{e}$ and one can solve the problem with a single self-energy diagram. As a result, the elastic scattering time is

$$\begin{aligned}\tau &= \frac{eBm}{n_\mathrm{i}\hbar k_z}\\ &= \frac{(B/\phi_0)^2}{(2\pi^2)^3}\frac{m}{n_\mathrm{e} n_i}\end{aligned} \tag{2.32}$$

in particular it does not depend on the detail of the scattering potential.

The conductivity tensor will be given by

$$\begin{aligned} \sigma_{\mathrm{xx}} &= \sigma_{\mathrm{yy}} = e n_{\mathrm{i}}/B \\ \sigma_{\mathrm{xy}} &= n_{\mathrm{e}} e/B \end{aligned} \tag{2.33}$$

where the Hall component σ_{xy} is unchanged in this limit. The resistivity components are

$$\begin{aligned} \rho_{\mathrm{xx}} &= \rho_{\mathrm{yy}} = \frac{n_{\mathrm{i}} B}{n_0^2 e} \\ \rho_{\mathrm{xy}} &= \frac{B}{n_0 e} \end{aligned} \tag{2.34}$$

The finite size effect manifest themselves in the fact that the $k_{\mathrm{z}} t$ product can only take integer values. In particular, the validity criterion is dramatically changed in this limit. As a result, if the bulk can only host a single LL at most, one expects the validity criterion to be true for all magnetic fields.

However, in order for this theory to explain our data, one has to add the conductivity of surface states in addition to bulk states to account for the total conductivity of the sample. The resistance $R_0 = 200\,\Omega$ at zero magnetic field cannot be explained only by bulk modes, especially if they are confined in one dimension.

In conclusion, we have found a very different magnetoresistance in a cleaved and a non cleaved sample coming from the same nanowire. This may come from a difference in quantization of Bulk modes due to the different thicknesses. However one should take surface conduction into account as well in order to describe the data quantitatively. An other explanation comes from the diffusion of guiding centers in a smooth disorder potential.

5 Proximity effect in Bi nanowires connected with W electrodes

A supercurrent can be induced in a nanowire connected to superconducting electrodes at low temperatures, on the condition that it is phase coherent, that it to say that its length verifies $L < L_{\mathrm{T}}$, L_{φ}. This supercurrent is carried by Andreev bound states (ABS) which are inherently sensitive to an external magnetic field. For an usual SNS junction with many channels, the orbital effect dominates leading to scrambling interferences between the numerous ABS that are free to explore the available space in the nanowire. Measuring the magnetic field dependence of the supercurrent can thus provide information on the trajectories of ABS. For this purpose, it is desirable to use a superconducting material with a high critical field, in order to be able to neglect the influence of the magnetic field dependence on the contacts.

5.1 Superconducting electrodes with high critical field

Contrarily to crystalline tungsten which has a a critical temperature $T_{\mathrm{C}} \simeq 15\,\mathrm{mK}$ and a critical field $H_{\mathrm{C}} \simeq 2\,\mathrm{G}$ (Black, 1968), the tungsten deposited by FIB has a much higher critical temperature ($T_{\mathrm{C}} \simeq 4 - 7\,\mathrm{K}$) and has a very strong critical field $H_{\mathrm{C}}^2 \gtrsim 12\,\mathrm{T}$. The reason for this is that FIB deposited W results from the decomposition of the precursor gaz

Table 2.2: Transport properties of Bi nanowires showing proximity effect.

Sample	w (nm)	L (μA)	$R_C + R_N$ (Ω)	I_C (μA)	$R_N I_C$ (mV)	$\pi\epsilon_T^b$ (mV)	$10.8\epsilon_T^d$ (mV)
Bi_1	90	1.9	900 *	1.7	1.53 *	0.66	0.032
Bi_2	90	2	$1.0\,10^4$ *	0.14	1.40 *	0.62	0.032
Bi_3	90	1.6	$1.5\,10^4$ *	0.07	1.05 *	0.79	0.054
Bi_8	200	1.4	$1.2\,10^3$ *	1.0	1.20 *	0.88	0.141
Bi_{32} (JU)	200	1.4	$0 + 330$	1.4	0.46	0.88	0.141
Bi_{33} (WH)	250	2.4	$30 + 116$	0.19	0.23	0.50	0.065
Bi_{34} (SD)	230	1.7	$180 + 77$	5.4	0.42	0.72	0.11

$W(CO)_6$ using Ga^+ ions. This decomposition is imperfect, leading to an alloy containing C (10 %) as well as Ga (10 %), O (5 %), leaving only 75 % of W, and therefore has an enhanced T_C but more importantly a greatly enhanced H_C^2. The latter property allows us to study Josephson junctions up to very high magnetic fields.

5.2 Proximity effect in zero magnetic field

We have connected two types of wires with FIB deposited W electrodes.

We conducted a first study on Bi nanowires grown by electrodeposition through polymer template, of diameter 90 ± 10 nm but with unknown crystal orientation (C. Li et al., 2014). They were wet deposited on a Si/SiO_2 substrate and connected using FIB-assisted deposition of W electrodes. Out of 10 samples, 5 nanowires did not show any sign of induced superconductivity, 2 samples showed a decrease of the resistance below the T_C of W, and 3 samples displayed a zero differential resistance at low temperatures ($T = 100$ mK), characteristic of a complete superconducting proximity effect (Bi_1, Bi_2, Bi_3).

In a second generation of measurements, crystalline nanowires of larger diameter $\varnothing \simeq 100 - 250$ nm grown by sputtering on a hot surface technique and connected with W electrodes were measured. Their crystal orientation was determined by EBSD. We selected only nanowires having their (111) orientation parallel to the substrate. Out of 16 junctions fabricated, only 4 showed a full superconducting proximity effect (Bi_8, Bi_{32}, Bi_{33}, Bi_{34}).

The fact that we observed no supercurrent in many junctions can be explained by two factors : either they were too long compared to L_T, L_φ or they were badly connected. The transport properties of the other junctions are summarized in the table 2.

The resistances marked with a $*$ likely include a large contact resistance which is unknown. The remaining three junction (Bi_{32}, Bi_{33}, Bi_{34}) were respectively part of nanowires where the resistance of other sections of different length could be determined. We could therefore extract the contact resistance from the length dependence of these resistances.

The amplitudes of the critical current ranges from $0.07\,\mu$A to $5.4\,\mu$A. In order to estimate how much supercurrent is carried per channel, one can compute the $R_N I_C$ product, which measures the average Josephson energy per channel. Note that for the junctions marked by a star, this product is less meaningful because of the large contact resistance. For the other junctions (Bi_{32}, Bi_{33}, Bi_{34}) it is nevertheless larger than the expected value $10.8\epsilon_T^d = 3.6\hbar v_F l_e / L^2$ for a long diffusive junction. Here, I took $l_e = w$, as justified by the study in the normal state, and $v_F = 6 \cdot 10^5$ m/s. These large values of the $R_N I_C$ product therefore imply that the junction has ballistic channels. It could be either a short junction or a long junction.

In the case of a short junction, one has $R_\mathrm{N} I_\mathrm{C} = \pi\Delta = 3.77\,\mathrm{meV}$, taking a $T_\mathrm{C} = 6\,\mathrm{K}$ for W. This value is larger than the $R_\mathrm{N} I_\mathrm{C}$ measured experimentally. If the junction are between the short and the long limit, that is to say $L \simeq \xi$, then we find from simulations that $R_\mathrm{N} I_\mathrm{C} = 2\Delta$ for $L = \xi$, and $R_\mathrm{N} I_\mathrm{C} = \Delta$ for $L = 2\xi$. Such an intermediate length can be justified given the uncertainty on the T_C of FIB deposited W as well as v_F, giving $\xi = \hbar v_\mathrm{F}/\Delta = 190 - 650\,\mathrm{nm}$. Additionnally, one could argue that the superconducting FIB W contamination effectively reduces L by $0.4\,\mu$m. Nevertheless, this interpretation in terms of junction of intermediate length is only possible for Bi$_{32}$, but is less realistic for the other junctions.

The second possibility is that the junctions are long and contains a significant amount of ballistic channels in addition to diffusive channels that contribute less to the supercurrent. Indeed, for a long ballistic junction, one has $R_\mathrm{N} I_\mathrm{C} = \pi\epsilon_\mathrm{T}^\mathrm{b} = \pi\hbar v_\mathrm{F}/L \sim 1/L$. Besides, $R_\mathrm{N} = \frac{R_\mathrm{Q}}{M}\frac{L}{l_\mathrm{e}} \sim L/l_e$ for a diffusive channel, whereas $R_\mathrm{N} = \frac{R_\mathrm{Q}}{M} \sim 1$ for a ballistic channel. As a result, the critical current of a diffusive channel is reduced by a factor $(L/l_\mathrm{e})^2$ compared to a ballistic channel, that is about 25 for a junction with $L = 1\,\mu$m and $l_e = 200\,\mathrm{nm}$. Thus, the large value of I_C can be interpreted by the existence of ballistic channels that contribute majoritarily to the supercurrent in addition to diffusive channels that contribute less. This will be confirmed by the measurement of the current-phase relation as exposed in the next chapter. On the other hand, the total resistance is less sensitive to the ballistic contribution.

One can further estimate the number M_b and $M_\mathrm{d} = M - M_\mathrm{b}$ of effective ballistic and diffusive channels respectively. First, the total conductance is given by the sum of the conductance of both components

$$G = G_\mathrm{Q}\left(M_\mathrm{b} + M_\mathrm{d}\frac{l_\mathrm{e}}{L}\right) \tag{2.35}$$

Second, the supercurrent is the sum of the contribution of both components

$$\begin{aligned} I_\mathrm{C} &= M_\mathrm{b}\left(\frac{ev_\mathrm{F}}{L}\right) + M_\mathrm{d}\left(\frac{1}{2}\frac{ev_\mathrm{F}}{L}\left(\frac{l_\mathrm{e}}{L}\right)^2\right) \\ &\simeq M_\mathrm{b}\left(\frac{ev_\mathrm{F}}{L}\right) \end{aligned} \tag{2.36}$$

where the 1/2 factor comes from the 2D diffusive states that dominates transport, and I neglected the second term as justified above. The calculation without approximation yields $(M, M_\mathrm{b}) = (137, 19)$ for Bi$_{32}$, $(1304, 2)$ for Bi$_{33}$ and $(638, 90)$ for Bi$_{34}$.

A better insight into the distribution of supercurrent over the different channels is provided by additional experiments : the field dependence of the proximity effect described below, and the current-phase relation described in the next chapter.

5.3 Resilience of critical current at high magnetic field

I recall the generic field dependence of I_C of ordinary SNS junctions with many conduction channels. The magnetic field suppresses I_C via two different pair breaking mechanisms. In the semi-classical limit (λ_F much smaller than all sample dimensions), the orbital phase breaking is due to the Aharonov Bohm phase difference between different Andreev pairs that follow different trajectories through the normal metal. This orbital dephasing suppresses the supercurrent at fields corresponding to one flux quantum

$\phi_0 = h/2e$ through the sample, as observed experimentally e.g. in Au wires (Chiodi, 2010), as well in Ag nanowires (see previous chapter). In our wires with dimensions $L \times w = 200\,\mathrm{nm} \times 1\,\mu\mathrm{m} \simeq 2 \cdot 10^{-13}\,\mathrm{m}^2$ this would correspond to a typical magnetic field $B = \phi_0/S \simeq 100\,\mathrm{G}$.

For all the Bi-based Josephson junctions, the supercurrent was found to exist up to the maximal field of the coil, either $7\,\mathrm{T}$ or $11\,\mathrm{T}$, even for the longer junction of length $L = 2.4\,\mu\mathrm{m}$ (fig 2.10).

We interpret this very striking behaviour by the possibility that the supercurrent is carried by few very narrow channels, thereby suppressing the orbital effect. The length of the junctions were typically $L = 1\,\mu\mathrm{m}$ and the typical scale of the magnetic field suppression of the critical current of $B_\mathrm{d} \simeq 10\,\mathrm{T}$. Therefore we can estimate the supercurrent carrying channel's maximal width, over which the orbital effect should destroy the supercurrent to be

$$w_\mathrm{c} \lesssim \frac{1}{L}\frac{\phi_0}{B_\mathrm{d}} \simeq 0.2\,\mathrm{nm} \tag{2.37}$$

This means that the confinement of the channels in Bi occurs within a few atomic lengths. This result is in line with the prediction that edge states are very localized in Bi (111) (Wada et al., 2011).

To put this result into perspective, one can compare the magnetic field dependence of Bi nanowire based JJ to the magnetic field dependence found in a conventional SNS junction made of an Ag nanowire also connected with W electrodes, of length $L = 2.2\,\mu\mathrm{m}$, of diameter $\varnothing = 50\,\mathrm{nm}$ (fig 2.11). The number of channels for this system is $M \simeq 10^5$, the geometry is such that $w \ll L$, and it was shown to be diffusive. Accordingly, one can fit the decay of the critical current by an orbital dephasing law (Montambaux, 2007)

$$I_\mathrm{C}(B) = I_0 \frac{\sigma \frac{\phi}{\phi_0}}{\sinh\left(\sigma \frac{\phi}{\phi_0}\right)} \tag{2.38}$$

where $\sigma = \frac{\pi}{\sqrt{3}} = 1.81$. We find an excellent agreement with this law, although we have to adjust $\sigma = 4.11$. This would lead to a rescaling of the flux by 2.27, similarly to what was found in diffusive Au based SNS junctions (Chiodi et al., 2012).

In the case of Bi, there is a much slower decay of the supercurrent at high magnetic field. One can give a rough explanation of the asymptotics by assuming that the current is carried along one ballistic edge state, with a distribution that is exponentially localized at the edge of the nanowire and is dephased upon the application of $\mathbf{A}$. Diffusive states are not represented in this picture, as their contribution to the supercurrent is weaker by a factor $(L/l_\mathrm{e})^2 \simeq 10^2$. I take the nanowire along x, with transverse coordinate y and work in the gauge $\mathbf{A} = By\mathbf{e}_\mathrm{x}$. I first suppose that the density of states is of the form $\rho(y) \propto \mathrm{e}^{-2\pi y/\lambda}$, $\lambda \ll w$, where λ is the transverse localization length and w is the width of the nanowire. Then the effect of orbital dephasing is to average on all the paths $p \in P$:

$$\begin{aligned} I_\mathrm{C}(B) &= I_0 \left| \left\langle \mathrm{e}^{2i\pi \frac{\phi(p)}{\phi_0}} \right\rangle_P \right| \\ &= I_0 \left| \int_0^w \mathrm{d}y \mathrm{e}^{\frac{2i\pi ByL}{\phi_0}} \left(b\mathrm{e}^{-2\pi y/\lambda}\right) \right| \\ &= I_0 \left| \frac{1}{1+ix} \right| = I_0 \frac{1}{\sqrt{1+x^2}} \end{aligned} \tag{2.39}$$

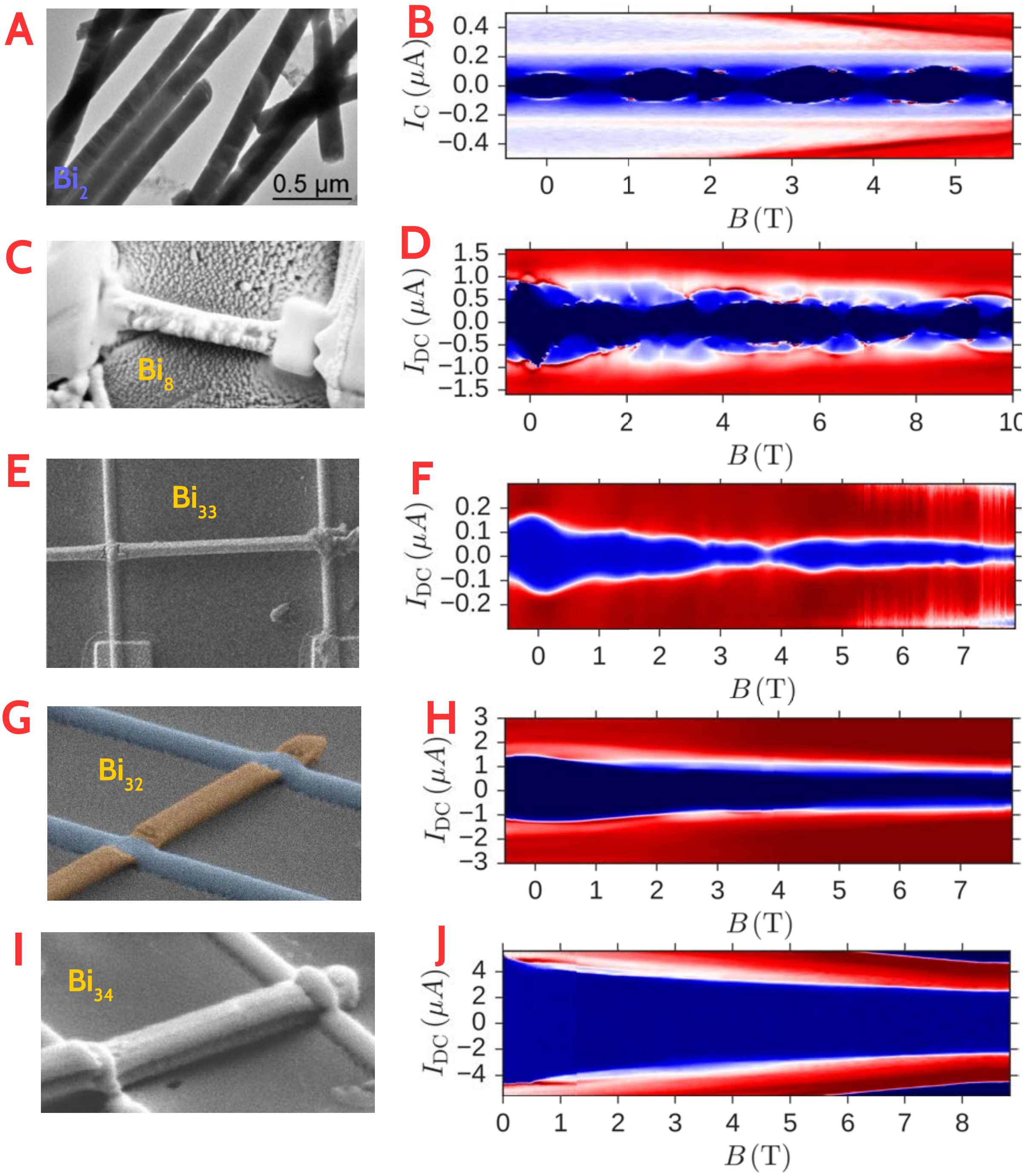

Figure 2.10: Differential resistance showing the supercurrent induced in Bismuth nanowires as a function of the bias current and magnetic field at large magnetic field. The critical current is seen to persist to high field, and oscillates with a typical scale of 1 T. Left : SEM images of the devices, right : measurement. **A-B** Measurement on the junction Bi_2 with unknown orientation. **C-J** SEM image and Ic vs B for nanowires with (111) top surface. Note that the FIB may have contaminated Bi_8 (C-D) on some parts resulting in a smooth transition to the normal state as a function of I_{DC}. Note also that Bi_{34} (I-J) consists in two aggregated nanowires in parallel, which can explain the resulting large value $I_C = 5.4\,\mu$A at zero field.

where $I_0 = I(B = 0)$, and the reduced flux x is defined by $x \equiv BL\lambda/\phi_0 = 2\pi\phi/\phi_0$. This law fails to reproduce at the same time the data at low magnetic fields $B \lesssim 1\,\mathrm{T}$ and the resilience of the supercurrent at $B \simeq 7\mathrm{T}$. A better fit is obtain by assuming the existence of a second lengthscale of the order of the atomic size of Bi.

For this purpose, lets assume now that the distribution is in fact characterized by two localization lengths λ_1 and λ_2. The length λ_2 represents the ultimate confinement of an edge state, that is few Å. The length λ_1 represents less confined edge states, that are for example hybridized with the bulk or surface states. A similar calculation gives the following law

$$I_{\mathrm{C}}(B) = I_0 \left| \frac{1-\alpha}{1 + iB/B_{\mathrm{d}}^1} + \frac{\alpha}{1 + iB/B_{\mathrm{d}}^2} \right| \tag{2.40}$$

where $B_{\mathrm{d}}^{1,2} = \phi_0/\lambda_{1,2}L$ are the magnetic field decay scales associated to the two localization lengths considered, and α is a dimensionless weighting parameter.

It turns out that this model agrees well with the average behaviour of the critical current data taken on characterized nanowires with (111) top surface, if we take $\lambda_2 = 1.8\,\text{Å}$ and $\alpha = 1/3$ for all the wires (fig 2.11A,C,E) except Bi_{34} where one has to take $\alpha = 2/3$ (fig 2.11F). The length λ_1 is about 0.6 times the nearest neighbor distance in Bi (Liu & Allen, 1995). The justification for the 1/3 weighting factor is the following : as one increases the magnetic field, the orbital structure p_{x}, p_{y}, p_{z} of the edge states will hybridize, resulting in the gaping of some of the energy level crossings. Due to the topological protection, it is predicted that one Kramers pair of edge states remains (Wada et al., 2011). This argument should apply as long as the magnetic length is larger than the localization length of the remaining edge state, that is to say $B \lesssim 10\,\mathrm{T}$. The fact that the junction SD needs a different treatment with $\alpha = 2/3$ is not fully understood, but could be the result of its geometry made of two stuck nanowires (fig 2.10 I).

The only adjusted parameter in (2.40) is the decay length λ_1, shown in table 2.3. From the discussion above, this length measures the hybridization of non topological ballistic states, which could occur e.g. upon scattering with impurities. Interestingly, the junctions Bi_8 and Bi_{32} have very similar characteristics, with supercurrents $I_0 \simeq 1\,\mu\mathrm{A}$ and length $L = 1.4\,\mu\mathrm{A}$, however their decay length λ_1 differs by one order of magnitude : $\lambda_1 \simeq 1\,\mathrm{nm}$ for Bi_8 and $\lambda_1 \simeq 10\,\mathrm{nm}$ for Bi_8. Given that Bi_8 is very disordered at the surface (fig 2.10 I), one can understand qualitatively the origin of this difference as the result of scattering at the surface with FIB induced contamination.

The fluctuations of the critical current around this average behaviour also have some structure that can be related to the Zeeman effect as will be showed now.

5.4 Oscillations due to Zeeman effect

In samples with a very small area perpendicular to the magnetic field, the orbital dephasing is weak, and the Zeeman effect becomes noticeable, especially for high g factor materials. The Zeeman effect causes an energy difference $\epsilon_{\mathrm{Z}} = g\mu_{\mathrm{B}}B$, and therefore a phase difference between the electron and hole components of a given Andreev pair, given by $\theta_{\mathrm{B}} \equiv \epsilon_{\mathrm{Z}}\tau/\hbar = \epsilon_{\mathrm{Z}}/\epsilon_{\mathrm{T}}$.

As illustrated by the theory of Nazarov et. al. in the short junction limit (Yokoyama, Eto & Nazarov, 2014) for $M = 4$ channels this leads to oscillations of the critical current, with a typical period given by $\theta_{\mathrm{B}} \sim n\pi$, i.e. $\Delta B = \epsilon_{\mathrm{T}}/g\mu_{\mathrm{B}}$ (fig 2.11 D). An other feature was predicted by these authors : an asymmetry between the positive and negative critical

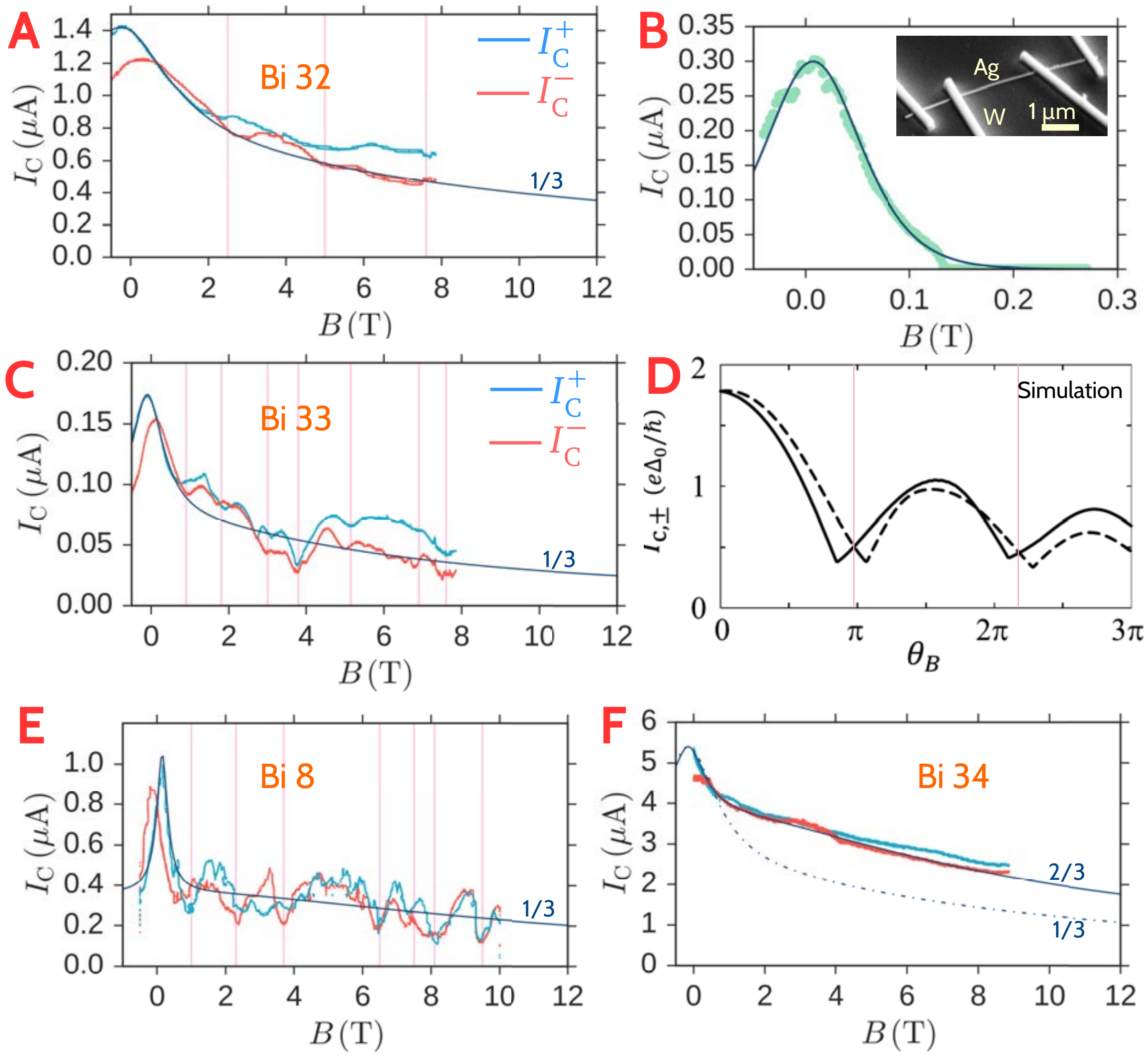

Figure 2.11: Magnetic field dependence of the critical current of Bi nanowires with top (111) surface for large perpendicular magnetic fields. **A, C, E, F** : Critical current vs magnetic field, (I_+, red) and (I_-, blue) differential resistance vs bias current, critical current vs magnetic field for the junctions Bi$_{32}$, Bi$_{33}$, Bi$_8$, Bi$_{34}$ respectively. **B** : I_C vs B for an Ag nanowire with dimensions $L \times w = 2.2\,\mu\mathrm{m} \times 50\,\mathrm{nm}$. The fit was done using formula 2.38. **D** : Dependence of the critical current with the Zeeman field $\theta_B \equiv \epsilon_Z/\epsilon_T$ in a short junction with $M = 4$ channels and with spin-orbit interaction, predicted by (Eto, Yokoyama et al, 2015). Solid line : positive current I_+, dashed line negative current I_-.

Table 2.3: Structure of the critical current at large magnetic fields

Sample	B_{d}^1 (T)	λ_1 (nm)	B_{d}^2 (T)	λ_2 (nm)	δI (nA)	δM_{b}	ΔB (T)	g
Bi_2					75	1.5	1.25	8.6
Bi_8	0.15	9.6	8.0	0.18	280	4.0	1.3	11.7
Bi_{32} (JU)	1.3	1.1	8.0	0.18	60	0.86	3.1	4.9
Bi_{33} (WH)	0.41	2.0	4.7	0.18	50	1.23	1.0	7.8
Bi_{34} (SD)	0.50	2.3	6.5	0.18				

Table 2.4: SQUID-like oscillations parameters

Sample	ΔB (G)	w_{eff} (nm)	δI (nA)	B_{d} (T)	$B_{\max}$ T
Bi_1	754	12	100	1.2 *	4.5
Bi_3	154	70	5	0.43	2.5
Bi_{32} (JU)	100	140	10	0.18	1

current in presence of SOC. This oscillatory behaviour is seen in all samples, with typical period between 1 and 3 T (fig. 2.11 A,B and 2.10). We also observe the asymmetry as indicated by the red and blue curves I_{C}^{+}, I_{C}^{-} (fig. 2.11 A, B). Furthermore, the amplitude δI of the oscillations can also be interpreted in terms of a number of channels $\delta M_{\mathrm{b}} \sim 1$ (table 2.3), which agrees with what is found from the numerical simulations by Nazarov et. al.

From the period ΔB, one can extract the g factor using the estimated $\epsilon_{\mathrm{T}}^{\mathrm{b}}$. This yields $g \simeq 5 - 10$ for all the wires.

In summary, it is important to note that this g factor is associated to ballistic states at high field and is possibly lower than the g factor found at lower fields, where all the orbitals contribute.

5.5 SQUID-like oscillations

If few narrow channels exist at the two edges of a nanowire connected to superconducting electrodes, they should lead to a two slit interference pattern with periodic oscillations similar to a SQUID. We do indeed observe such oscillations in three samples : $\mathrm{Bi}_1, \mathrm{Bi}_3, \mathrm{Bi}_{33}$.

The period of these oscillations (100 G) should correspond to one flux quantum enclosed between the two trajectories located on the two edges of the nanowire, that is ϕ_0 across the area of the nanowire.

This is confirmed for the oscillations we find (fig 2.12,2.13,2.14), and one can further evaluate the distance w_{eff} between the supercurrent carrying paths (table 2.4). The partial modulation between $5-10\%$ of the supercurrent is typical of a SQUID with two branches, with very different critical current I_C^1 and I_C^2.

The SQUID-like oscillations persist up to $B_{\max} = 2.5\,\mathrm{T}$ for Bi_3, 4.5 T for Bi_1 and 1 T for Bi_{32}, confirming that the edge states are narrow. The decay scale B_{d} of the oscillations can be fitted by a gaussian, shown in table 2.4. The value of B for Bi_1 is marked with a * indicating that it was not fitted but only estimated.

5.6 Modulation of the SQUID-like oscillations

We have analyzed more precisely the SQUID like oscillations of sample Bi_3, which were visible up to 2.5 T. They display a clear amplitude modulation with a period $B_2 = 2200\,\mathrm{G}$

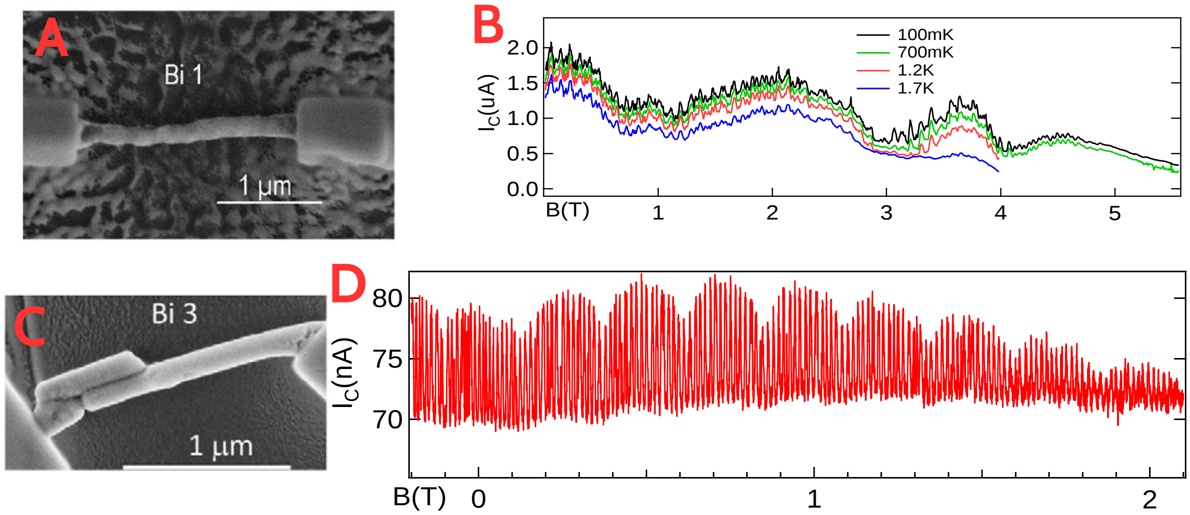

Figure 2.12: SQUID-like oscillations found in Bi samples with unknown orientations. **A** : SEM image of the sample Bi_1. **B** Magnetic field dependence of I_{C} of sample Bi_1, taken for different temperatures. **C-D** SEM image and magnetic field dependence of I_{C} of sample Bi_3. The SQUID like oscillations are of period 154 G (orbital effect) and their amplitude is modulated with a period 2200 G (Zeeman effect).

(fig 2.12).

This amplitude modulation of the SQUID like oscillations can be understood as the Zeeman effect acting on the two supercurrent carrying channels, if they have different g factors.

Moreover, in presence of spin-orbit interaction, bands are spin split, which implies a finite momentum k_{SO} between up spin and down spin. The addition of a Zeeman effect raises one band with respect to the other one. This leads to a difference between Fermi velocities v^+ and v^- related to the spin up and spin down respectively.

The full calculation including spin-orbit interactions was done by Mironov and Buzdin ((Mironov, Mel'nikov & Buzdin, 2015), yielding a current-phase relation

$$I(\varphi) = \sum_{n=1,2} I_n \sin\left(\varphi + \beta_n B + (-1)^n \pi\phi\right) \cos(\gamma_n B) \tag{2.41}$$

where $\gamma_n = g_n \mu_{\mathrm{B}} L \left(1/v^+ + 1/v^-\right)$ leads to Zeeman induced modulations of the sign and amplitude of the critical current ($0-\pi$ type transitions) and $\beta_n B = g_n \mu_B B L(1/v^+ - 1/v^-)$ results in the formation of spin-orbit and Zeeman induced ϕ_0 junction, that will be discussed in the next chapter.

The critical current is then given by

$$\begin{aligned} I_{\mathrm{C}}^2 &= I_1^2 \cos(\gamma_1 B) + I_2^2 \cos(\gamma_2 B) + I_1 I_2 \cos(\gamma_1 B)\cos(\gamma_2 B)\cos\left(\frac{2\pi\phi}{\phi_0} + (\beta_1 - \beta_2)B\right) \\ I_{\mathrm{C}} &\simeq \left|I_1 \cos\left(\gamma_1 B\right)\right| \left|1 + I_2 \frac{\cos\left(\gamma_2 B\right)}{\cos\left(\gamma_1 B\right)} \cos\left(2\pi\frac{\phi}{\phi_0} + (\beta_1 - \beta_2)B\right)\right| \end{aligned} \tag{2.42}$$

in the case $I_2 \ll I_1$. This implies an amplitude and frequency modulation of the critical current.

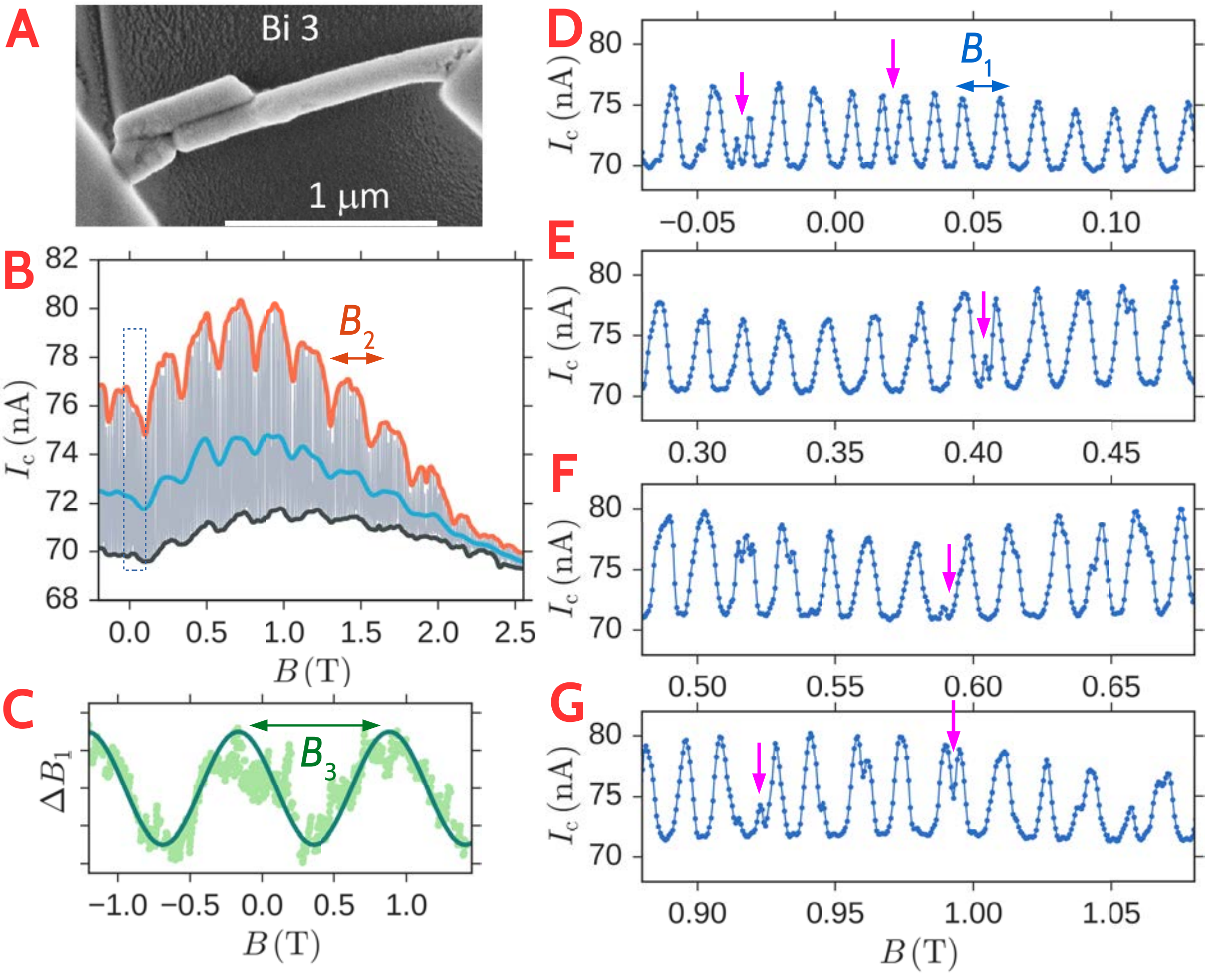

Figure 2.13: Oscillations in magnetic field for sample Bi3 connected with FIB-W. **A** : SEM image of the sample Bi_3. The nanowire was grown in a polycarbonate membrane. A smaller lateral nanowire is visible, however it should not be electrically connected to it due to the presence of the membrane in between. **B** : Oscillations of the critical current as a function of the magnetic field from 0 to 2.5 T. The red, blue and black curve are obtained by applying a moving filter to the main curve using the maximum, average and minimum functions on a 3 periods wide window. This evidences an amplitude modulation of the SQUID-like oscillations of amplitude 3 nA, and period $B_2 = 2200\,\mathrm{G}$. **C** : Variation of the period B_1 of the SQUID-like oscillations as a function of the magnetic field. **D-G** Zoom of the I_C vs B curves. They display oscillations with a local period $B_1 \simeq 154\,\mathrm{G}$. This period changes as a function of the magnetic field due to phase jumps, as indicated by pink arrows. The magnetic field dependence of B_1 is sinusoidal with period $B_3 = 1\,\mathrm{T}$, as shown in C.

A frequency modulation is also visible in the data. This can be seen in the form of phase jumps or change of the period B_1 of the SQUID-like oscillation (fig 2.13D-G). This can be quantified by computing the density of local minima in the current (fig 2.13 C) . We find an oscillation of the period ΔB_1 on the scale of 1 T.

5.7 Magnetic field orientation dependence of the SQUID-like oscillations

The finding of two-path interference patterns of the critical current is consistent with the existence of two distinct current paths located on the opposite edges of the wire. Given that these edges are in fact predicted to be located at the diagonally opposite edges of the nanowire from our tight-binding simulations, then one should also be able to observe SQUID-like oscillations in a in-plane magnetic field as well. We could measure the critical current oscillations of Bi_{32} as a function of a parallel magnetic field for different field orientations θ (fig 2.14 B, E).

The period of the oscillations depends on the field direction, and corresponds to one flux quantum through the surface enclosed by the two paths projected onto the y direction. Given the interference period $\phi_0/wL = 100\,\mathrm{G}$ in a perpendicular field B_z, where w is the nanowire's width, the measured period $\Delta B_\mathrm{y} = 500\,\mathrm{G} = \phi_0/tL$ yields a nanowire's thickness $t = 40\,\mathrm{nm}$. This would mean that the thickness of the nanowire is one half of the thickness of the Au electrodes, which agrees qualitatively with the tilted SEM image (fig 2.14 A).

The SQUID-like oscillations disappear faster with B along the y direction than with B along the z direction. This is consistent with the fact that the states are more delocalized in the y direction than in the z direction. The typical scale of the decay in the z direction can be obtained from a gaussian envelope function, giving 1800 G (fig. 2.14 F). We also observe a reduction of the decay scale in parallel field B_y : $B_\mathrm{d} = 700\,\mathrm{G}$ (fig 2.14 E). In the scenario of a nanowire of rhombohedral transverse section with an anistropic localization that prevents from observing SQUID-like oscillations, then assuming that the states are more delocalized along the (100) surface (fig. 2.14 B), implies that B_d should be $1800 \tan 57^\mathrm{o} = 1170\,\mathrm{G}$ in the y direction.

6 Inducing superconductivity with sputtered Pd electrodes

In order to study Bi nanowires in the normal state, we contacted one wire with electrodes made of sputtered Pd, which is a normal metal. Surprisingly, a superconducting transition was detected at 1.8 K. I will first review the existing literature that shows that Bismuth is very close to a superconductor, in the sense that there exists several ways to observe superconductivity in Bismuth even though pure Bi in its crystalline phase is superconducting only at very low temperatures $T \simeq 0.5\,\mathrm{mK}$. I will then describe the device that was measured in this experiment, and then expose the results showing unambiguously superconducting proximity effect. Finally, I discuss effects that could modify this observation such as inverse proximity effect and show that they are minimal.

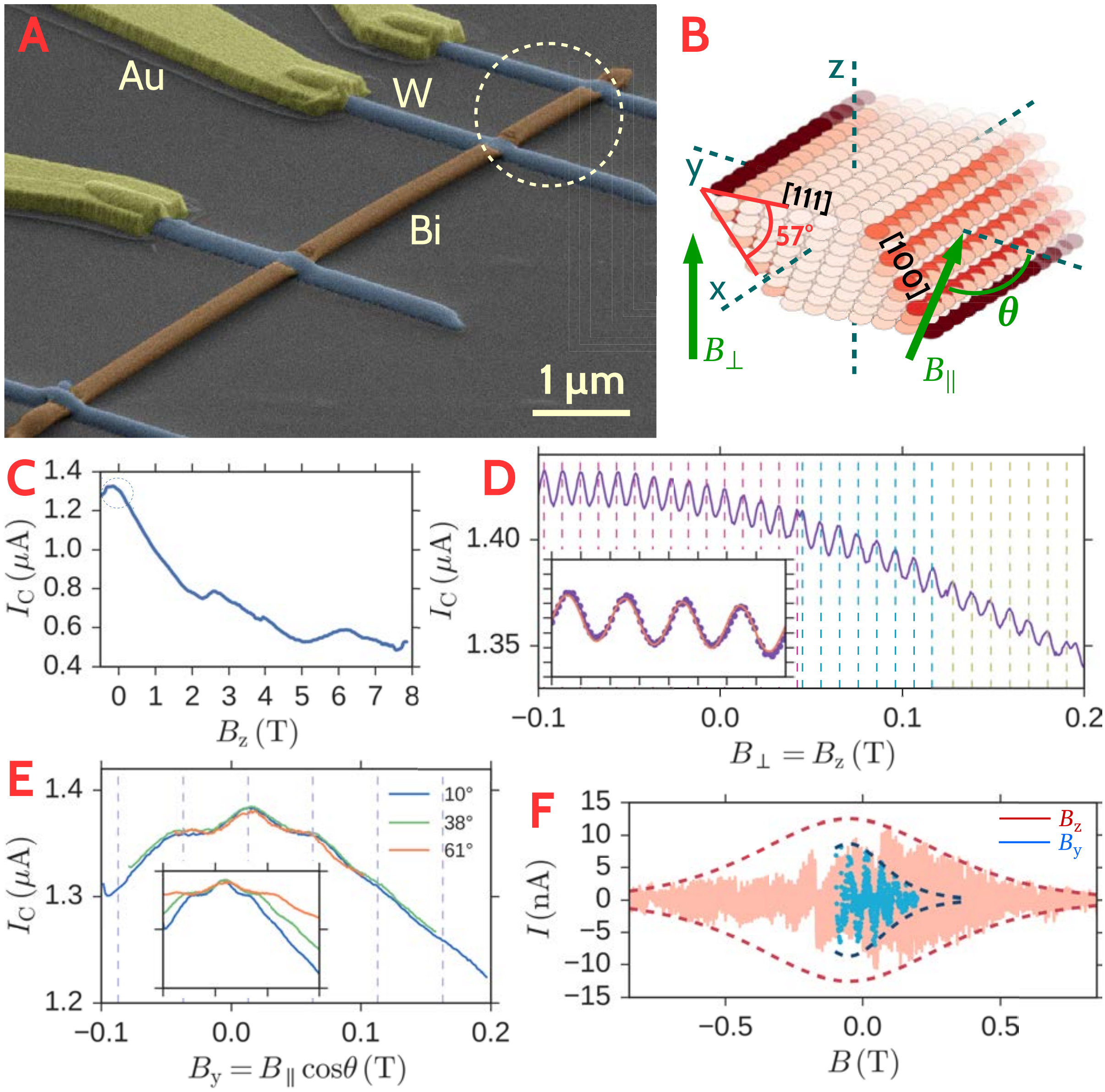

Figure 2.14: Magnetic field orientation dependence of the critical current in Bi 33. **A** : SEM image of the device with false colors. For this nanowire, only the sections encircled with white dashed lines displayed a supercurrent. **B** : Magnetic field orientation with respect to the axis of the nanowire. The LDOS calculated from tight binding simulations is plotted here. The angle between the (100) and (111) directions measures 57°. **C** : I_C vs B as a function of the perpendicular magnetic field B_z. **D** : SQUID-like oscillations at low magnetic field. The periods are indicated by dashed vertical lines. The different periods represent phase jumps. These jumps were not reproducible from an up sweep to a down sweep. Inset : Zoom of oscillations from -100 G to 300 G, yielding a period of 100 G. **E** SQUID-like oscillations in parallel magnetic field for different orientations of the magnetic field. The curves are rescaled by the projection of the magnetic field on the y direction. Inset : non rescaled data. **F** Amplitude of the SQUID-like oscillations as a function of the magnetic field B_z or B_y for large magnetic fields. Dashed lines : gaussian envelope functions.

6.1 Bismuth is close to a superconductor

Perhaps every metal is a superconductor, as predicted by Anderson (Morel & Anderson, 1962), although its critical temperature may be very small and the transition not observable at accessible temperatures. Previous studies on Bi based materials indicate that the combination of a very low density of states and electron-phonon coupling which prevents it from becoming a superconductor, can be easily broken. In particular this can be achieved either through amorphization, or by alloying. I review them here.

Recall the superconducting gap equation within BCS theory (Tinkham, 2004)

$$\Delta = \hbar\omega_{\mathrm{D}} e^{-1/(N(\epsilon_{\mathrm{F}})V)} \tag{2.43}$$

where ω_{D} is the Debye frequency, $V = V_{\mathrm{e-ph}} - V_{\mathrm{e-e}}$ is the effective attractive retarded interaction between electrons and $N(\epsilon_{\mathrm{F}})$ is the electronic density of states at the Fermi level. Despite the fact that this formula can only describe a subclass of low T_{C} materials termed BCS superconductors, it has proven to be quite predictive (Roberts, 1976). An important point that it conveys is that the stronger the $\lambda = N(\epsilon_{\mathrm{F}})V_{\mathrm{e-ph}}$ product, the stronger the superconducting gap will be. This provides two possibilities to increase superconductivity : one can either increase the density of states or increase the effective interaction. A third way would be to increase the Debye frequency.

The most common way to increase the density of states is through doping. It is indeed known to provide a way to strengthen superconductivity in materials. This has proven to be the case in several situations for example when doping diamond (Bustarret et al., 2006) or silicon (Ekimov et al., 2004) with B atoms. This phenomenon can even be observed through electrostatic gating in two dimensional superconductors, although to a smaller extent, for example at the LAO/STO interface (Bert et al., 2012) or for monolayer $\mathrm{NbSe_2}$ (Xi, Berger, Forró, Shan & Mak, 2016).

An early measurement of Bi using Ag contacts displayed some signatures of superconductivity, probably localized at the Bi/Ag interface (Esaki & Stiles, 1965). This was explained by the creation of a superconducting metastable intermetallic alloy $\mathrm{BiAg_2}$. In fact, subsequent measurement from 1966 showed that almost all non magnetic metallic bismuth compounds are superconducting (Matthias, Jayaraman, Geballe, Andres & Corenzwit, 1966).

On the other hand, amorphous Bi alone was also known to be superconducting since 1954 with a $T_{\mathrm{C}}^{\mathrm{a}} \simeq 6\,\mathrm{K}$ (Buckel & Hilsch, 1954) whereas non disordered Bi films do not show any superconducting transition down to 50 mK. Later, superconductivity was found to appear as one applies a local pressure (Shklyarevskii, Duif, Jansen & Wyder, 1986), the mechanism being either amorphization or a change of the crystal structure leading to the $\mathrm{Bi_{II}}$ phase, known to be superconducting. A recent ab-initio calculation on a disordered cluster of atoms distributed with a probability distribution function mimicking the one determined experimentally (Mata-Pinzón, Valladares, Valladares & Valladares, 2016) demonstrated that amorphisation leads to a four times larger $N(\epsilon_{\mathrm{F}})$, while ω_{D} is only slightly modified. Assuming no modification of V, this yields a $T_{\mathrm{C}}^{\mathrm{c}}$ of crystalline Bi as

$$T_{\mathrm{C}}^{\mathrm{c}} \simeq T_{\mathrm{C}}^{\mathrm{a}} \left(\frac{T_{\mathrm{C}}^{\mathrm{a}}}{\theta_D}\right)^3 \simeq 1.3\,\mathrm{mK} \tag{2.44}$$

where $\theta_D \simeq 100\,\mathrm{K}$ is the Debye temperature of amorphous Bi which agrees both with theory and estimation from experiments. This is an upper bound in the sense that taking

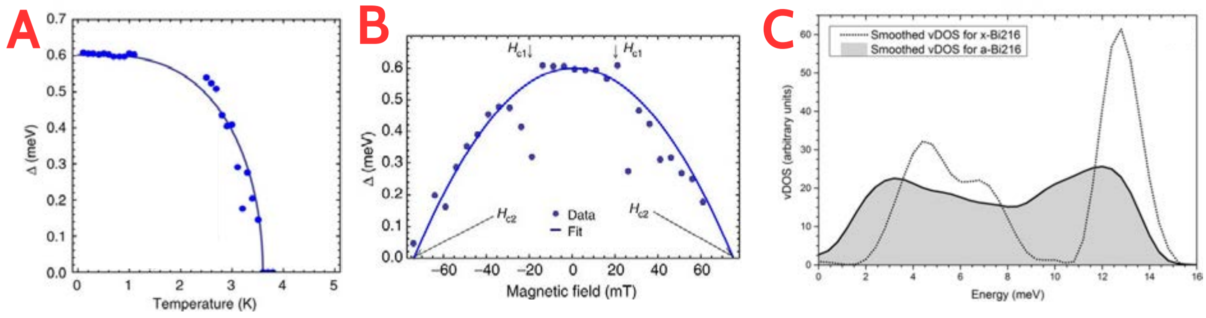

Figure 2.15: Different superconducting Bi based materials **A, B** : Temperature dependence of the superconducting gap and critical field measured in the BiPd superconductor. **C** : Phonon density of states $F(\omega)$ for crystalline (fine dotted curve) and amorphous Bi (solid, shaded curve) calculated ab-initio (Mata-Pinzon et al., 2016). Amorphization allows low frequency vibration modes also termed "soft modes", directly enhancing the parameter $\lambda = 2\int_0^\infty \omega^{-1}\alpha^2(\omega)F(\omega)\mathrm{d}\omega$ within McMillan theory, yet leading to a diminution of ω_{D} by only 10%.

a smaller value of V for the crystal would lead to an even (much) smaller value of $T_{\mathrm{C}}^{\mathrm{c}}$. In fact, a very recent experiment that was performed at very low temperatures using an adiabatic demagnetizing fridge, showed that pure crystalline Bi is indeed superconducting with a $T_{\mathrm{C}} = 0.53\,mK$ and an upper critical field of 5.2 μT (Prakash, Kumar, Thamizhavel & Ramakrishnan, 2016).

Several theoretical studies find that the electron-phonon coupling is dramatically increased by amorphisation. It has long been known that amorphous Bi is a strong coupling superconductor (Chen, Chen, Leslie & Smith, 1967), with $\lambda = 2.46$ which is even stronger than Pb. On the other hand, theoretical calculations find that crystaline Bi should have a very small λ : 0.09, 0.13, 0.236 (upper bound).

Furthermore, the mere effect of size reduction may also be a determining factor for increasing the electron-phonon coupling, yielding $\lambda \simeq 0.45$ (Alcántara Ortigoza et al., 2014) for the outer bilayers, where the structural relaxation occurs. Therefore, the effect of size reduction can also enhance superconductivity, as it has recently been observed for few atoms thick TaS_2 films (Navarro-Moratalla et al., 2016). Of course when the size is too small, superconductivity should be destroyed due to quantum size effects (Anderson, 1959), and this has been verified experimentally on strongly disordered Bi thin films (Kubatkin & Landau, 1989), or by decreasing the film thickness (Liu, Haviland, Nease & Goldman, 1993).

Polycrystalline Bi films can therefore display superconductivity either in rough and randomly disposed polycrystals (Baring, Silva & Kopelevich, 2011), or on the form of well defined connected rhombohedral clusters (Weitzel & Micklitz, 1991). Interestingly, it has even been found in isolated individual grains (Johnson, Nieskoski, Disseler, Huber & Graf, 2013). This can now be understood easily as being the consequence of either a superconducting amorphous Bi surrounding these crystals or a finite size enhancement of superconductivity. Therefore, the observation of superconductivity in polycrystaline Bi nanowires (Tian et al., 2006) is not a surprising fact. Yet, all measurements on polycrystalline nanowires do not show superconductivity but sometimes only a weak signature in the resistance (Tian, Kumar, Chan & Mallouk, 2008). This demonstrates that this superficial superconductivity is a priori too weak to develop a zero resistance state in polycristals by proximity effect.

These observation raise an important question from the superconducting proximity effect standpoint. Pure Bi being a high mobility material it can consequently have a very large electronic mean free path. This implies that the propagation of pair correlations induced by doping could reach great distances. However, because it is localized at a surface, this superconductivity could be too weak and not induce a zero resistance state. Moreover, doping by metal alloying, as originally discovered by Esaki and Stiles, implies a strong weakening due to inverse proximity effect. To what extent can the interfacial superconductivity found in Bi develop into a full superconducting proximity effect ?

6.2 Device description

We fabricated a junction made of Bi connected with Pd electrodes. The Bi nanowire was grown by the sputtering technique described in chap 7. Its length $L = 6\,\mu$m was determined by optical microscopy and its diameter was estimated to be between 100 nm and 200 nm from similarly grown nanowires from the same batch observed with SEM. The contacts were made of 63 nm sputtered Pd contacts, with a DC power of 150 W and an Ar flow of 15.4 sccm in a vacuum better than $3 \cdot 10^{-7}$ mbar. Beforehand, an etching step was performed using IBE with Ar^{+} ions at an accelerating voltage of $200\,V$ for 15 s. This corresponds to an etching of the order of 30 nm of Bi. Four such contacts were made on the nanowire, realizing a pseudo four probe situation. The distances between the contacts were $0.6\,\mu m$ for the two outer regions and $2\,\mu m$ for the inner region (fig 2.16). The two inner contacts were $0.5\,\mu m$ wide and the outer contacts were $1\,\mu m$ wide.

6.3 Regime of proximity effect

The four wire resistance of the central region was measured with a lockin amplifier with 0.1 nA bias current, as a function of the temperature. At temperatures below 4.2 K the resistance undergoes a broad superconducting transition from $R = 222\,\Omega$ to $R = 184\,\Omega$ at 1.8 K with a resistance jump of $36\,\Omega$, and an exponential broadening with characteristic temperature $\theta\mathrm{b} = 243\,mK$. The corresponding superconducting gap is therefore $\Delta = 1.76 T_{\mathrm{C}} = 272\,\mu$eV. At lower temperatures, a second transition to a zero resistance state is observed with an onset around 400 mK. The observation of a change in the contact resistance for this four probe geometry is not surprising as the inner probes are actually invasive (fig 2.16B). The second transition to a zero resistance state can only be explained by the superconductivity induced in the Bi nanowire by the contacts. Since we have etched Bi before depositing Pd, we were first tempted to explain the induced superconductivity by the presence of a layer of amorphous Bi between the Pd and the Bi nanowire. However, this explanation does not hold, as superconductivity was not found on nanowires that were purposely etched on their entire length using IBE an then contacted with Nb. We came to the conclusion that the doping from the Pd is crucial for the superconductivity in this system. Moreover, this hypothesis is corroborated by the fact that the BiPd alloy is known to be superconducting with a similar $T_{\mathrm{C}} = 3.7$ K (Sun et al., 2015) to the $T_{\mathrm{C}} = 1.8$ K we measure.

The temperature dependance of the resistance for this second transition can be interpreted by a phase diffusion mechanism driven by thermal fluctuations. In the limit of the overdamped junction, which is justified because the junction is not hysteretic (see below), a phase diffusion leads to a finite voltage proportional to the bias current I_{b} in the limit

$I_{\mathrm{b}} \rightarrow 0$. Within the RSJ model, a finite resistance can be measured (Chauvin, 2005)

$$R(T) = R_{\mathrm{N}} J_0^2 \left(\frac{\gamma_0(T)}{2} \right) \tag{2.45}$$

where $\gamma_0(T) = \phi_0 I_{\mathrm{c}}(T)/\pi k_{\mathrm{B}} T$ is the damping, J_0 is the modified 0th order Bessel function, and R_{N} is the shunt resistance, interpreted as the resistance in the normal state. The temperature dependent critical current $I_{\mathrm{C}}(T)$ is related to R_{N} and the effective gap Δ^* through

$$e R_{\mathrm{N}} I_{\mathrm{C}}(T) = \frac{\pi}{2} \Delta^* \tanh \left(\frac{\Delta^*}{2 k_{\mathrm{B}} T} \right) \tag{2.46}$$

As a result, the temperature dependance of the resistance is

$$\frac{R_{\mathrm{N}}}{R(T)} = J_0^2 \left(\frac{h}{8e^2 R_{\mathrm{N}}} \frac{\Delta^*}{k_{\mathrm{B}} T} \tanh \left(\frac{\Delta^*}{2 k_{\mathrm{B}} T} \right) \right) \tag{2.47}$$

Although this formula is valid for an SIS junction, it yields a good agreement with the experimental data, with a characteristic energy $\Delta^* = 128.5\,\mathrm{mK} = 11.05\,\mu\mathrm{eV}$ (fig 2.16D).

The existence of a superconducting interfacial region between the contact and the Bi nanowire is plausible. However, one can wonder why the superconductivity in the BiPd film is not destroyed by the normal Pd electrode (inverse proximity effect). We believe that the inverse proximity effect is strongly reduced for highly disordered superconducting thin films whose coherence length ξ is very short and of the order or below the film thickness t (Fominov & Feigel'man, 2001). Therefore, it is reasonable that a full superconducting proximity effect could occur in the Bi nanowire induced by a small superconducting alloy. In the next paragraph we estimate these two parameters and show that the condition $t \simeq \xi$ is fulfilled.

6.4 Characteristic parameters of the superconducting contacts

From the differential resistance data taken for larger bias current, one can deduce the critical current $I_{\mathrm{C}} = 5\,\mu\mathrm{A}$ and the critical perpendicular magnetic field $B_{\mathrm{C}} = 0.17\,\mathrm{T}$ of the superconducting contact 2.18. The superconducting coherence length in the contact is then estimated by $\xi = (\Phi_0/4\pi B_{\mathrm{C}})^{1/2} \simeq 30\,\mathrm{nm}$. From this value one can extract the diffusion coefficient and the mean free path $l_e \simeq 0.5$nm from $\xi = (\hbar D/\Delta)^{1/2}$. Such a very small mean free path is not surprising in this highly disordered BiPd alloy. The thickness t of the contact can in turn be estimated from the contact resistance:

$$R_c = \frac{h}{2e^2} \frac{t/l_e}{M} \simeq 18\,\Omega \tag{2.48}$$

where $M = S/(\lambda_{\mathrm{F,Pd}}/2)^2 \simeq 10^5$ is the number of channels connecting the alloy region and $S = 150\mathrm{nm} \times 500\mathrm{nm}$ is the section of the contact covering the Bi wire. We find $t \simeq 50\,\mathrm{nm}$. These values of M and t rely on the assumption of the formation of a uniform ohmic contact on the Bi wire. They are probably over-estimated. Our data are anyhow consistent with $t \simeq \xi$.

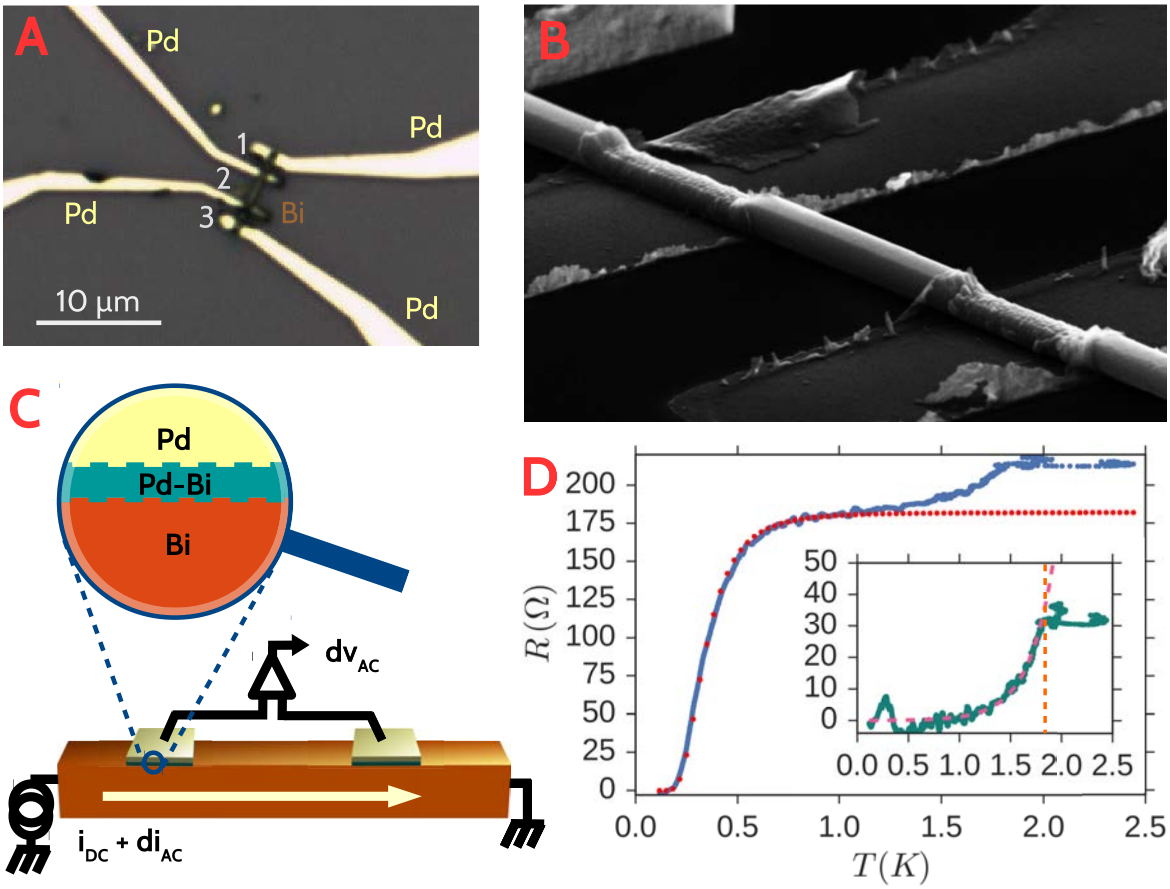

Figure 2.16: Induced proximity effect with sputtered Pd electrodes **A** : Optical image of the measured Bi nanowire connected with Pd contacts. **B**: SEM image with angle of a Bi nanowire with Pd contacts deposited after IBE milling of 30 s. The etched part is clearly visible and displays some roughness provoked by the etching. Some facets of the nanowire are visible indicating the crystalline nature. **C**: Cartoon of contact region and the measurement setup. At the contact region the Pd makes a superconducting disordered alloy with the Bi. The differential is then measured in four probe configuration for the section 2 of the nanowire using a standard lockin technique. **D**: Resistance vs temperature between 120 mK and 2.5 K. Dashed, red line : fit of the temperature dependent resistance using Zilberman-Ivanchenko formula. Inset : the resistance subtracted from the fit displays an exponential behavior with a characteristic temperature $\theta_{\mathrm{B}} \simeq 0.28\,K$

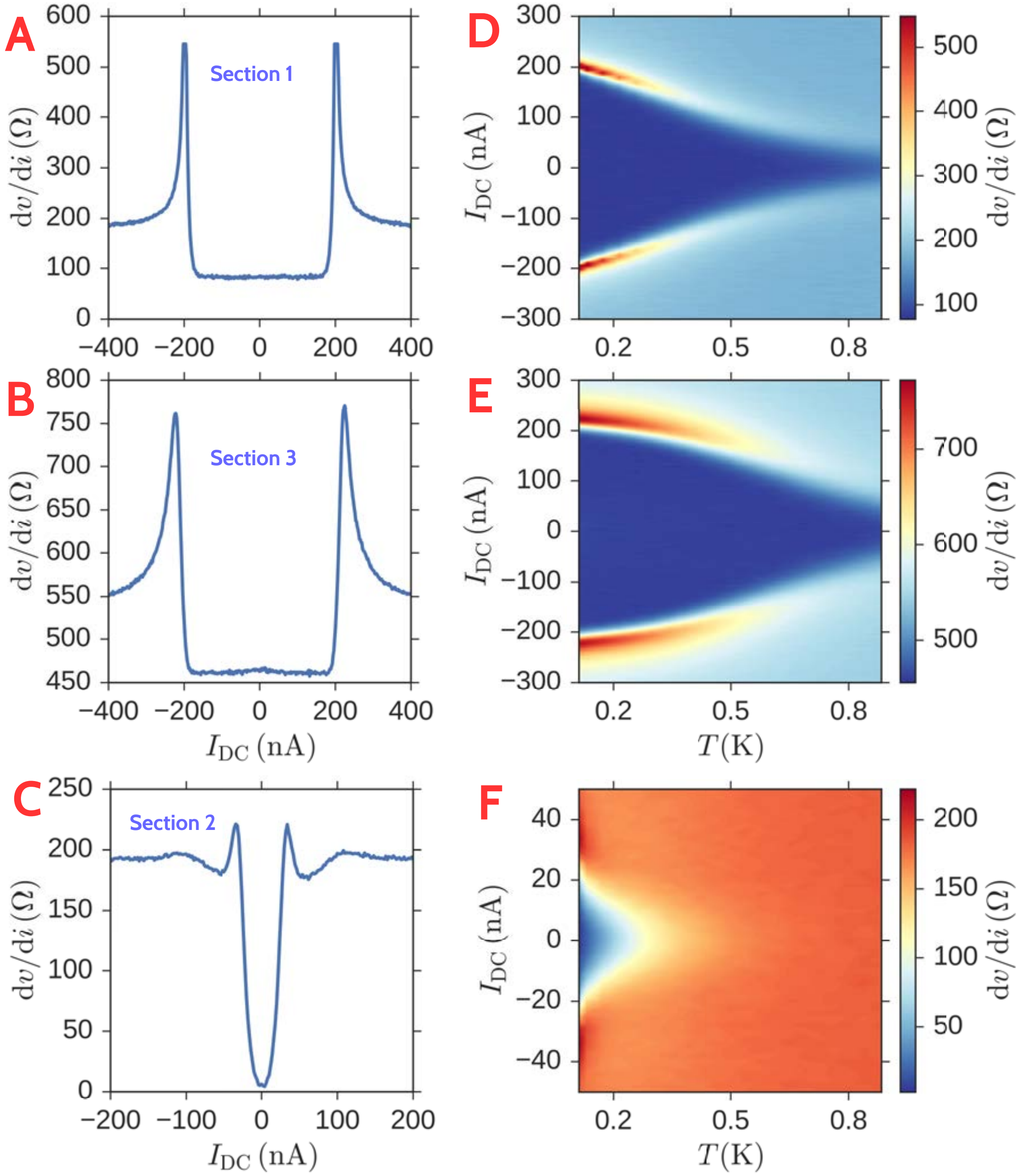

Figure 2.17: Temperature dependence of the proximity effect found in the devices. **A-C** : dvdi vs i for the sections 1 (A), 2 (C) and 3 (B). Note the large offset resistance coming from the Pd contacts in sections 1 and 3, as they are measured in a two probe configuration. **DF** : dvdi (color) vs bias current and temperature for the corresponding sections.

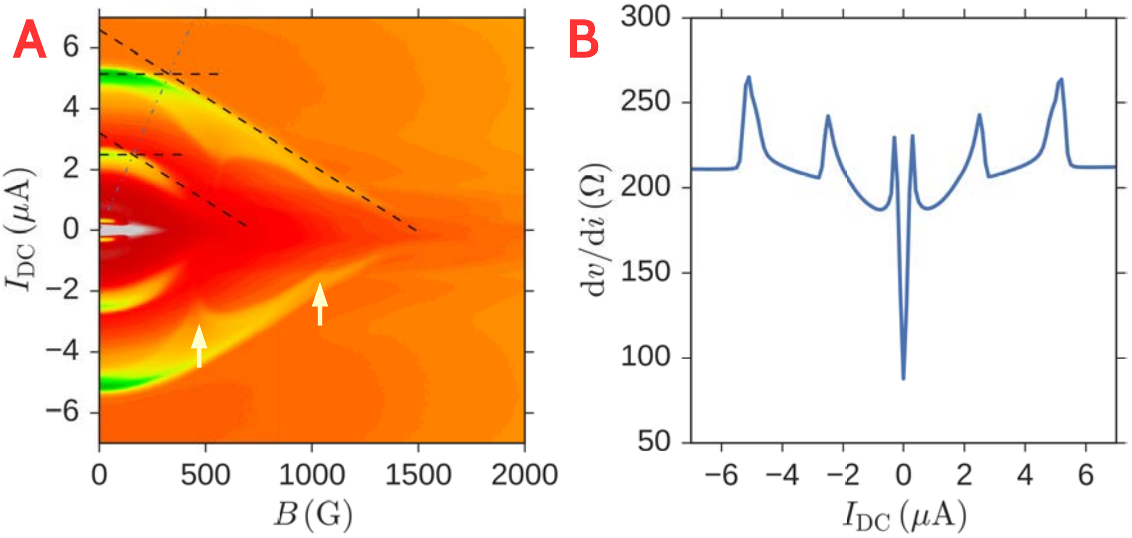

Figure 2.18: Differential resistance versus bias current and transverse (perpendicular) magnetic field, for large bias currents. It reveals the behaviour of the critical current of the contacts as a function of the magnetic field. **A** : dvdi (color) vs i (vertical) and B (horizontal) for the section 1 of the Bi-Pd sample. The dashed line indicates the critical current of the contacts in the current dominated deparing regime (horizontal lines) and in the magnetic field dominated regime (canted lines). The blue dashed-dotted line indicate the location of the crossover between the two regimes in the I-B plane, for a fixed aspect ratio of the contact. The white arrows indicates some seemingly periodic oscillations of the critical current of the contact. The period corresponds to a flux of $\phi_0/2$ in the surface of the contact. **B** : dvdi vs i cut at B=0. The narrow jump at low bias currents corresponds to the destruction of proximity effect, while the jumps at higher bias currents is due to the contacts becoming normal.

6.5 Discussion

The fact that T_C and $H_C^\perp$ are not so much reduced from the values corresponding to the bulk, agrees with the theory that predicts small reduction for large ρ_{int}. More quantitatively for $\rho_{\text{int}} \simeq 150$, following the calculation of Feigelman and Fominov, the T_C would be 30% of the bulk value at most (we find 47%) and 20% for $H_C^\perp$ (we find 28%). This indicates either that ρ_{int} has been underestimated or even that the pairing properties of the interfacial alloy are different from the bulk (different electron-phonon coupling or density of states).

Interestingly, a zero resistance was measured in Bi nanowires connected to FIB deposited Pt contacts (Tian, Wang, Ning, Mallouk & Chan, 2015). We suspect that at the Bi-Pt interface, the intermetallic alloy BiPt known to be superconducting since a long time (Matthias, 1953) with a $T_C = 1.3\,\text{K}$, could induce a superconducting proximity effect similarly to what we observe. Furthermore, some oscillations of the resistance at zero bias current were also observed, which could be related to the physics of edge states that is detailed in the next part.

Finally, the small superconducting layer of PdBi alloy is protected from the inverse proximity effect at the disordered PdBi - Pd interface because it has a large value of the resistivity per channel ρ_{int}, which prevents the leakage of pair correlations into the Pd. On the other hand, the fact that the Fermi wavelength is larger inside the bulk of Bi nanowire leads to an overall decrease of the number of channels. As a result, for the same disorder, the parameter ρ_{int} gets smaller at the PdBi - Bi interface and the pair correlations can increase inside the nanowire : the superconducting proximity effect can take place.

In conclusion, I believe that this behaviour is generic and should happen with a large variety of contacts.

6.6 Magnetic field dependence

For the Bi nanowire connected with Pd electrodes, we observe oscillations of the critical current for at least one of the junctions (fig 2.19). The junction 1 displayed four quasiperiodic oscillations, with an average period of 150 G and the junction 3 displayed one damped oscillation with period of 170 G.

The width w inferred from the average period ΔB through

$$w = \frac{\phi_0}{(\Delta B)L} \tag{2.49}$$

gives $w = 222\,\text{nm}$ for the junction 1 and $w = 195\,\text{nm}$ for junction 3, which agrees with the estimated width of the nanowire. However, given that the length of the junction is greater than the diameter by a factor $L/w \simeq 4$, no oscillations are expected.

These SQUID like oscillations present similarities with those observed in the W FIB contacted Bi nanowires discussed in the previous sections. However in the present case we observe a complete modulation of the supercurrent whereas the amplitude of the modulations observed on the W connected Bi nanowires did not exceed 10%. This indicates that in this sample the transmission between the 2 interfering paths are of the same order of magnitude which was not the case for the previous devices.

Two other observations can be made on this oscillatory pattern. First, the height of these oscillations is non monotonic, which again disagrees with the expected gaussian behaviour. Second, the location of the minima and maxima of the critical current displays an increase as a function of B (2.20A).

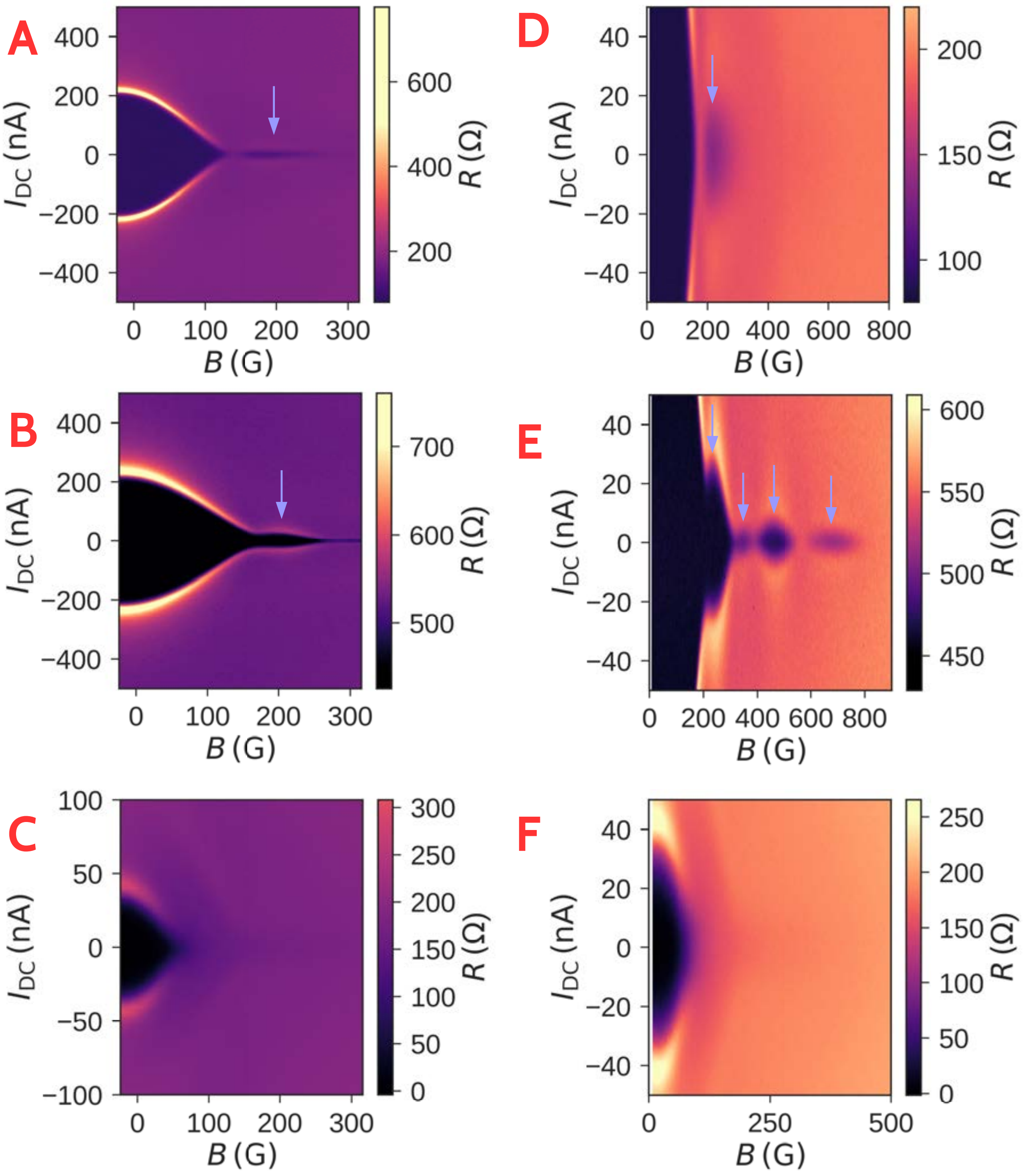

Figure 2.19: Low field oscillations of the critical current for the three different segments of the Bi-Pd sample measured at 120 mK. A,B,C : I-B map of the differential resistance for the junctions 3, 1 and 2. Blue arrows indicate the first lobe of the oscillations. C,D,E : Zoom of the low field oscillations for the corresponding sections.

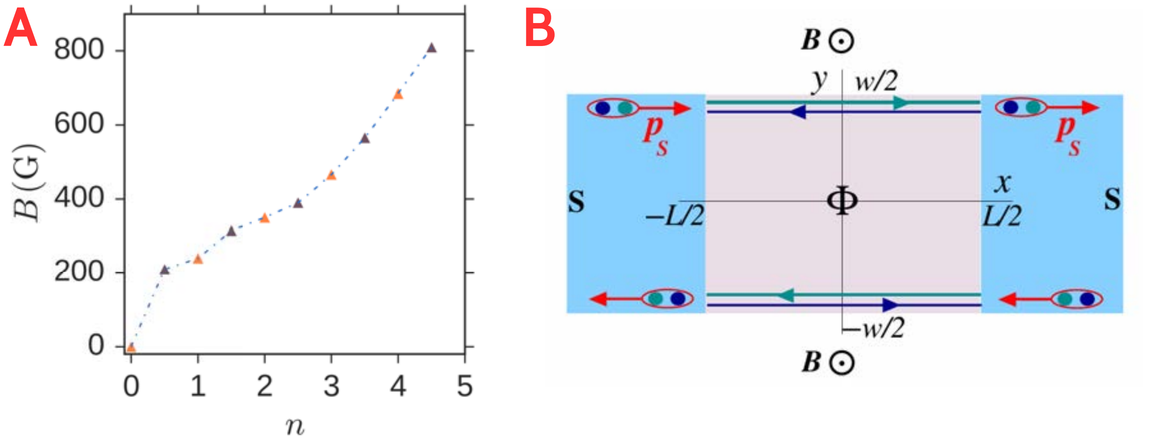

Figure 2.20: Doppler shift of the oscillations. A: Location of the successive maxima (orange triangles) and minima (purple triangles) of the Fraunhoffer pattern as a function of the index. B: Schematic picture of a quantum spin hall Josephson junction in a magnetic field. The Doppler shift results from the the difference of momentum acquired by both edges due to the difference of potential vector. From Tkachov et al. 2015

We could interpret it by a shielding response from the contacts (Tkachov, Burset, Trauzettel & Hankiewicz, 2015). Indeed, in the scenario of supercurrent carrying edge states, a local gradient of phase will appear in the contacts due to the wide geometry (fig 2.20). This results in a different value of the momentum of the Cooper pairs condensate from one edge compared to the other

$$p_{\mathrm{s}}(B) = \pm \pi \hbar \frac{Bw}{\phi_0} \tag{2.50}$$

This results in a magnetic field dependent phase shift $\arccos(v_{\mathrm{F}} p_{\mathrm{s}}/2\Delta)$ in the Andreev equation that competes with the phase dependence coming from the orbital flux ϕ/ϕ_0. This results in

- an increase of the period as a function of the magnetic field
- a non compensation of the phase dependence of the current for both edges, and therefore the height of oscillations will alternate as a function of B : this is an amplitude modulation.

This shielding effect is significant above a typical magnetic field scale

$$B_{\mathrm{AR}} = \frac{2\phi_0}{w\xi_*} \tag{2.51}$$

where $\xi_* = \min\left(\hbar v_{\mathrm{F}}/\Delta, \hbar v_{\mathrm{F}}/\pi k_{\mathrm{B}} T\right)$. In our case, using $v_{\mathrm{F}} = 10^6\,\mathrm{m/s}$ and $T = 130\,\mathrm{mK}$, we have $\hbar v_{\mathrm{F}}/\pi k_{\mathrm{B}} T \simeq 28\,\mu\mathrm{m}$ and $\frac{\hbar v_F}{\Delta} \simeq 1.1\,\mu\mathrm{m}$. Therefore the limitation occurs due to the coherence length, and $B_{\mathrm{AR}} \simeq 90\,\mathrm{G}$ which allows the effect to be observable.

7 Conclusion of this chapter

The fabrication of crystalline Bi nanowire with small diameter and the use of powerful characterization techniques allows us to study well defined quasi one dimensional systems with strong spin orbit interaction. The magnetoresistance measurements in the normal state revealed different types of carriers, that can be used as an indicator for the effective dimensionality of the system. More importantly, transport measurement in the normal state show that the conduction is dominated by the surface states rather than the bulk.

For Bi wires connected to W electrodes, the critical current was shown to persist up to very high magnetic fields, which is a very unusual behavior for superconducting proximity effect. Two types of oscillations were observed and were attributed to two types of interferences controlled by the magnetic field. The orbital effect results from interferences between trajectories that are located at the periphery of the sample, leads to SQUID-like oscillations pattern with a magnetic field period $\Delta B = \phi_0/S$. The Zeeman effect results in an oscillatory signal with larger period $\Delta B = E_\mathrm{T}/g\mu_\mathrm{B}$.

We also observed induced superconductivity in Bi nanowires with normal Pd electrodes at low temperatures. We think that this was possible due to the disordered superconducting PdBi alloy that is protected from the inverse proximity effect in the Pd electrode on one hand, and on the other hand lets pair correlations to proximitize the nanowire due to the fewer conducting channels in Bi.

The scenario where the supercurrent is carried by states located at the edges of the sample calls for a direct confirmation using a phase biased detection experiment. Moreover, the spin-momentum locking in the system should have very strong consequences. In the next chapter, I will present some measurement of the current-phase relation on the Bismuth that reveals the ballistic conduction through few narrow channels.

Chapter 3

Measurement of the current phase relation of Bi nanowires based Josephson junctions

In this chapter I describe the measurement of the current phase relation (CPR) of Bi nanowires. I start by recalling the CPR in known cases, then explain the technique used for the fabrication and the measurement. I then describe the measured CPR, which leads to the conclusion that the supercurrent is carried by ballistic edge states in the two samples we have measured.

1 Introduction

When a normal metal is connected to superconducting electrodes making a so called SNS junction, the current is carried by Andreev bound states (ABS) which are coherent superpositions of electrons and holes. This current is dissipationless, similarly to the supercurrent found in superconductors. The measurement of the critical current, defined as the maximum supercurrent the SNS junction can sustain, gives already some information about these states. Measuring the magnetic field dependence of the critical current can provide an idea about the phase breaking mechanism : the orbital effect or the Zeeman effect. In the previous chapter, we showed that the orbital dephasing breaking mechanism effect is very weak in Bi nanowires.

In particular, the ABS energy is sensitive to the phase difference φ between the superconducting contacts leading to an Andreev spectrum that encodes the information both about propagation through the normal metal and the reflection at the NS interface. The current carried by these states is related to the spectrum according to

$$i(\varphi) = -\frac{2e}{h}\sum_n f_n \frac{\partial \epsilon_n}{\partial \varphi} \tag{3.1}$$

where each individual level carry a supercurrent $i_n = -\frac{2e}{h}\partial_\varphi \epsilon(\varphi)$. The minus sign is reminiscent of the diamagnetic response of a superconductor (the Meissner effect). It will be absorbed in an amplitude prefactor in the rest of the manuscript.

Therefore the measurement of the CPR, i.e. the supercurrent of a phase biased SNS junction, is of fundamental importance to understand the propagation of its charge carriers. I will now review the CPRs of SNS junctions in some important limiting cases.

2 Current phase relation of model junctions

2.1 Scattering matrix formalism

The formation of ABS can be understood formally by using scattering matrix formalism (Nazarov & Blanter, 2009). In this formalism, the propagation in the electron-hole channel is described by a spinor $\Psi = (\Psi_{\mathrm{e}}, \Psi_{\mathrm{h}})^{\mathrm{T}}$, where Ψ_{e} and Ψ_{h} are themselves Bogoliubov spinors

$$\begin{aligned}\Psi_{\mathrm{e}} &= (\psi_{\uparrow}, \psi_{\downarrow})^{\mathrm{T}} \\ \Psi_{\mathrm{h}} &= (\psi^*_{\uparrow}, \psi^*_{\downarrow})^{\mathrm{T}}\end{aligned} \tag{3.2}$$

This formalism allows to take into account the imperfect Andreev reflection processes by including a finite normal transmission at the interface. However, note that it works well for 1D cases but is less explicit for more complicated systems. I will describe it now.

One starts from the Bogoliubov-de Gennes (BdG) equations describing the propagation of electrons and holes in presence of a pair correlations :

$$\begin{pmatrix} H_N & \Delta(x) \\ \Delta^{\dagger}(x) & -H_N^* \end{pmatrix} \Psi = \epsilon\Psi \tag{3.3}$$

where H_N is the hamiltonian of the normal metal, $\Delta(x)$ is the order parameter that vanishes inside the N and is equal to a constant Δ_0 inside the S. For practical purposes, it is described by a step function at the interface. Assuming $k_{\mathrm{F}}\xi \gg 1$, one can approximate the spinor Ψ by an enveloppe function $\Psi \simeq \tilde{\Psi}(x)\mathrm{e}^{ik_{\mathrm{F}}x}$ where $\tilde{\Psi}$ is a slowly varying function in space, on a scale $\xi \gg 2\pi/k_{\mathrm{F}}$.

We can linearize the kinetic energy term in the BdG equation

$$\begin{pmatrix} -i\hbar v_{\mathrm{F}}\frac{\mathrm{d}}{\mathrm{d}x} & \Delta(x) \\ \Delta^{\dagger}(x) & i\hbar v_{\mathrm{F}}\frac{\mathrm{d}}{\mathrm{d}x} \end{pmatrix} \tilde{\Psi} = \epsilon\tilde{\Psi} \tag{3.4}$$

Assuming $\epsilon < \Delta$, the solutions can be computed in the uniform, infinite normal case

$$\tilde{\Psi}(x) = \mathrm{e}^{i\epsilon x/\hbar v_{\mathrm{F}}} \tag{3.5}$$

and in the superconducting case

$$\tilde{\Psi}(x) = \mathrm{e}^{-\sqrt{\Delta^2-\epsilon^2}|x|/\hbar v_{\mathrm{F}}} \tag{3.6}$$

The latter solution is evanescent as no electron-like or hole-like propagation can be found due to the condition $\epsilon < \Delta$, leading to a vanishing density of states.

At the NS interface, one can match these two solutions. As a result, the hole solution propagating in the opposite direction is

$$\Psi_{\mathrm{h},-} = r_{\mathrm{A}}\Psi_{\mathrm{e},+} \tag{3.7}$$

where the reflection coefficient $r_{\mathrm{A}} \equiv \mathrm{e}^{-i\alpha}$ is a pure phase factor. Indeed, the incident wave cannot be transmitted in the superconductor at $\epsilon < \Delta$ and therefore has to be fully reflected $|t|^2 = 0$ and $|r_{\mathrm{A}}|^2 = 1$. The expression for this coefficient is

$$\mathrm{e}^{-i\alpha} = \frac{\epsilon}{\Delta} - i\frac{\sqrt{\Delta^2-\epsilon^2}}{\Delta} \tag{3.8}$$

The conversion of electrons into holes is described by a scattering matrix $\hat{S}_{eh}$ and the propagation in the normal metal is described by a conventional S matrix.

Finally, one can assemble these matrices into a secular operator

$$\hat{\Pi} = \hat{S}_N(\epsilon)\hat{S}_{eh}\hat{S}^*_N(-\epsilon)\hat{S}_{he} \tag{3.9}$$

This operator describes the succession of Andreev reflection and propagation through the normal metal from the point of view of electron-hole pairs. More precisely, it describes the following successive processes, starting from an electron-like excitation

- the electron-like excitation propagates forward (with positive velocity)
- reflects into a hole-like excitation
- propagates backwards in space (with negative velocity)
- reflects into an electron-like excitation

A dual sequence applies starting from a hole-like excitation. A bound state is found at the condition that

$$\mathrm{Det}\left(\hat{\Pi} - \hat{1}\right) = 0 \tag{3.10}$$

Finally we conclude by stressing that the existence of ABS results from the coherent superposition of successive Andreev reflections at the two NS interfaces, similarly to a cavity where the resonances result from the coherent superposition of reflected probability amplitude on the mirrors. Therefore, the ABS are non local in nature. In this sense, they are very different from excitons. Indeed, in semiconductors, the binding potential is the semiconducting gap, which makes the excitons local in nature. This non-local nature of ABS makes them very sensitive to boundary conditions, and as a result they carry intrinsically the information about them. In particular, they depend crucially on the difference between the macroscopic phases of the wavefunction describing the superconducting Cooper pair condensates of the two electrodes.

2.2 Single channel, clean limit

In the case of one channel, in the clean limit, the scattering matrix describing propagation is simply given by

$$\hat{S}(\epsilon) = \begin{pmatrix} 0 & \mathrm{e}^{-\epsilon L/\hbar v_\mathrm{F}} \\ \mathrm{e}^{-\epsilon L/\hbar v_\mathrm{F}} & 0 \end{pmatrix} \tag{3.11}$$

and the scattering matrix describing the electron hole conversion at the interface by

$$\hat{S}_{eh} = \mathrm{e}^{-i\alpha} \begin{pmatrix} \mathrm{e}^{-i\varphi} & 0 \\ 0 & \mathrm{e}^{i\varphi} \end{pmatrix} \tag{3.12}$$

The secular operator is therefore

$$\hat{\Pi} = \mathrm{e}^{-2i\alpha} \begin{pmatrix} \mathrm{e}^{i\varphi - i\epsilon L/\hbar v_\mathrm{F}} & 0 \\ 0 & \mathrm{e}^{-i\varphi - i\epsilon L/\hbar v_\mathrm{F}} \end{pmatrix} \tag{3.13}$$

A bound state is found at the condition that

$$\begin{aligned} \mathrm{Det}\left(\hat{\Pi}-\hat{1}\right) &= 0 \\ \exp\left(\frac{2i\epsilon L}{\hbar v_F}+2i\arccos\left(\frac{\epsilon}{\Delta}\right)\pm i\varphi\right) &= 1 \\ \frac{\epsilon L}{\hbar v_F}+\arccos\left(\frac{\epsilon}{\Delta}\right)\pm\frac{\varphi}{2} &= n\pi, \qquad n\in\mathbb{Z} \end{aligned} \tag{3.14}$$

This result shows that ABS exists at the condition that the total accumulated phase is an integer multiple of 2π.

We can solve this equation in two different limits

- the short junction limit $L \ll \xi$, one can neglect the propagative term $\epsilon L/\hbar v_F$, and the equation leads to

  $$\epsilon(\varphi) = \pm\Delta\cos(\varphi/2) \tag{3.15}$$

  the spectrum is composed by two cosine functions (fig 3.1A)

- the long junction limit $L \gg \xi$, where the propagative term is dominant, and the energy scale Δ is absent in the problem. As a result, one has below the gap

  $$\epsilon_n(\varphi) = \frac{\hbar v_\mathrm{F}}{L}\left(n\pi \pm \varphi/2\right) \tag{3.16}$$

  In this case the spectrum is composed by linear segments (fig 3.1E). One should also take into account the spectrum just above the gap that has a small phase dependence.

Once the Andreev spectrum and its dependence with respect to the phase is known, one has to determine the thermodynamic occupation f_n. At zero temperature, all the states below the Fermi level are filled, and all the states above are empty. The current is then obtained by taking the derivative of the energies $\epsilon_n(\varphi)$ whose states are occupied, with respect to the phase

$$i(\varphi) = -\frac{2e}{h}\sum_n f_n \partial_\varphi \epsilon_n(\varphi) \tag{3.17}$$

For the short junction case, the CPR is a piecewise sine function (fig 3.1B), while for the long junction, it is a piecewise linear function (fig 3.1F).

It is interesting to note that the original $\varphi/2$ dependence of the energy levels (3.15) (3.16) leads to a φ dependence of the resulting current. This is directly related to the existence of an energy level crossing at π.

However in practice, there always exists a finite transmission at the interface, which results in the level crossing at π (and also at 0 for the long junction) to be avoided due to mixing of Andreev reflection and normal reflection. The Andreev levels are thus effectively coupled at the vicinity of π leading to a gap opening (fig 3.1C,G). As a result, the CPR is strongly affected by this behavior and loses its sharpness at π (fig 3.1D,H). The same happens in presence of disorder in the normal metal.

The anharmonicity of the CPR can be translated as a number of Andreev reflections performed before a scattering event occurs. This can be illustrated in Fourier components

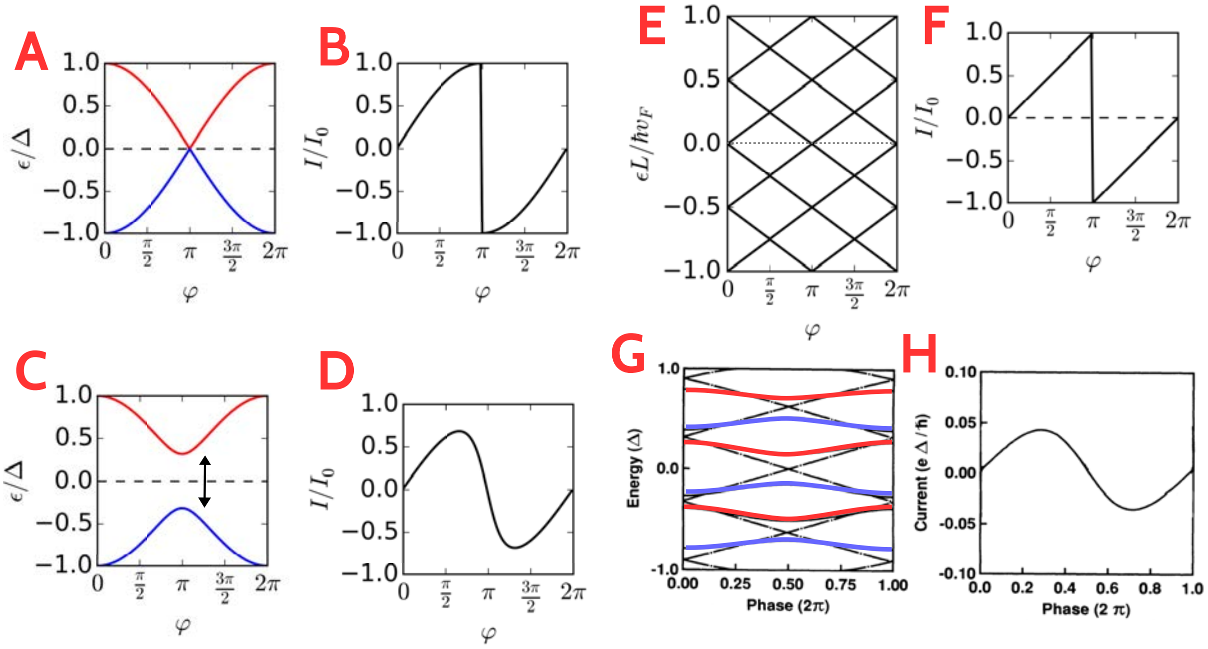

Figure 3.1: Spectrum (left) and CPR (right) of single channel SNS junction in different regimes. **A-B** Short junction in the clean limit. The solid blue line corresponds to the occupied state. **C-D** Short junction with finite transmission τ. The arrow corresponds to a gap opening of $\Delta\sqrt{1-\tau}$. **E-F** Long junction, clean limit. In the spectrum, the dashed lines are solutions with odd integer n, the solid lines are solutions with odd integer n. The blue (red) curve corresponds to solutions with positive (negative) current. **G-H** Long junction with finite transmission, from (Bagwell 1992). The black line corresponds to the clean limit, the blue (red) curve corresponds to the states with opposite contribution to the current. Note that one has also to take into account the slightly phase dependent levels above the gap in order to get the correct current in this case.

$$i(\varphi) = i_0 \sum_{m=1}^{\infty} a_m \sin(m\varphi) \tag{3.18}$$

The components are given by

$$a_m = \begin{cases} \dfrac{(-1)^{m+1}}{m} & L \gg \xi \\ \dfrac{(-1)^{m+1} m}{m^2 - 1/4} & L \ll \xi \end{cases} \tag{3.19}$$

In presence of bad interfaces or disorder, one can phenomenologically introduce a parameter $t \in [0, 1]$, that modify the Fourier coefficients

$$a_m \to a_m t^{2m} \tag{3.20}$$

We interpret t^2 as an effective transmission that is encountered m times during the processes of Andreev reflection - propagation, and describe both the effects of disorder or bad interfaces. When $t \to 1$, one recovers the original CPR, and when $t \to 0$ one obtains a sine CPR. One can thus understand the transition from an anharmonic CPR to an harmonic (sine) CPR due to a finite t by relating the cutoff $-1/2 \ln t$ to the typical number of reflections before a scattering event occurs.

In summary, a disordered or poorly transmitted junction should lead to a small number of Andreev reflections before a scattering event occurs and should be universally sinusoidal. On the contrary, for a very ballistic junction with clean interfaces, the number of reflection-propagation is very large before any scattering event, and the CPR should be very anharmonic, i.e. sharp at π, both in the short and in the long junction.

2.3 Multiple channels

The case of M multiple channels can be generalized straightforwardly for the short junction limit, because one can identify one conduction channel in the normal metal with a definite Andreev energy level. If there is no diffusion, then the current-phase relation remains the same with a global multiplicative factor M.

For the long junction, there is however no such one to one relationship between Andreev levels and the transmission matrix eigenstates. In other words, the scattering matrix does depend on the energy. Other approaches makes use of the quasiclassical Green's functions formalism, or by performing exact numerical diagonalization of the Bogoliubov-de Gennes equations. The result is similar than the one stated in the one channel case : the presence of disorder leads to a loss of harmonic content in the CPR (Dubos et al., 2001), (Heikkilä, Särkkä & Wilhelm, 2002), (Hammer, Cuevas, Bergeret & Belzig, 2007).

For both the short diffusive and the long diffusive junction, one has

$$i(\varphi) = i_0 \sum_{m} a_m \sin(m\varphi) \tag{3.21}$$

with

$$a_m = \frac{3(-1)^m}{(2m+1)(2m-1)} \tag{3.22}$$

and

$$i_0 = \begin{cases} \dfrac{3.2\Delta}{eR_\mathrm{N}} & \text{(short)} \\ \dfrac{10.82E_\mathrm{T}}{eR_\mathrm{N}} & \text{(long)} \end{cases} \tag{3.23}$$

2.4 Prediction for Quantum Spin Hall systems

For the quantum spin hall case (QSH), there is a locking between the spin and the velocity along each edge. As a result

- transport should be ballistic if no time reversal symmetry breaking mechanism occur. Indeed, in this case one cannot flip the velocity without flipping the spin, which is forbidden in a chiral channel. Therefore the transport should be ballistic due to this protection.
- At the NS interface, for the same reason, the normal reflection is forbidden in the absence of time reversal symmetry breaking because it would flip the velocity without flipping the spin, while on the contrary Andreev reflection is favored as the reflected hole has an opposite spin given the s wave pairing symmetry of the superconducting order parameter.

In addition to these properties related to the motion of Andreev pairs across the junction, an other property is predicted for the Quantum Spin Hall insulator connected with superconducting electrodes (Beenakker et al., 2013). This prediction results from the fact the secular equation which admits two solutions associated with $\pm\phi/2$ are now located on two different edges. In the limit of a very wide sample, they do not couple and the levels truly cross at π : in other words the resulting CPR has the $\varphi/2$ dependence, that is to say it is 4π periodic instead of 2π periodic.

2.5 π junction and φ junction

I now focus on the consequence of spin orbit interaction on the propagation of ABS. For simplicity, I assume a Rashba spin-orbit interaction. Depending on the effective dimensionality of the system, spin-orbit interaction will lead to a splitting of the levels. In one dimension with parabolic band dispersion, no effect occurs. Indeed, in this case, the transverse component of the momentum k_y is negligible and one can rewrite the Rashba term as

$$H_\mathrm{SO} = k_\mathrm{x}\sigma_\mathrm{y} - k_\mathrm{y}\sigma_\mathrm{x} \simeq k_\mathrm{x}\sigma_\mathrm{y} \tag{3.24}$$

Therefore, the total hamiltonian commutes with σ_y, in other words the spin is a good quantum number. Consequently it has no evolution and the ABS are still spin degenerate.

However, this degeneracy is somewhat accidental. As soon as the dimensionality is not purely 1D, or that the band dispersion is not parabolic, the presence of spin-orbit coupling leads to a shift between the two Fermi velocities v^+ and v^- due to the spin degeneracy lifting. Interestingly, this is the case for a parabolic band dispersion with spin-orbit interaction in addition to a perpendicular and parallel magnetic field. Indeed, the hamiltonian of the system reads

$$\begin{aligned} \hat{H}_N &= \hat{H}_0 + \hat{H}_{\text{SO}} + \hat{H}_{\text{Z}} \\ &= \hat{\mathbf{p}}^2/2m + \alpha(\hat{\mathbf{p}} \times \hat{\sigma}) \cdot \mathbf{e_z} - g\mu_B \mathbf{H} \cdot \hat{\sigma} \\ &\equiv k^2/2m + \alpha(k_x\sigma_y) - h_\parallel \cdot \sigma_y - h_\perp \cdot \sigma_z \end{aligned} \tag{3.25}$$

where for simplicity I put here $\hbar = 1$, and define $h \equiv g\mu_{\text{B}}H$. The eigenenergies are

$$\epsilon_\pm = \epsilon_0(k) \pm \sqrt{h_\perp^2 + (\alpha k_x - h_\parallel)^2} \tag{3.26}$$

where $\pm$ denotes the two spin split bands and $\epsilon_0(k) \equiv k^2/2$. Thus, the velocities $v_\pm = \partial_k \epsilon|_\pm$ are given by

$$\begin{aligned} v_\pm &= k_\pm/m \pm \frac{\alpha(\alpha k_\pm - h_\parallel)}{\sqrt{h_\perp^2 + (\alpha k_\pm - h_\parallel)^2}} \\ &= k_\pm/m + \frac{\alpha(\alpha k_\pm - h_\parallel)}{\epsilon_F - k_\pm^2/2m} \end{aligned} \tag{3.27}$$

This shows that the presence of a parallel magnetic field $h_\parallel$ acts directly on the velocities. On the other hand, the effect of $h_\perp$ is to split the bands.

In the case of two dimensions, one cannot neglect k_y anymore. This is the case as soon as one allows more than one conduction channel, and in general, some band mixing will occur, leading to a non parabolic dispersion relation. As a result, the velocities are also shifted in this case.

The Andreev spectrum is directly affected by the velocity shift, as it leads to a shift of the propagative phase acquired by the ABS along their trajectories by an amount

$$\Delta\phi = \frac{2\epsilon_F L}{\hbar}(\frac{1}{v_+} - \frac{1}{v_-}) \tag{3.28}$$

However, although spin-orbit interaction alone can change the Andreev spectrum, it does not change the CPR (Dimitrova & Feigelman, 2006), if no magnetic field or disorder is present. One can understand this result by stating that the CPR cannot change if one does not break time reversal symmetry. One can view this result from the Andreev spectrum perspective by looking at the velocity of the spin up and spin down levels. As a result, the Andreev equation leads to different energy levels, that are effectively spin split.

Microscopically, the evolution of electrons from one interface to the other in presence of SOI implies a phase accumulation along closed trajectories. However, the phase accumulated by the holes compensates this phase by the exact same amount. In order to observe a net effect, one should create an imbalance between electrons and holes. In other words one should break time reversal symmetry (Buzdin, 2008).

This is the role played by a Zeeman field. Indeed, taking into account both effects, one sees that the total accumulated phase due to the spin does not vanish. As a result, the CPR is shifted by a constant φ_0.

In the QSH case, the CPR is very sensitive to spin orbit interaction that leads to a ballistic CPR even in presence of disorder, due the topological protection. Moreover, since each counterpropagating edge channel is associated to a definite spin, the effect of the Zeeman field $g\mu_B B$ at one edge is to shift the spin up towards positive energy and spin down towards negative energy. Then, summing the current of each levels results in a net phase shift. However, this phase shift is counterbalanced by the same amount at

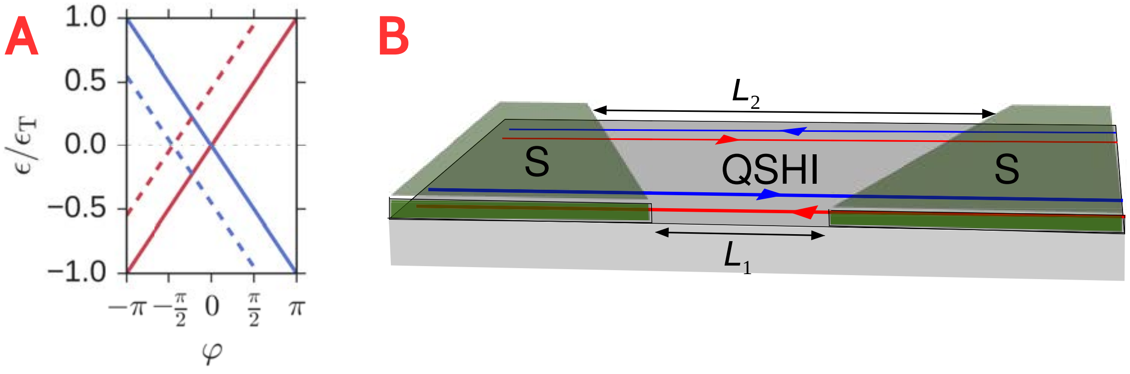

Figure 3.2: Anomalous Josephson effect in the QSH case. **A** : Phase dependent Andreev spectrum. Solid blue (red) line : branch of positive (resp. negative) current at zero Zeeman energy $E_Z = 0$. Dotted blue (red) line : branch of positive (resp. negative) current at zero Zeeman energy $E_Z \neq 0$. **B** : Schematics of the QSH connected asymmetrically to the superconducting electrodes. Taken from (Dolcini, Houzet, Meyer, 2015)

the other edge. Therefore, for a perfectly symmetrical sample, the phase shift should be compensated (Dolcini, Houzet & Meyer, 2015). This is no longer the case if there is an asymmetry between the length of the channels (fig 3.2).

3 Fabrication and measurement technique

One cannot phase bias a junction in order to measure the CPR in a two terminal geometry. In order to achieve this, one possibility is to enclose the junction in a loop geometry. In that case, a relation exists between the phase and the Aharonov-Bohm flux thread through the loop.

3.1 Asymetric SQUID technique

In a SQUID, the relation between the phase difference $\varphi_1 - \varphi_2$ across the two junctions is related to the Aharonov Bohm flux inside the loop thanks to the fluxoid quantization relation

$$\varphi_1 - \varphi_2 + 2\pi\frac{\phi_{\text{ext}}}{\phi_0} = 2n\pi \tag{3.29}$$

The critical current of the whole SQUID for a given ϕ_{ext} is given by the maximum of the function of one variable

$$i_c = \max|i_1(\varphi_1) + i_2(\varphi_2)| \tag{3.30}$$

If one makes the further assumption that the SQUID is asymetric, meaning that $i_1 \gg i_2$, then the phase φ_1 at the maximum of supercurrent will be constant to first order

$$\varphi_1 \simeq \varphi_1^0 \tag{3.31}$$

As a result, φ_2 is given by

$$\varphi_2 \simeq \varphi_1^0 + 2\pi\frac{\phi_{\text{ext}}}{\phi_0} \tag{3.32}$$

and is therefore a linear function of the magnetic field. Therefore, at first order in i_1/i_2, the measurement of the switching current of the whole SQUID will result in the superposition of a 0 order term (constant) given by critical current of the reference junction $i_2(\varphi_2^0)$ modulated by a 1st order term $i_1(\varphi_1^0 + 2\pi\phi_{\text{ext}}/\phi_0)$ which is nothing but the current phase relation of the junction.

3.2 Proof of principle using a W constriction as the reference junction

The critical current of Bi nanowire being in the range of few 10 nA to few 100 nA, it is therefore desirable to make a junction with critical current around 10 μA. If we were using an Al tunnel junction, then using the relation $eR_{\text{N}}I_{\text{C}} = \pi\Delta/2$, with $\Delta \simeq 160\,\mu$V for Al, that requires a shunt resistance of 20 Ω, that is only realizable in practice by making a junction of large area, which is not convienient in particular because it would not survive to high magnetic fields. Therefore, we have chosen to make the reference junction using a tungsten constriction. This has two advantages : the gap of W is larger, and the resistance can be made smaller than for the tunnel junction. Aiming $I_{\text{C}} \simeq 10\,\mu A$, the resistance of the constriction required is $R_{\text{N}} \simeq 120\,\Omega$.

The fabrication of the SQUID for the proof of principle experiment was made using an open Al loop closed on one side by a superconducting tunnel junction (fig 3.3). The other side is left open for growing the W constriction. Two other discontinuities in the loop are made in this design, in order to measure the resistance of different sections independently before the measurement at low temperature. They are closed by growing tungsten lines at the last step.

The fabrication of the W constriction is made in two steps, using a technique developed by Alik Kasumov. First, a W line is grown using the FIB. Second, two micro-manipulated metallic tips present inside the FIB chamber are brought to contact with the big pads connecting the two sides of the W line. Finally, the W line is etched while measuring the differential resistance using a lockin amplifier. Every etching step can be modelized by a reduction of the nanowire's thickness t by an amount τ. Therefore the resistance at every step is given by

$$R_n = R_{\text{C}} + \frac{\rho L}{w(t - n\tau)} \tag{3.33}$$

with ρ the resistivity of W, and w the width of the W line. The increase in resistivity is thus approximately given by

$$R_{n+1} - R_n \simeq \frac{\rho L}{S} \frac{\tau/t}{(1 - \tau n/t)^2} \tag{3.34}$$

Therefore, the resistivity increases non linearly with the index of the step, mimicking a divergence : the increase is small at the beginning, and becomes progressively very large. Of course, when the critical step where the W line is disconnected and the resistance is infinite is passed, the process has to be restarted over. A way to circumvent this is be to measure the conductivity instead of the resistivity. Furthermore any shift during the etching process will result in a smaller τ, or a recovering of the constriction by redeposition of tungsten and therefore an increasing of τ.

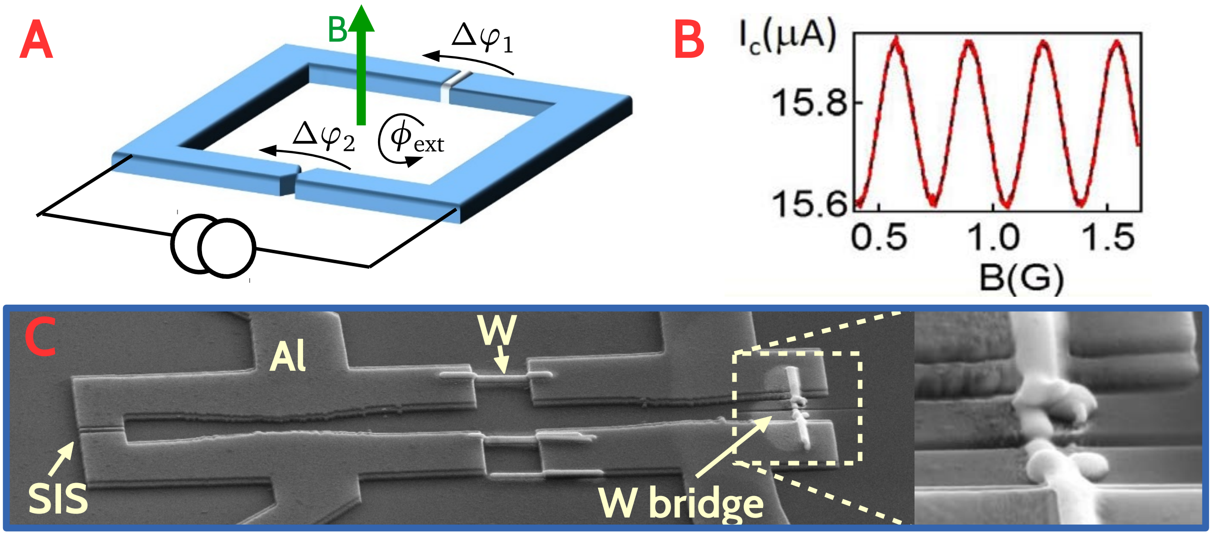

Figure 3.3: Proof of principle of the current phase relation measurement using an asymetric SQUID technique with a W constriction as the reference junction. **A** : Schematics of the asymetric squid. The superconducting tunnel junction is symbolized by the white junction and the W constriction is located opposite to it. **B** Critical current of the asymetric SQUID. Red : measurement after performing the β correction. Black dashed line : sinus function fit. **C** : SEM image of the measured SQUID. The long part of the SQUID is 20 microns long. Inset : Zoom of the W constriction.

3.3 Measurement technique

The switching current was measured using a counter technique (fig 3.4). A time dependent current source signal is produced using an arbitrary function generator (AFG) voltage source in serie with a polarization resistance R_{polar}. The signal is chosen to be a triangle of amplitude peak to peak V_{pp}, so that a bias current is swept linearly over over a period T. For practical reasons, this triangle is asymetric, the duration of the positive slope part of the signal divided by T being termed as the duty factor. Moreover, it is important that the current has a negative part to ensure the junction to return to the superconducting state, therefore offsetting the bias by a voltage V_{off} is important. The typical frequency for this signal can vary from few Hz to 200 Hz. The output voltage across the junction will therefore switch into the normal state, at a given time that corresponds to the current of the ramp. This time τ_{m} is defined modulo the period T, and is recorded in a counter so that it will be averaged over many such events. An extra offset time can be defined by setting a delay between the ramp and the counter, that is characterized by a phase φ.

One can relate the measured time to the current through

$$i_{\text{m}} = \frac{1}{R_{\text{polar}}}\left(V_{\text{off}} + \frac{V_{\text{pp}}}{\text{Duty}}\left(\frac{t_{\text{m}}}{T} + \frac{\varphi}{2\pi} - 1/2\right)\right) \tag{3.35}$$

4 Current phase relation of Bi nanowires based Josephson junctions

We decided to investigate the CPR of a Bi junction that was already characterized in a two terminal DC transport measurement, the data of which are shown at the end of

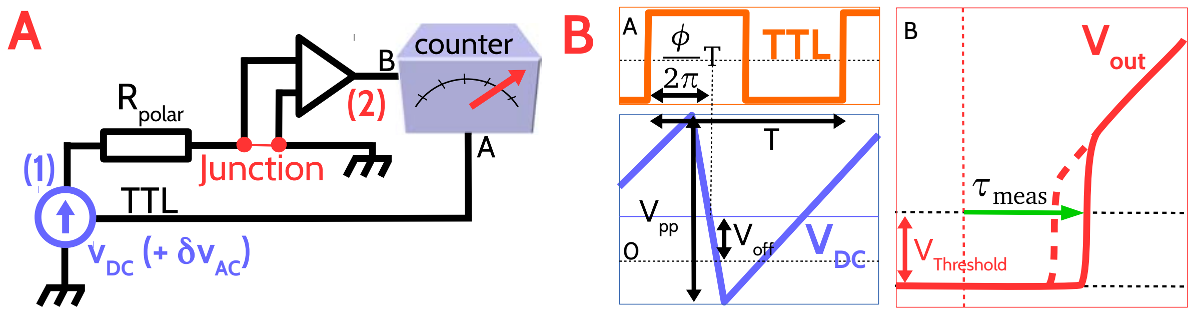

Figure 3.4: Principle of the measurement of the switching current using the counter technique. **A** : Electrical circuit diagram of the measurement setup. **B** : see main text.

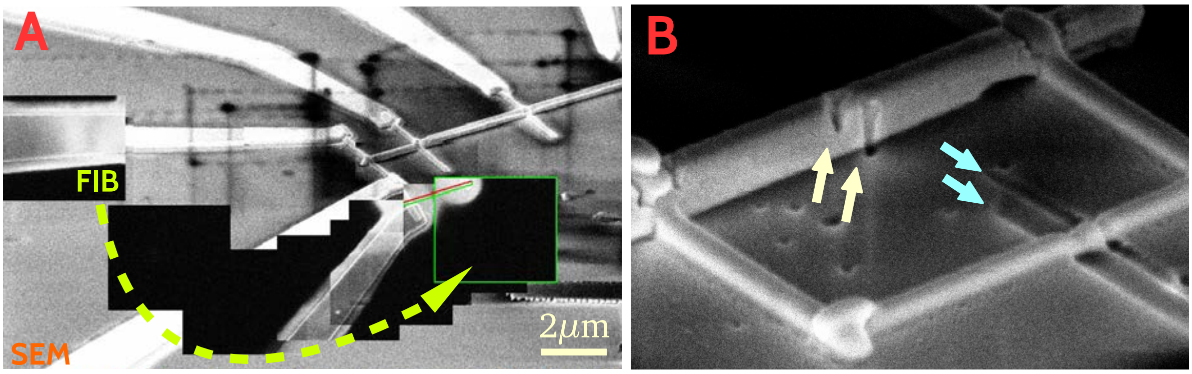

Figure 3.5: Fabrication of the asymetric SQUID using FIB. A: Dual imaging using both FIB and SEM. The FIB imaging is done in a reduced window, at coincidence between the two focal points of the SEM and the FIB. The magnification is less than 5k. The window is displaced in order to avoid exposing the nanowires to the Ga^+ ion beam. A W line is grown thereby shunting the nanowire. It is then etched in order to obtain a significant increase of the 2 wires resistances measured in situ. B : Two common errors using FIB that are fatal for the fabrication of a SQUID. White lines : hole in the nanowire caused by Ga ions due to excess of exposure at the reduced window's dump point (upper left of the window). Blue lines : shift of the beam while etching, due to either charging effects or a too long time taken during the procedure.

the previous chapter. The choice of this particular junction was made because of its distinctive feature of SQUID like oscillations at low magnetic fields, compatible with the existence of edge states in the system. We therefore directly built the SQUID on the DC W electrodes, without using an Al loop such as in the proof of principle experiment. This leads to a modification of the fabrication process that I will now detail.

4.1 Variation on the fabrication process

A W line was grown in parallel to the Bi nanowire. The tips were placed on the pads in order to measure the resistance (fig 3.5) of the whole circuit. We etched the W line about 20 times in the same conditions, and stopped when the increase in the resistance was sufficiently high. As a result, the increase in resistance was found to be equal to 90 Ω. The critical current of the reference junction was found to be equal to 83 μA and modulated by only 350 nA, compared to the 1.4 μA measured in the two wires configuration. The

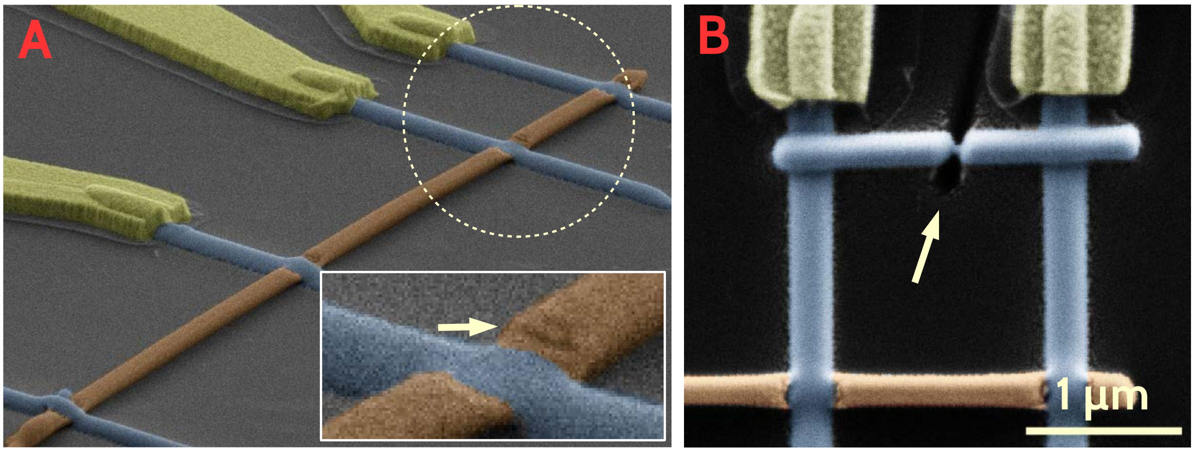

Figure 3.6: SEM image of the fabricated SQUID with Bi nanowire Josephson junction. **A** : SEM image of the nanowire before constructing the SQUID. White dashed circle : the selected section showing SQUID like oscillations. Inset : Zoom on the SEM image showing the damaged contact interface. **B** : Fabricated SQUID. The white arrow indicates the etching line.

reason of this decrease in the amplitude of the current of the Bi junction is understood by the modification of the contact resistance due to thermal cycling that was necessary for the fabrication of the SQUID. As a result, the SQUID made this way was very asymetric, making it challenging to measure. A variation on the traditional measurement technique was made in order to circumvent this issue.

4.2 Variation on the measurement technique

We added AC modulation of the current to the switching measurement process (fig 3.7). An AC voltage with small amplitude and with frequency of the order of few 10 kHz was added to the DC voltage. The output of the amplified differential signal was then demodulated at the same frequency and fed to an adjustable band pass filter. The output of the latter was used for the detection in the counter. The use of a lockin amplifier has two advantages. First, it gets rid of the large constant resistance in serie with the sample. Second, it increases the signal over noise ratio in the signal measured by the B port of the counter. A band pass filter is used to select the high resistance jump in the dvdi vs i curve, corresponding to the switching event. As a result, the detection threshold is done on a dark background (zero voltage).

4.3 CPR of Bi nanowires based Josephson junctions

The switching current data shows oscillations of amplitude $\Delta i = 350\text{nA}$ above the critical current of the constriction $I_\mathrm{C} \simeq 79\,\mu\mathrm{A}$. The SQUID dimensions are $L \times W = 1.4\,\mu\mathrm{m} \times 1.4\,\mu\mathrm{m}$, therefore the SQUID area is $1.96\,\mu\mathrm{m}^2$. The expected magnetic field period for the signal is thus 10.2 G, which matches the measured period 9.62 G within 6%.

The shape of the CPR is a very sharp sawtooth, which is indicative of the ballistic propagation of Andreev pairs with quasi perfect Andreev reflection.

Furthermore, the shape of the CPR is characteristic of the long junction. Using $v_\mathrm{F} = 6 \pm 2 \cdot 10^5\,\mathrm{m/s}$, one can estimate the coherence length in the ballistic limit $\xi = \hbar v_\mathrm{F}/\Delta = 318\,\mathrm{nm} \ll L$, which indeed indicates that the junction is long.

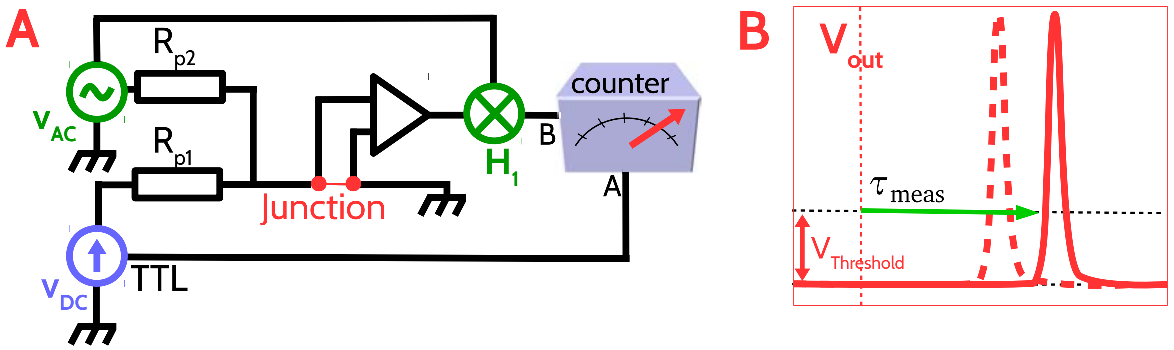

Figure 3.7: Principle of the measurement of the switching current using the counter technique with AC modulation. **A** : Electrical circuit diagram of the measurement setup. **B** : Signal at the output of the preamplifier. See main text for the details.

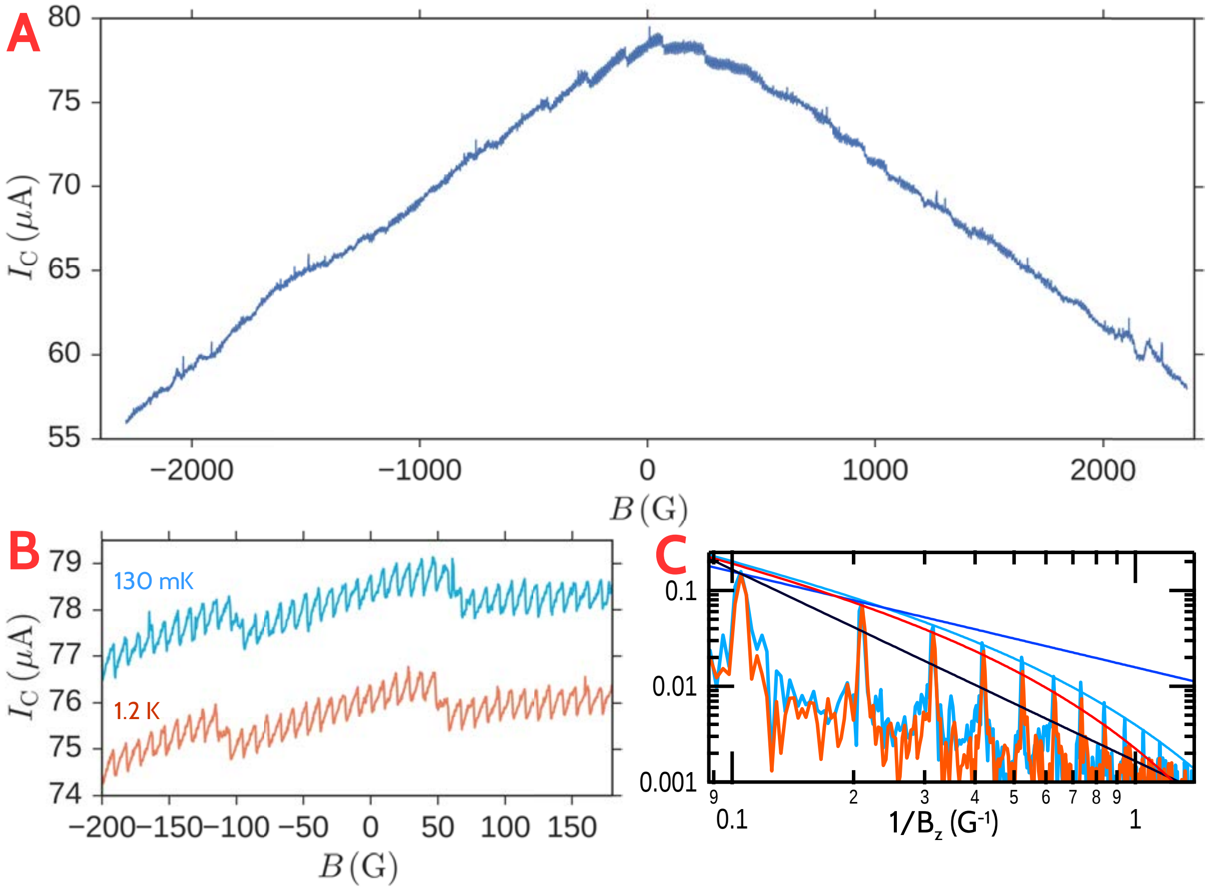

Figure 3.8: Switching current of the SQUID 1 as a function of the magnetic field. **A** Switching current of the SQUID 1 at 130 mK for magnetic fields up to 2400 G. **B** Zoom of the switching current at low field, revealing the sawtooth shaped current phase relation of the Bi nanowire based Josephson junction, for two temperatures. **C** Fourier transforms of the corresponding signals. The temperature dependence can be found in the higher harmonics.

4.4 β-correction

Before going further, I now show that the SQUID is not hysteretic. The CPR signal would have been difficult or impossible to extract otherwise. Indeed, if the amplitude of the current circulating around the loop gets too large, then the external applied flux may be screened inside the loop.

In SQUID-like systems, this effect can be accounted by a single parameter β termed the Stewart - McCumber parameter, which is defined as

$$\beta \equiv 2\pi \frac{\mathcal{L}_{\mathrm{tot}} I_{\mathrm{C}}}{\phi_0} \tag{3.36}$$

In order to evaluate β, one needs to estimate the inductance of the loop. The total length of the loop being $L_{\mathrm{tot}} = 5.1\,\mu\mathrm{m}$, the corresponding geometrical inductance is $\mu_0 L_{\mathrm{tot}} = 6.4{\cdot}10^{-12}\,\mathrm{H}$. It is important to correct this value by adding the kinetic inductance of FIB deposited W to it. Indeed, being a disordered superconductor, it's contribution outweighs that of the geometrical inductance alone. The kinetic inductance of a wire of section S is given by

$$\mathcal{L}_{\mathrm{K}} = \mu_0 L_{\mathrm{tot}} \frac{\lambda^2}{S} \tag{3.37}$$

where λ is the penetration length of the disordered superconductor.

For FIB deposited W wires, one has on one hand

$$\mathcal{L}_{\mathrm{geo}} = \mu_0 L \tag{3.38}$$

and on the other hand

$$\mathcal{L}_{\mathrm{K}} = \frac{1}{\pi} R_N \frac{\hbar}{\Delta} \tag{3.39}$$

Therefore,

$$\frac{\mathcal{L}_{\mathrm{K}}}{\mathcal{L}_{\mathrm{geo}}} = \frac{R_N h}{\mu_0 L \Delta} \tag{3.40}$$

which is a constant for a W line with constant thickness fabricated in the same conditions. For our case, $R/L \simeq 10.0 \cdot 10^7\,\Omega/\mathrm{m}$ at most and $\hbar/\Delta \simeq 0.53\mathrm{ps}$, therefore an upper estimate for this ratio is $\mathcal{L}_{\mathrm{K}}/\mathcal{L}_{\mathrm{geo}} = 13.4$. Therefore, the kinetic inductance can be estimated to be $L_{\mathrm{K}} \simeq 10 L_{\mathrm{geo}}$.

The corresponding correction due to the finite Stewart-McCumber parameter β is negligible in this case :

$$\begin{aligned}\beta &= 2\pi \frac{(L_{\mathrm{K}} + L_{\mathrm{geo}})}{\phi_0} I_{\mathrm{c}} \\ &= 0.092 \ll 1\end{aligned} \tag{3.41}$$

where the I_{c} to take in this formula is the current that screens the loop, which is $I_{\mathrm{c}} = 350\mathrm{nA}$ in our case.

4.5 Temperature dependence

The CPR of the main signal displays a very small variation between the temperatures 130 mK and 1.3 K, an observation that seems to disagree with the long junction behavior. If we look at the higher harmonics of the CPR (fig 3.8), we see a change of amplitude of the harmonics starting from the 5th harmonic. This small thermal rounding of the CPR can be used to evaluate the Josephson energy ϵ_{J} of the junction. One has (Bergeret, Virtanen, Ozaeta, Heikkilä & Cuevas, 2011)

$$\begin{aligned}\frac{i_n(T)}{i_n(0)} &= 1/\sinh\left(\frac{\pi n k_{\mathrm{B}} T}{\epsilon_{\mathrm{J}}}\right)\\ &\simeq \exp\left(-\frac{\pi n k_{\mathrm{B}} T}{\epsilon_{\mathrm{J}}}\right)\end{aligned} \tag{3.42}$$

in the asymptotic limit ($nT \to \infty$). In a long junction, ϵ_{J} is given by the Thouless energy $\epsilon_{\mathrm{T}} = 282\,\mu\mathrm{V} \simeq 6\,\mathrm{K}$, so that the decay should be $i_n(T)/i_n(0) \sim \mathrm{e}^{-n/4.8}$ at 1.3 K. This would imply that the amplitude of the 5th harmonic should be approximately one third between 1.3 K and 130 mK. We observe that this only happens around the 7th harmonic, meaning that we underestimated ϵ_{T}. More quantitatively, we measure a decay $\exp(-0.25n)$ at 1.3 K, so that $\epsilon_{\mathrm{J}}/\pi = 4\,\mathrm{K}$, and therefore $\epsilon_{\mathrm{J}} = 12\,\mathrm{K}$. This would correspond to $v_{\mathrm{F}} = 1.2 \cdot 10^6\,\mathrm{m/s}$.

4.6 Second channel

By optimizing the detection setup, which is done essentially by increasing the number of measurements on which the counter performs its average, one observes a small periodic signal which superimposes to the main signal with a different periodicity. The observed periodicity is 10% higher than the one of the main sawtooth signal. It matches the value of one flux quantum across the area of a greater SQUID that would be formed by the outer channel of the Bi nanowire. It also corresponds to the second channel whose existence was hinted by the two wires measurement described in the previous chapter.

The amplitude of the full signal is recovered as one adds an other sawtooth with amplitude 50nA. The reason for this mismatch between the values of the current for the two different channels could be related to the existence of a disordered region that was caused by etching with Ga ions during the FIB deposition procedure (inset of fig 3.6A).

The critical current of this second channel is completely suppressed at $T = 1.3\,\mathrm{K}$. This seems to be in agreement with a reduced effective gap with value $\Delta^* < 1.3\,\mathrm{K}$, and this second channel would therefore be in the short junction limit. An other way to say this is to describe this channel by a longer path, which is justified since the electrons have to go through a disordered region before being Andreev reflected (fig 3.6)

4.7 Number of channels

The amplitude of the measured supercurrent as well as its resilience up to high magnetic fields ($B_{\max} = 0.5\,\mathrm{T}$) are consistent with a small number of channels, each of them confined in an extremely narrow region in space (within less than 4 nm $= \frac{\phi_0}{B_{\mathrm{maxL}}}$). The maximum supercurrent through one ballistic channel is $I_1 = \frac{\pi\Delta}{\phi_0} \simeq 250\,\mathrm{nA}$ for a short junction (i.e. $L \ll \xi = \hbar v_{\mathrm{F}}/L \simeq 330 - 600\,\mathrm{nm}$), and $I_1 = ev_{\mathrm{F}}/L = 70 \pm 30\,\mathrm{nA}$ for a long junction ($L \gg \xi$). The critical current of the nanowire, given by the modulated current amplitude

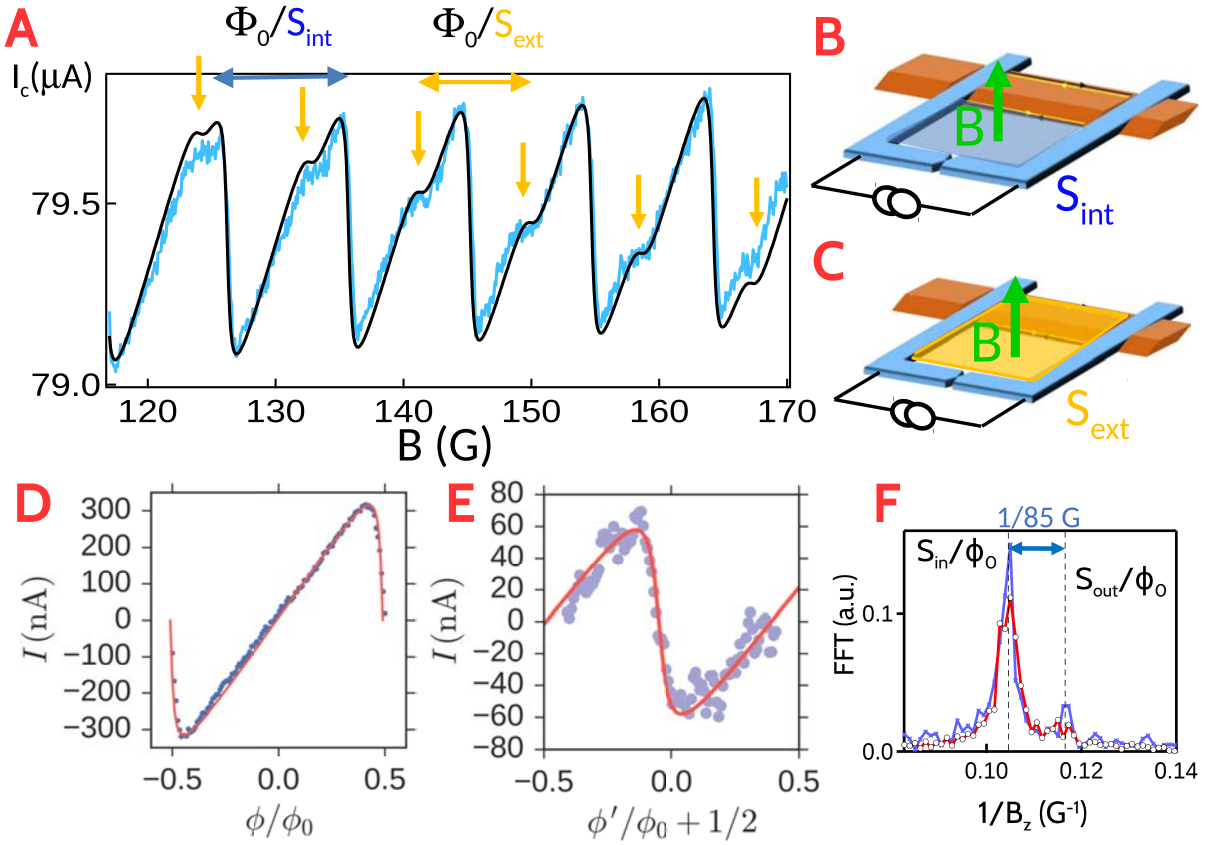

Figure 3.9: Second edge state revealed by performing the switching current measurement with a higher resolution. **A** : Blue curve : Critical current vs magnetic field. Black curve : sum of two sawtooth signals with different periods, corresponding to the different channels. The yellow arrows indicate the wiggle, corresponding to the second channel. **B** : Schematics of SQUID loop closed by the inner (bottom) channel, which is the shortest one. The area S_{int} is smaller, thus it has larger magnetic field period. **C** : SQUID loop closed by the outer (top) channel, which is the longest one, and corresponds to a larger area S_{ext}. The period is thus smaller. **D** : Main sawtooth signal. Blue dots : CPR signal averaged over 12 periods in order to remove the wiggle signal. The data is plotted against $\phi/\phi_0 = BS_{\text{int}}/\phi_0$. Red solid line : theoretical sawtooth signal with $t^2 = 0.92$ of amplitude 310 nA. **E** : Secondary sawtooth signal ("wiggle"). Blue dots : Raw signal subtracted from the averaged signal (D). The data is plotted against $1/2 + \phi'/\phi_0 \equiv 1/2 + BS_{\text{ext}}/\phi_0$. Red solid line : theoretical sawtooth signal with $t^2 = 0.7$ of amplitude 50 nA.

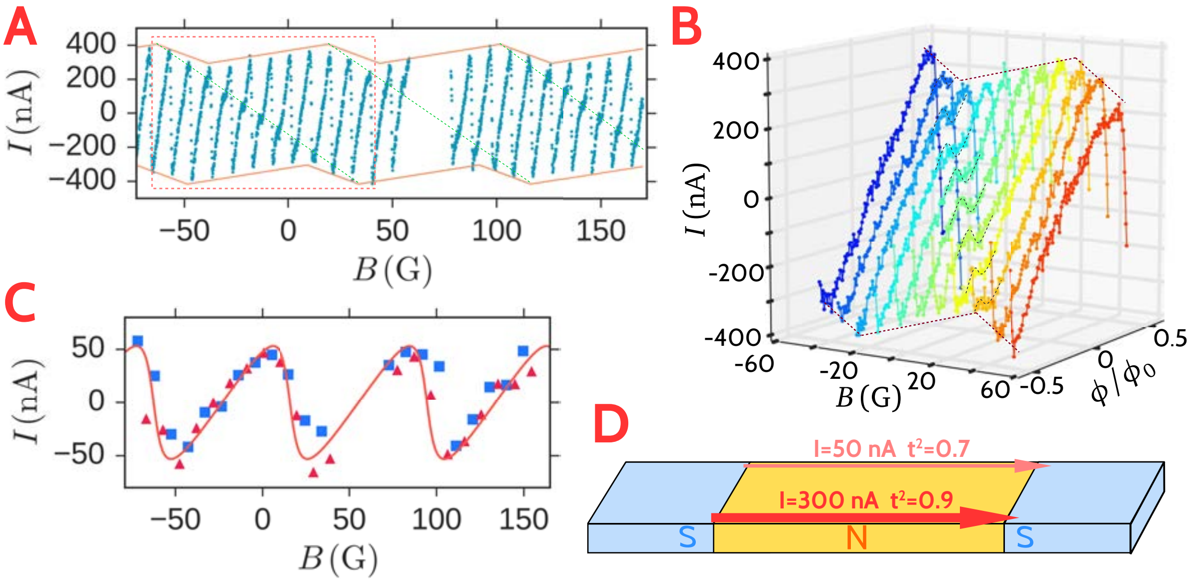

Figure 3.10: Envelope of the CPR showing that the signature of the second channel can be retrieved as an amplitude modulation of the largest channel. **A** : CPR at large scale. Blue dots : supercurrent filtered by a low frequency signal. The data between 58 G and 78 G are discarded. Orange solid line : guide to the eye for the maxima and minima of the CPR. Green dashed line : guide to the eye for the wiggle signal. **B** : CPR as a function of the magnetic field. **C** : Maxima (red triangles) and minima (blue squares) of the CPR as a function of the magnetic field. Orange line is the periodic sawtooth signal with period 80 G. **D** : Cartoon of the supercurrent carrying edge states along with their transmission and current.

of 400 nA (fig), thus implies that at most six perfectly transmitted channels carry the supercurrent. A reasonable assumption is that one path contains three to four quasi perfect channels, each with the same sawtooth-shaped CPR, and all situated at the inner edge of the wire, on the bottom (111) facet. They could be associated to the orbitals $p_\mathrm{x}, p_\mathrm{y}, p_\mathrm{z}$ of one topological edge state of Bi, as suggested by Murakami (Wada et al., 2011), or could also run along the edges of few parallel terraces at the facet edge.

On the other hand, the outer channel has $I_0 = 45\,\mathrm{nA}$. We can attribute this result to the prediction that the 3 conduction channels are not robust against disorder, but the topological protection ensures that one channel will remain ballistic, and thus contribute substantially to the current. Additionally, the current could be reduced further due to the reduction of the effective gap.

4.8 How ballistic are the channels

These sharp current phase relation can be fitted to evaluate the effective transmission of the channels. In order to achieve this, we use the formula

$$i(\varphi) = i_0 \sum_n \frac{(-1)^n}{n} t^{2n} \sin(n\varphi) \tag{3.43}$$

where t represents the average effective transmission. Note that this quantity is different from the finite transmission at the interface. The latter only reproduces the sharpness of the CPR while the second dictates the amplitude of the CPR. In this sense, the parameter t only concerns the propagation through the normal metal. We find $t = 0.9$ for the inner (bottom) channel, and $t = 0.7$ for the outer (top) channel.

4.9 Second SQUID

A second squid (BiW-SQUID2) was fabricated in order to confirm these results. The magnitude of the critical current found was $174\,\mu$A. The dimensions of the SQUID were $W \times L \simeq 1.5\,\mu m \times 1.6\,\mu m$ which corresponds to the measured period of 8 G.

The shape of the CPR is again a sawtooth, with a strikingly straight cusp at $\varphi = \pi$.

The amplitude of the current is 35 nA, which is similar to the current of the outer channel of the first SQUID. It would therefore correspond to one supercurrent carrying channel. The amplitude of the current being much smaller than in the previous SQUID and the dimensions being similar, the screening parameter β is completely negligible in this case ($\beta \simeq 10^{-3}$).

There was no signature of two path CPR, like in the previous SQUID. This could be due to two effects. First, the inner channel could be not connected to the SQUID this time, as can be hinted from the SEM image. Indeed, in the first SQUID, the Bi nanowire was etched and therefore more likely to connect both channels, whereas in the second SQUID, no etching was made which may result in a poorly connected bottom channel. Second and more likely, it could be due to the too high amplitude of the critical current of the reference junction combined with the small amplitude of the CPR, thereby limiting the sensitivity of the technique.

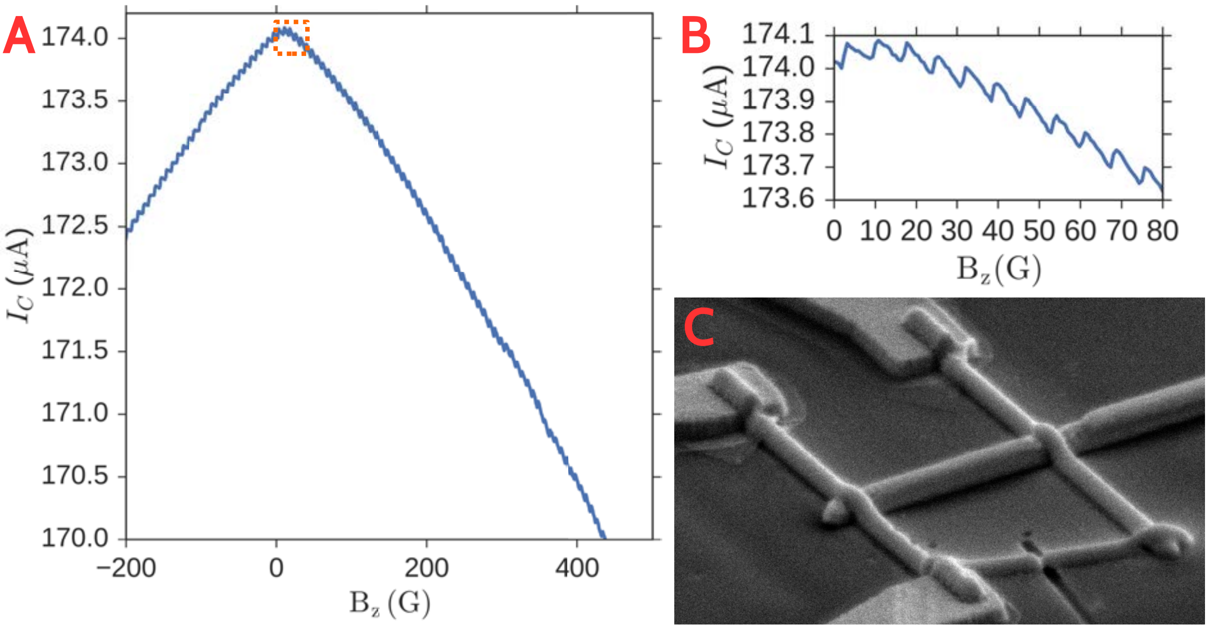

Figure 3.11: Switching current of the second SQUID (BiW-SQUID2) measured. **A** The CPR of the Bismuth nanowire based Josephson junction modulates the switching current of the SQUID over many periods. **B** Zoom on the signal at lower magnetic fields, showing a sawtooth like current-phase relation. **C** : SEM image of the BiW-SQUID2 device. The Bismuth junction is 1.4 μm long.

5 φ junction and π junctions behaviour

5.1 $0-\pi$ transition

The purely one dimensional nature of the Andreev bound states that carry the supercurrent across the nanowire implies that they are insensitive to orbital dephasing and therefore that the magnetic field acts primarily through the Zeeman effect. A Zeeman field can induce a crossing of the Andreev levels, turning an energy maximum into a minimum : this causes a sign change of the CPR, or equivalently a π shift of its phase. $0-\pi$ transitions are expected when dephasing by the magnetic field equals dephasing by the propagation time through the wire, i.e. when the Zeeman energy equals the Thouless energy, $g_{\text{eff}}\mu_{\mu B}B = \hbar\langle v_{\text{F}}\rangle/L$.

The characteristic field $B_{\text{x,y}} \sim 600\,\text{G}$, $B_{\text{z}} \sim 400\text{G}$ between 2 successive $0-\pi$ transitions seen in the CPR as a function of a magnetic field in the (111) plane, either perpendicular or parallel to the wire axis yields an effective g factor $g_{\text{eff}} \sim 30-100$, consistent with the high g factors of some bands in Bi. We note that penetration of vortices in the superconducting electrodes would also lead to phase jumps. This is however unlikely as no sign of hysteresis was found in our data. This realization of a $0-\pi$ transition induced by the Zeeman field is possible because the junction is long, contains few channels, and the g_{eff} are high enough that the transition occurs at a magnetic field below the superconducting electrodes' (relatively high) critical field.

5.2 φ junction effect

1. Linear correction

The main signature of the Zeeman induced φ junction is predicted to be a linear shift of the CPR as a function of the magnetic field : $\varphi \sim B_{\text{x,y}}$. However, a linear shift already arises from the misalignment of the two coils, that needs to be corrected. For example, a misalignment of $\theta = 1^{\text{o}}$ between the in plane coil and the out of plane coil would lead to a perpendicular magnetic field coming from the supposedly in plane coil of $\sin\theta \simeq \theta \simeq 1.7\%$ of the out of plane coil. Therefore, if $B_z = 1000G$, an uncertainty of $B_{\text{x,y}} = 10G$, that corresponds to one period of the oscillations. Moreover, the misalignment could be greater than 1^{o}.

For these reasons, we perform a linear correction in the B_{z}, $B_{\text{x,y}}$ plane, on the form

$$\begin{aligned} B_{\text{x,y}} &\to B_{\text{x,y}} + \alpha_{\text{x,y}} B_{\text{z}} \\ B_{\text{z}} &\to B_{\text{z}} \end{aligned} \tag{3.44}$$

2. Evaluation of the effect

   After having performed these correction, we observe a non linear shift of the CPR which is quadratic in the parallel magnetic field. The effect is stronger in the y direction than in the x direction (the direction of the nanowire), which agrees with the prediction of the theory.

6 Conclusion of this chapter

We showed that the CPR of Bi nanowire based Josephson Junction is that of a ballistic junction, with transparent interfaces. This result was confirmed independently in a second SQUID. In the first SQUID, we also detected a second ballistic channel, with a signal having a different periodicity, that was hinted in the 2 wire measurement of the critical current displayed in the previous chapter.

The strong spin orbit and g factor lead to the possibility to observe Zeeman induced band crossing under the form of $0 - \pi$ transitions and Zeeman induced φ junction effect. This g factor $g \simeq 30 - 100$ is significantly different from the $g \simeq 5 - 10$ obtained at high field in the two probes experiment. This is explained by the fact that the edge states may be different from low field to high field, as was explained in the previous chapter.

Another prediction for the Quantum Spin Hall is that the CPR is 4π periodic. However, poisoning processes at finite temperature will always give this 4π periodic signal a finite lifetime, resulting in a 2π periodic signal measured in DC. In order to probe this physics, we need to measure the CPR at finite frequency.

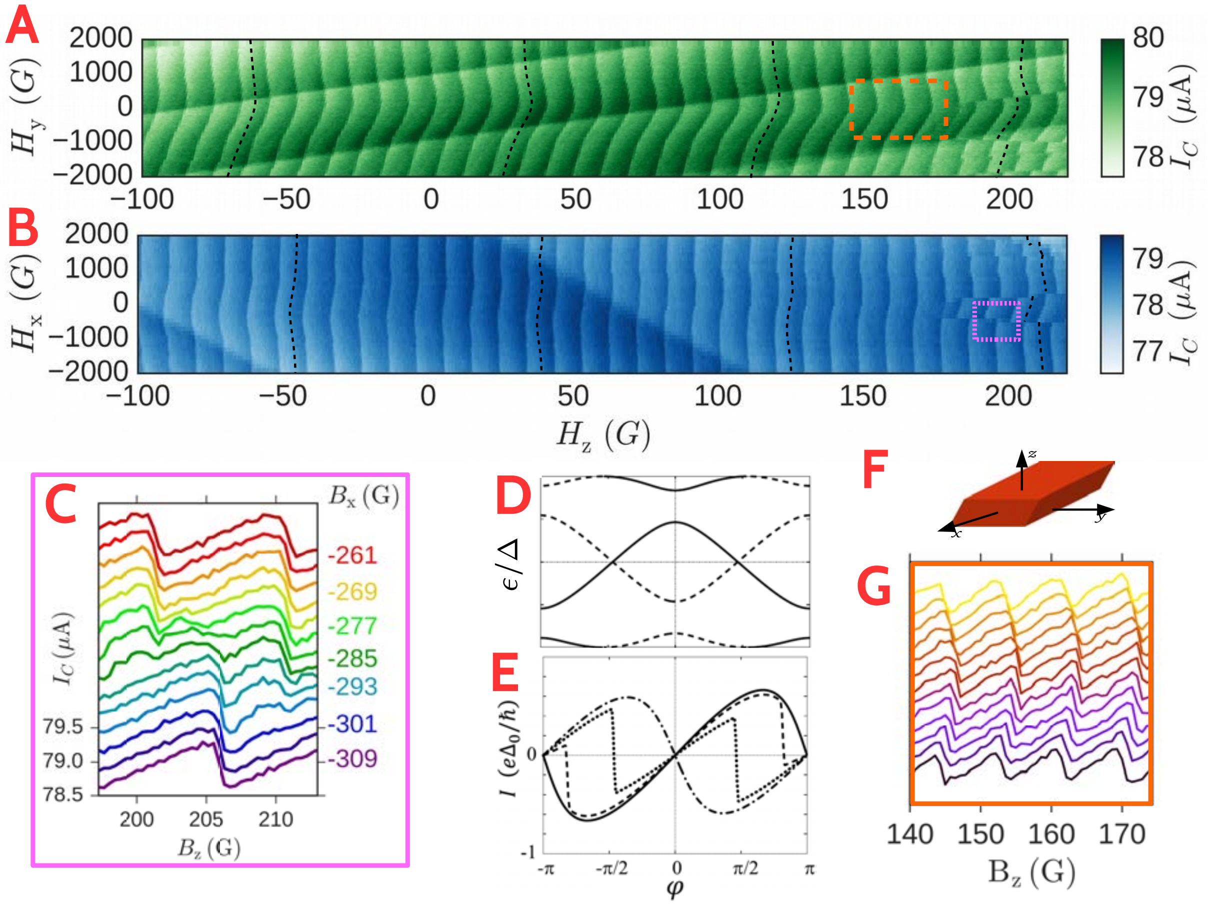

Figure 3.12: π junction and φ junction effects observed in parallel magnetic field. **A-B** Switching current as a function of the parallel magnetic field in the Y direction (A) and the X direction (B) as labeled in F. Black dotted lines : guide to the eye for the non linear φ junction behavior. Orange dotted line : region corresponding to the zoom displayed in G. Pink dotted line : region corresponding to the zoom displayed in C. **C** $0-\pi$ transition as a function of the parallel magnetic field for the region marked by a pink dotted line. **D-E** Andreev spectrum (D) and current-phase relation, as a function of the phase φ, in presence of a Zeeman magnetic field. In D, the plain and dotted line corresponds to two level resulting from the Zeeman field lifting of the spin-degeneracy. Taken from (Yokoyama, Eto and Nazarov, 2014). **F** Labeling of the directions with respect to the nanowires' axis. **G** CPR measured for different magnetic fields in the y direction, corresponding to the orange box in A.

Conclusion

In this thesis, I have investigated the superconducting proximity effect induced in monocristalline, micron long Bi and Ag nanowires with typical diameter $\varnothing \simeq 100\,\mathrm{nm}$.

The Ag nanowires display a conventional proximity effect typical of conventional multichannel, diffusive nanowires with a mean free path of the order of their diameter $l_{\mathrm{e}} \simeq 50\,\mathrm{nm}$. By varying the length of the junctions, we could follow the full transition from short to long SNS junction. Interestingly, we unambiguously found a systematic reduction of their $R_{\mathrm{N}}I_{\mathrm{C}}$ product by a factor 4 with respect to the theory. Moreover, a paradoxical increase of the critical current at low magnetic field was observed, and interpreted as a competition between heating and supression of the order parameter in the contact.

In contrast to the conventional proximity effect seen in the Ag nanowires, radically different results were obtained on monocristalline Bi nanowires. From the measurement of the resistance of segments of different lengths and Shubnikov de Haas oscillations, we first show that the normal transport is dominated by surface states, and that both bulk and surface states are diffusive with a mean free path of the order of the diameter $l_{\mathrm{e}} \simeq 200\,\mathrm{nm}$. Using superconducting proximity effect we revealed the existence of very few narrow ballistic channels that are undetectable in the normal state. The interference of the supercurrent carried by these channels lead to strikingly pure and robust SQUID-like oscillations up to high field (several T). The period extracted from the two path interference pattern correspond to one flux quantum across the area of the nanowires, indicating that the paths are situated at opposite edges of the wires. In addition to this orbital effect, a Zeeman effect (enhanced by the high g factors of the carriers) caused an amplitude modulation of the supercurrent with a Tesla range period.

We investigated further these supercurrent carrying edge channels by measuring the current phase relation of an already characterized Bi based Josephson junction, purposely realized in Bi nanowire with toplogical (111) facets. From the measured sawtooth shaped signal, we could unambiguously prove that these channels are ballistic and in the long junction regime. Besides, from the beating of this main signal, a second ballistic channel was found with a different period, demonstrating that this second channel is located on a diametrically opposite edge. The ballistic character (over a length $L > 1\,\mu\mathrm{m}$) suggest a topological protection of these states. Additionally, the high transmission extracted from these measurements suggests a nearly perfect Andreev reflection, as predicted for a chiral quantum spin Hall edge state. These results are in agreement with our tight binding simulations of Bi nanowires with rhombic section and (111) surface, that find two diametrically opposite paths along which the density of states is concentrated, and demonstrates spin-momentum locking.

In addition to those results obtained with high H_{C} focused ion beam induced tungsten superconducting contacts, we have also observed a two path interference pattern using different superconducting contacts made of BiPd. This result came as a surprise since they were obtained from pure sputtered Pd.

The next step is to perform the measurement of the dynamical response of the phase biased Bi based Josephson junction. This could uniquely uncover the topological protection suggested by the previous experiments. Indeed, as was also revealed by numerical simulations during this thesis, the AC susceptibility can exquisitely distinguish between avoided and topologically protected crossings. For this purpose, a test measurement has been realized on a Au based SNS junction at low temperatures and high frequency, with increased sensitivity by using a cryogenic RF amplifier. The insertion of the already measured Bi based SQUID in a superconducting resonator was successfully realized and should be measured soon.

Besides these measurements of supercurrents carried by edge states, other investigations of the quantum spin hall phase of Bi in the normal state could be imagined. For example, detecting the magnetic moment of a few bilayers-thick crystal should reveal large orbital currents that exist thanks to the protected edge states of Bi (111). One could also directly probe the Aharonov Bohm oscillations of the resistance, resulting from normal interferences of the edge states.

References

Abrahams, E., Anderson, P. W., Licciardello, D. C. & Ramakrishnan, T. V. (1979, March). Scaling Theory of Localization: Absence of Quantum Diffusion in Two Dimensions. *Physical Review Letters*, *42*(10), 673–676. Retrieved 2016-10-16, from `http://link.aps.org/doi/10.1103/PhysRevLett.42.673` doi: 10.1103/PhysRevLett.42.673

Abrikosov, A. A. (1969). Galvanomagnetic Phenomena in Metals in the Quantum Limit. *Soviet Journal of Experimental and Theoretical Physics*, *29*, 746. Retrieved 2016-11-22, from `http://adsabs.harvard.edu/abs/1969JETP...29..746A`

Akkermans, E. & Montambaux, G. (2007). Mesoscopic physics of electrons and photons. *EDP Sciences*. Retrieved from `http://dx.doi.org/10.1017/cbo9780511618833` doi: 10.1017/cbo9780511618833

Albrecht, S. M., Higginbotham, A. P., Madsen, M., Kuemmeth, F., Jespersen, T. S., Nygard, J., … Marcus, C. M. (2016, March). Exponential protection of zero modes in Majorana islands. *Nature*, *531*(7593), 206–209. Retrieved 2017-02-20, from `http://www.nature.com/nature/journal/v531/n7593/abs/nature17162.html` doi: 10.1038/nature17162

Alcántara Ortigoza, M., Sklyadneva, I. Y., Heid, R., Chulkov, E. V., Rahman, T. S., Bohnen, K.-P. & Echenique, P. M. (2014, November). \textit{Ab initio} lattice dynamics and electron-phonon coupling of Bi(111). *Physical Review B*, *90*(19), 195438. Retrieved 2016-11-10, from `http://link.aps.org/doi/10.1103/PhysRevB.90.195438` doi: 10.1103/PhysRevB.90.195438

Altimiras, C., Portier, F. & Joyez, P. (2016, July). Interacting Electrodynamics of Short Coherent Conductors in Quantum Circuits. *Physical Review X*, *6*(3), 031002. Retrieved 2017-02-06, from `http://link.aps.org/doi/10.1103/PhysRevX.6.031002` doi: 10.1103/PhysRevX.6.031002

Anderson, P. W. (1959, September). Theory of dirty superconductors. *Journal of Physics and Chemistry of Solids*, *11*(1), 26–30. Retrieved 2016-11-10, from `http://www.sciencedirect.com/science/article/pii/0022369759900368` doi: 10.1016/0022-3697(59)90036-8

Anderson, P. W. & Rowell, J. M. (1963, Mar). Probable observation of the josephson superconducting tunneling effect. *Phys. Rev. Lett.*, *10*, 230–232. Retrieved from `http://link.aps.org/doi/10.1103/PhysRevLett.10.230` doi: 10.1103/PhysRevLett.10.230

Ashcroft, N. W. & Mermin, N. D. (1976). *Solid state physics.* Saunders College.

Ast, C. R., Henk, J., Ernst, A., Moreschini, L., Falub, M. C., Pacilé, D., … Grioni, M. (2007, May). Giant Spin Splitting through Surface Alloying. *Physical Review Letters*, *98*(18), 186807. Retrieved 2016-11-04, from `http://link.aps.org/doi/10.1103/PhysRevLett.98.186807` doi: 10.1103/PhysRevLett.98.186807

Baring, L. A., Silva, R. R. d. & Kopelevich, Y. (2011, October). Local and global superconductivity in bismuth. *Low Temperature Physics*, *37*(10), 889–892. Retrieved 2016-11-10, from http://scitation.aip.org/content/aip/journal/ltp/37/10/10.1063/1.3671591 doi: 10.1063/1.3671591

Basset, J. (2011). *High frequency quantum noise of mesoscopic systems and current-phase relation of hybrid junctions.*

Beenakker, C. W. J., Pikulin, D. I., Hyart, T., Schomerus, H. & Dahlhaus, J. P. (2013, January). Fermion-parity anomaly of the critical supercurrent in the quantum spin-Hall effect. *Physical Review Letters*, *110*(1). Retrieved 2017-02-06, from http://arxiv.org/abs/1210.5412 (arXiv: 1210.5412) doi: 10.1103/PhysRevLett.110.017003

Bergeret, F. S., Virtanen, P., Ozaeta, A., Heikkilä, T. T. & Cuevas, J. C. (2011, August). Supercurrent and Andreev bound state dynamics in superconducting quantum point contacts under microwave irradiation. *Physical Review B*, *84*(5). Retrieved 2017-02-06, from http://arxiv.org/abs/1105.1016 (arXiv: 1105.1016) doi: 10.1103/PhysRevB.84.054504

Bert, J. A., Nowack, K. C., Kalisky, B., Noad, H., Kirtley, J. R., Bell, C., ... Moler, K. A. (2012, August). Gate-tuned superfluid density at the superconducting LaAlO${}_{3}$/SrTiO${}_{3}$ interface. *Physical Review B*, *86*(6), 060503. Retrieved 2016-11-10, from http://link.aps.org/doi/10.1103/PhysRevB.86.060503 doi: 10.1103/PhysRevB.86.060503

Black, W. C. (1968, July). Critical-Field Measurement of Superconducting Tungsten as Related to the Cerium-Magnesium-Nitrate Temperature Scale. *Physical Review Letters*, *21*(1), 28–31. Retrieved 2016-11-28, from http://link.aps.org/doi/10.1103/PhysRevLett.21.28 doi: 10.1103/PhysRevLett.21.28

Bocquillon, E., Deacon, R. S., Wiedenmann, J., Leubner, P., Klapwijk, T. M., Brüne, C., ... Molenkamp, L. W. (2016, August). Gapless Andreev bound states in the quantum spin Hall insulator HgTe. *Nature Nanotechnology*, *12*(2), 137–143. Retrieved 2017-02-20, from http://arxiv.org/abs/1601.08055 (arXiv: 1601.08055) doi: 10.1038/nnano.2016.159

Boukai, A. I., Bunimovich, Y., Tahir-Kheli, J., Yu, J.-K., Goddard Iii, W. A. & Heath, J. R. (2008, January). Silicon nanowires as efficient thermoelectric materials. *Nature*, *451*(7175), 168–171. Retrieved 2016-11-17, from http://www.nature.com/nature/journal/v451/n7175/full/nature06458.html#B6 doi: 10.1038/nature06458

Bretheau, L. (2013). *Localized excitations in superconducting atomic contacts: probing the andreev doublet.*

Buckel, W. & Hilsch, R. (1954, April). Einfluß der Kondensation bei tiefen Temperaturen auf den elektrischen Widerstand und die Supraleitung für verschiedene Metalle. *Zeitschrift für Physik*, *138*(2), 109–120. Retrieved 2016-11-09, from http://link.springer.com/article/10.1007/BF01337903 doi: 10.1007/BF01337903

Bustarret, E., Marcenat, C., Achatz, P., Kačmarčik, J., Lévy, F., Huxley, A., ... Boulmer, J. (2006, November). Superconductivity in doped cubic silicon. *Nature*, *444*(7118), 465–468. Retrieved 2016-11-10, from http://www.nature.com/nature/journal/v444/n7118/abs/nature05340.html doi: 10.1038/nature05340

Buzdin, A. (2008, September). Direct coupling between magnetism and superconducting current in Josephson Phi junction. *Physical Review Letters*, *101*(10). Retrieved 2017-02-06, from http://arxiv.org/abs/0808.0299 (arXiv: 0808.0299) doi: 10.1103/PhysRevLett.101.107005

Chauvin, M. (2005). *The Josephson Effect in Atomic Contacts* (phdthesis, Université Pierre et Marie Curie - Paris VI). Retrieved 2016-11-24, from https://tel.archives-ouvertes.fr/tel-00107465/document

Chen, J. T., Chen, T. T., Leslie, J. D. & Smith, H. J. T. (1967, November). Strong-coupling superconductivity in amorphous bismuth. *Physics Letters A*, *25*(9), 679–680. Retrieved 2016-11-10, from http://www.sciencedirect.com/science/article/pii/0375960167904719 doi: 10.1016/0375-9601(67)90471-9

Chiodi, F. (2010). *Dynamical effects in superconductor/normal metal/superconductor long josephson junctions.*

Chiodi, F., Ferrier, M., Guéron, S., Cuevas, J. C., Montambaux, G., Fortuna, F., … Bouchiat, H. (2012, August). Geometry-related magnetic interference patterns in long SNS Josephson junctions. *Physical Review B*, *86*(6). Retrieved 2017-02-21, from http://arxiv.org/abs/1201.3509 (arXiv: 1201.3509) doi: 10.1103/PhysRevB.86.064510

Claude Cohen-Tannoudji, B. D. e. F. L. (1973). *Mécanique quantique.* Hermann.

Coleridge, P. T., Stoner, R. & Fletcher, R. (1989, January). Low-field transport coefficients in GaAs/${\mathrm{Ga}}_{1\mathrm{-}\mathrm{x}}$${\mathrm{Al}}_{\mathrm{x}}$As heterostructures. *Physical Review B*, *39*(2), 1120–1124. Retrieved 2016-10-28, from http://link.aps.org/doi/10.1103/PhysRevB.39.1120 doi: 10.1103/PhysRevB.39.1120

Collaudin, A. (2014). *Tenseur de mobilité et magnétothermoélectricité anisotrope de bismuth.* Paris 6. Retrieved 2016-11-21, from http://www.theses.fr/2014PA066630

Cuevas, J. C. & Bergeret, F. S. (2007, November). Magnetic Interference Patterns and Vortices in Diffusive SNS Junctions. *Physical Review Letters*, *99*(21), 217002. Retrieved 2017-02-20, from http://link.aps.org/doi/10.1103/PhysRevLett.99.217002 doi: 10.1103/PhysRevLett.99.217002

Dassonneville, B. (2013). *Dynamics of andreev states in a normal metal - superconductor ring: Supercurrent fluctuations and spectroscopy of the minigap.*

Delagrange, R. (2016). *Josephson effect and high frequency emission in a carbon nanotube in the kondo regime.*

Dimitrova, O. V. & Feigelman, M. V. (2006, April). Two-dimensional S-N-S junction with Rashba spin-orbit coupling. *Journal of Experimental and Theoretical Physics*, *102*(4), 652–660. Retrieved 2017-02-06, from http://link.springer.com/article/10.1134/S1063776106040157 doi: 10.1134/S1063776106040157

Dolcini, F., Houzet, M. & Meyer, J. S. (2015, July). Topological Josephson ${\ensuremath{\phi}}_{0}$ junctions. *Physical Review B*, *92*(3), 035428. Retrieved 2017-02-06, from http://link.aps.org/doi/10.1103/PhysRevB.92.035428 doi: 10.1103/PhysRevB.92.035428

Drozdov, I. K., Alexandradinata, A., Jeon, S., Nadj-Perge, S., Ji, H., Cava, R. J., … Yazdani, A. (2014, September). One-dimensional topological edge states of bismuth bilayers. *Nature Physics*, *10*(9), 664–669. Retrieved 2017-02-09, from http://www.nature.com/nphys/journal/v10/n9/abs/nphys3048.html doi: 10.1038/nphys3048

Dubos, P., Courtois, H., Pannetier, B., Wilhelm, F. K., Zaikin, A. D. & Schön, G. (2001, January). Josephson critical current in a long mesoscopic S-N-S junction. *Physical Review B*, *63*(6), 064502. Retrieved 2017-02-20, from http://link.aps.org/doi/10.1103/PhysRevB.63.064502 doi: 10.1103/PhysRevB.63.064502

Édel'man, V. S. (1977). Properties of electrons in bismuth. *Soviet Physics Uspekhi*, *20*(10), 819. Retrieved 2016-11-21, from http://iopscience

.iop.org/article/10.1070/PU1977v020n10ABEH005467/meta doi: 10.1070/PU1977v020n10ABEH005467

Edwards, E. R. J., Ulrichs, H., Demidov, V. E., Demokritov, S. O. & Urazhdin, S. (2012, October). Parametric excitation of magnetization oscillations controlled by pure spin current. *Physical Review B*, *86*(13), 134420. Retrieved 2016-11-18, from http://link.aps.org/doi/10.1103/PhysRevB.86.134420 doi: 10.1103/PhysRevB.86.134420

Ekimov, E. A., Sidorov, V. A., Bauer, E. D., Mel'nik, N. N., Curro, N. J., Thompson, J. D. & Stishov, S. M. (2004, April). Superconductivity in diamond. *Nature*, *428*(6982), 542–545. Retrieved 2016-11-10, from http://www.nature.com/nature/journal/v428/n6982/full/nature02449.html doi: 10.1038/nature02449

Esaki, L. & Stiles, P. J. (1965, August). New Phenomenon in Semimetals and Semiconductors. *Physical Review Letters*, *15*(8), 377–377. Retrieved 2016-11-10, from http://link.aps.org/doi/10.1103/PhysRevLett.15.377 doi: 10.1103/PhysRevLett.15.377

Feldman, B. E., Randeria, M. T., Gyenis, A., Wu, F., Ji, H., Cava, R. J., ... Yazdani, A. (2016, October). Observation of a nematic quantum Hall liquid on the surface of bismuth. *Science*, *354*(6310), 316–321. Retrieved 2016-11-17, from http://science.sciencemag.org/content/354/6310/316 doi: 10.1126/science.aag1715

Fevrier, P. (2017). *Étude des fluctuations quantiques du courant aux fréquences optiques dans une jonction tunnel.*

Fominov, Y. V. & Feigel'man, M. V. (2001, February). Superconductive properties of thin dirty SN bilayers. *Physical Review B*, *63*(9). Retrieved 2016-11-12, from http://arxiv.org/abs/cond-mat/0008038 (arXiv: cond-mat/0008038) doi: 10.1103/PhysRevB.63.094518

Fu, L. & Kane, C. L. (2009, April). Josephson Current and Noise at a Superconductor-Quantum Spin Hall Insulator-Superconductor Junction. *Physical Review B*, *79*(16). Retrieved 2017-02-09, from http://arxiv.org/abs/0804.4469 (arXiv: 0804.4469) doi: 10.1103/PhysRevB.79.161408

Fuchs, J. N., Piechon, F., Goerbig, M. O. & Montambaux, G. (2010, October). Topological Berry phase and semiclassical quantization of cyclotron orbits for two dimensional electrons in coupled band models. *The European Physical Journal B*, *77*(3), 351–362. Retrieved 2016-10-27, from http://arxiv.org/abs/1006.5632 (arXiv: 1006.5632) doi: 10.1140/epjb/e2010-00259-2

Fukuyama, H. & Kubo, R. (1970, March). Interband Effects on Magnetic Susceptibility. II. Diamagnetism of Bismuth. *Journal of the Physical Society of Japan*, *28*(3), 570–581. Retrieved 2017-01-20, from http://journals.jps.jp/doi/abs/10.1143/JPSJ.28.570 doi: 10.1143/JPSJ.28.570

Fuseya, Y., Ogata, M. & Fukuyama, H. (2015, January). Transport Properties and Diamagnetism of Dirac Electrons in Bismuth. *Journal of the Physical Society of Japan*, *84*(1), 012001. Retrieved 2016-11-07, from http://arxiv.org/abs/1407.2179 (arXiv: 1407.2179) doi: 10.7566/JPSJ.84.012001

Fuseya, Y., Zhu, Z., Fauqué, B., Kang, W., Lenoir, B. & Behnia, K. (2015, November). Origin of the large anisotropic g-factor of holes in bismuth. *Physical Review Letters*, *115*(21). Retrieved 2016-11-16, from http://arxiv.org/abs/1507.05996 (arXiv: 1507.05996) doi: 10.1103/PhysRevLett.115.216401

Geim, A. K. & Grigorieva, I. V. (2013, July). Van der Waals heterostructures. *Nature*, *499*(7459), 419–425. Retrieved 2017-02-07, from http://www.nature.com/nature/

journal/v499/n7459/full/nature12385.html doi: 10.1038/nature12385

Gitsu, D., Konopko, L., Nikolaeva, A. & Huber, T. E. (2005, March). Pressure-dependent thermopower of individual Bi nanowires. *Applied Physics Letters*, *86*(10), 102105. Retrieved 2016-11-11, from http://scitation.aip.org/content/aip/journal/apl/86/10/10.1063/1.1873045 doi: 10.1063/1.1873045

Goerbig, M. O. (2009, September). Quantum Hall Effects. *arXiv:0909.1998 [cond-mat]*. Retrieved 2016-10-27, from http://arxiv.org/abs/0909.1998 (arXiv: 0909.1998)

Hammer, J. C., Cuevas, J. C., Bergeret, F. S. & Belzig, W. (2007, August). Density of states and supercurrent in diffusive SNS junctions: role of nonideal interfaces and spin-flip scattering. *Physical Review B*, *76*(6). Retrieved 2017-02-20, from http://arxiv.org/abs/0704.2358 (arXiv: 0704.2358) doi: 10.1103/PhysRevB.76.064514

Hasan, M. Z. & Kane, C. L. (2010, November). \textit{Colloquium} : Topological insulators. *Reviews of Modern Physics*, *82*(4), 3045–3067. Retrieved 2017-01-09, from http://link.aps.org/doi/10.1103/RevModPhys.82.3045 doi: 10.1103/RevModPhys.82.3045

Heikkilä, T. T., Särkkä, J. & Wilhelm, F. K. (2002, November). Supercurrent-carrying density of states in diffusive mesoscopic Josephson weak links. *Physical Review B*, *66*(18), 184513. Retrieved 2017-02-20, from http://link.aps.org/doi/10.1103/PhysRevB.66.184513 doi: 10.1103/PhysRevB.66.184513

Heremans, J. & Thrush, C. M. (1999, May). Thermoelectric power of bismuth nanowires. *Physical Review B*, *59*(19), 12579–12583. Retrieved 2016-11-09, from http://link.aps.org/doi/10.1103/PhysRevB.59.12579 doi: 10.1103/PhysRevB.59.12579

Hirahara, T., Miyamoto, K., Matsuda, I., Kadono, T., Kimura, A., Nagao, T., … Hasegawa, S. (2007, October). Direct observation of spin splitting in bismuth surface states. *Physical Review B*, *76*(15), 153305. Retrieved 2016-11-08, from http://link.aps.org/doi/10.1103/PhysRevB.76.153305 doi: 10.1103/PhysRevB.76.153305

Hofmann, P. (2006). The surfaces of bismuth: Structural and electronic properties. *Progress in Surface Science*, *81*(5), 191–245. Retrieved 2016-11-08, from http://www.sciencedirect.com/science/article/pii/S0079681606000232 doi: 10.1016/j.progsurf.2006.03.001

Huang, C. C. & Fung, K. Z. (2006, September). Effect of the surface configuration on the oxidation of bismuth nanowire. *Materials Research Bulletin*, *41*(9), 1604–1611. Retrieved 2016-11-16, from http://www.sciencedirect.com/science/article/pii/S0025540806000845 doi: 10.1016/j.materresbull.2006.02.037

Iftikhar, Z. (2017). *Many-body physics in few-channel quantum circuits (title to be confirmed)*.

Imry, Y. (2002). *Introduction to Mesoscopic Physics*. Oxford University Press. (Google-Books-ID: ZyjW37iGhaQC)

Johnson, R. C., Nieskoski, M. D., Disseler, S. M., Huber, T. E. & Graf, M. J. (2013, February). Superconductivity of Bi Confined in an Opal Host. *Journal of Low Temperature Physics*, *170*(3-4), 205–215. Retrieved 2016-11-10, from http://arxiv.org/abs/1108.5762 (arXiv: 1108.5762) doi: 10.1007/s10909-012-0768-3

Kane, C. L. & Mele, E. J. (2005, November). Quantum Spin Hall Effect in Graphene. *Physical Review Letters*, *95*(22). Retrieved 2017-01-10, from http://arxiv.org/abs/cond-mat/0411737 (arXiv: cond-mat/0411737) doi: 10.1103/PhysRevLett.95.226801

Kapitza, P. (1929, March). The Change of Electrical Conductivity in Strong Magnetic Fields. Part I. Experimental Results. *Proceedings of the Royal Society of London*

A: Mathematical, Physical and Engineering Sciences, *123*(791), 292–341. Retrieved 2016-11-22, from http://rspa.royalsocietypublishing.org/content/123/791/292 doi: 10.1098/rspa.1929.0072

Kasumov, A. (2016).
personal communication.

Kato, Y. K., Myers, R. C., Gossard, A. C. & Awschalom, D. D. (2004, December). Observation of the Spin Hall Effect in Semiconductors. *Science*, *306*(5703), 1910–1913. Retrieved 2016-11-18, from http://science.sciencemag.org/content/306/5703/1910 doi: 10.1126/science.1105514

Kim, J., Lee, S., Brovman, Y. M., Kim, M., Kim, P. & Lee, W. (2014, January). Weak antilocalization and conductance fluctuation in a single crystalline Bi nanowire. *Applied Physics Letters*, *104*(4), 043105. Retrieved 2016-11-09, from http://scitation.aip.org/content/aip/journal/apl/104/4/10.1063/1.4863421 doi: 10.1063/1.4863421

Kitaev, A. Y. (2001). Unpaired Majorana fermions in quantum wires. *Physics-Uspekhi*, *44*(10S), 131. Retrieved 2017-02-20, from http://stacks.iop.org/1063-7869/44/i=10S/a=S29 doi: 10.1070/1063-7869/44/10S/S29

Konopko, L. A., Huber, T. E., Nikolaeva, A. A. & Burceacov, L. A. (2013, June). Quantum Interference of Surface States in Bismuth Nanowires in Transverse Magnetic Fields. *Journal of Low Temperature Physics*, *171*(5-6), 677–684. Retrieved 2016-11-11, from http://link.springer.com/article/10.1007/s10909-012-0850-x doi: 10.1007/s10909-012-0850-x

Konschelle, F., Tokatly, I. V. & Bergeret, F. S. (2015, September). Theory of the spin-galvanic effect and the anomalous phase-shift phi0 in superconductors and Josephson junctions with intrinsic spin-orbit coupling. *Physical Review B*, *92*(12). Retrieved 2017-02-09, from http://arxiv.org/abs/1506.02977 (arXiv: 1506.02977) doi: 10.1103/PhysRevB.92.125443

Koroteev, Y. M., Bihlmayer, G., Gayone, J. E., Chulkov, E. V., Blügel, S., Echenique, P. M. & Hofmann, P. (2004, July). Strong Spin-Orbit Splitting on Bi Surfaces. *Physical Review Letters*, *93*(4), 046403. Retrieved 2016-11-04, from http://link.aps.org/doi/10.1103/PhysRevLett.93.046403 doi: 10.1103/PhysRevLett.93.046403

Kubatkin, S. & Landau, I. (1989). Investigation of Disordered Bismuth and Cadmium Films. *Zh. Eksp. Teor. Fiz.*, *69*(2), 740–756.

Langley, D., Giusti, G., Mayousse, C., Celle, C., Bellet, D. & Simonato, J.-P. (2013). Flexible transparent conductive materials based on silver nanowire networks: a review. *Nanotechnology*, *24*(45), 452001. Retrieved 2016-10-13, from http://stacks.iop.org/0957-4484/24/i=45/a=452001 doi: 10.1088/0957-4484/24/45/452001

Li, C., Guéron, S., Chepelianskii, A. & Bouchiat, H. (2016, September). Full range of proximity effect probed with superconductor/graphene/superconductor junctions. *Physical Review B*, *94*(11), 115405. Retrieved 2017-03-04, from http://link.aps.org/doi/10.1103/PhysRevB.94.115405 doi: 10.1103/PhysRevB.94.115405

Li, C., Kasumov, A., Murani, A., Sengupta, S., Fortuna, F., Napolskii, K., … Bouchiat, H. (2014, Dec). Magnetic field resistant quantum interferences in josephson junctions based on bismuth nanowires. *Phys. Rev. B*, *90*, 245427. Retrieved from http://link.aps.org/doi/10.1103/PhysRevB.90.245427 doi: 10.1103/PhysRevB.90.245427

Li, Y., Zhao, Y., Wu, G. & Zhao, J. (2016, May). Facile and Efficient Synthesis of Bismuth Nanowires for Improved Photocatalytic Activity. *Inorganic Chem-*

istry, *55*(10), 4897–4905. Retrieved 2016-11-09, from http://dx.doi.org/10.1021/acs.inorgchem.6b00423 doi: 10.1021/acs.inorgchem.6b00423

Linder, J. & Robinson, J. W. A. (2015, April). Superconducting Spintronics. *Nature Physics*, *11*(4), 307–315. Retrieved 2016-11-17, from http://arxiv.org/abs/1510.00713 (arXiv: 1510.00713) doi: 10.1038/nphys3242

Liu, Y. & Allen, R. E. (1995, July). Electronic structure of the semimetals Bi and Sb. *Physical Review B*, *52*(3), 1566–1577. Retrieved 2016-11-16, from http://link.aps.org/doi/10.1103/PhysRevB.52.1566 doi: 10.1103/PhysRevB.52.1566

Liu, Y., Haviland, D. B., Nease, B. & Goldman, A. M. (1993, March). Insulator-to-superconductor transition in ultrathin films. *Physical Review B*, *47*(10), 5931–5946. Retrieved 2016-11-11, from http://link.aps.org/doi/10.1103/PhysRevB.47.5931 doi: 10.1103/PhysRevB.47.5931

Mata-Pinzón, Z., Valladares, A. A., Valladares, R. M. & Valladares, A. (2016, January). Superconductivity in Bismuth. A New Look at an Old Problem. *PLoS ONE*, *11*(1). Retrieved 2016-11-09, from http://www.ncbi.nlm.nih.gov/pmc/articles/PMC4729681/ doi: 10.1371/journal.pone.0147645

Matthias, B. T. (1953, May). Superconducting Compounds of Nonsuperconducting Elements. *Physical Review*, *90*(3), 487–487. Retrieved 2016-11-11, from http://link.aps.org/doi/10.1103/PhysRev.90.487 doi: 10.1103/PhysRev.90.487

Matthias, B. T., Jayaraman, A., Geballe, T. H., Andres, K. & Corenzwit, E. (1966, September). Many More Superconducting Bismuth Phases. *Physical Review Letters*, *17*(12), 640–643. Retrieved 2016-11-09, from http://link.aps.org/doi/10.1103/PhysRevLett.17.640 doi: 10.1103/PhysRevLett.17.640

Mironov, S. V., Mel'nikov, A. S. & Buzdin, A. I. (2015, June). Double path interference and magnetic oscillations in Cooper pair transport through a single nanowire. *Physical Review Letters*, *114*(22). Retrieved 2016-11-30, from http://arxiv.org/abs/1411.1626 (arXiv: 1411.1626) doi: 10.1103/PhysRevLett.114.227001

Montambaux, G. (2007, July). Interference pattern of a long diffusive Josephson junction. *arXiv:0707.0411 [cond-mat]*. Retrieved 2017-02-21, from http://arxiv.org/abs/0707.0411 (arXiv: 0707.0411)

Morel, P. & Anderson, P. W. (1962, February). Calculation of the Superconducting State Parameters with Retarded Electron-Phonon Interaction. *Physical Review*, *125*(4), 1263–1271. Retrieved 2016-11-09, from http://link.aps.org/doi/10.1103/PhysRev.125.1263 doi: 10.1103/PhysRev.125.1263

Mourik, V., Zuo, K., Frolov, S. M., Plissard, S. R., Bakkers, E. P. a. M. & Kouwenhoven, L. P. (2012, May). Signatures of Majorana Fermions in Hybrid Superconductor-Semiconductor Nanowire Devices. *Science*, *336*(6084), 1003–1007. Retrieved 2017-02-20, from http://science.sciencemag.org/content/336/6084/1003 doi: 10.1126/science.1222360

Murakami, S. (2006, December). Quantum Spin Hall Effect and Enhanced Magnetic Response by Spin-Orbit Coupling. *Physical Review Letters*, *97*(23), 236805. Retrieved 2017-02-09, from http://link.aps.org/doi/10.1103/PhysRevLett.97.236805 doi: 10.1103/PhysRevLett.97.236805

Navarro-Moratalla, E., Island, J. O., Mañas-Valero, S., Pinilla-Cienfuegos, E., Castellanos-Gomez, A., Quereda, J., … Coronado, E. (2016, March). Enhanced superconductivity in atomically thin TaS2. *Nature Communications*, *7*, 11043. Retrieved 2016-11-10, from http://www.nature.com/ncomms/2016/160317/ncomms11043/full/ncomms11043.html doi: 10.1038/ncomms11043

Nazarov, Y. V. & Blanter, Y. M. (2009). *Quantum Transport: Introduction to Nanoscience* (1edition ed.). Cambridge, UK ; New York: Cambridge University Press.

Nicolay, G., Reinert, F., Hüfner, S. & Blaha, P. (2001, December). Spin-orbit splitting of the L-gap surface state on Au(111) and Ag(111). *Physical Review B*, *65*(3), 033407. Retrieved 2016-11-04, from `http://link.aps.org/doi/10.1103/PhysRevB.65.033407` doi: 10.1103/PhysRevB.65.033407

Oulton, R. F., Sorger, V. J., Zentgraf, T., Ma, R.-M., Gladden, C., Dai, L., … Zhang, X. (2009, October). Plasmon lasers at deep subwavelength scale. *Nature*, *461*(7264), 629–632. Retrieved 2016-10-13, from `http://www.nature.com/nature/journal/v461/n7264/abs/nature08364.html` doi: 10.1038/nature08364

Parish, M. M. & Littlewood, P. B. (2003, November). Non-saturating magnetoresistance in heavily disordered semiconductors. *Nature*, *426*(6963), 162–165. Retrieved 2016-11-25, from `http://www.nature.com/nature/journal/v426/n6963/full/nature02073.html` doi: 10.1038/nature02073

Park, B., Bae, I.-G. & Huh, Y. H. (2016, January). Aligned silver nanowire-based transparent electrodes for engineering polarisation-selective optoelectronics. *Scientific Reports*, *6*, 19485. Retrieved 2016-11-04, from `http://www.nature.com/articles/srep19485` doi: 10.1038/srep19485

Popović, D., Reinert, F., Hüfner, S., Grigoryan, V. G., Springborg, M., Cercellier, H., … Malterre, D. (2005, July). High-resolution photoemission on Ag/Au(111): Spin-orbit splitting and electronic localization of the surface state. *Physical Review B*, *72*(4), 045419. Retrieved 2016-11-04, from `http://link.aps.org/doi/10.1103/PhysRevB.72.045419` doi: 10.1103/PhysRevB.72.045419

Prakash, O., Kumar, A., Thamizhavel, A. & Ramakrishnan, S. (2016, December). Evidence for bulk superconductivity in pure bismuth single crystals at ambient pressure. *Science*, aaf8227. Retrieved 2017-01-13, from `http://science.sciencemag.org/content/early/2016/11/30/science.aaf8227` doi: 10.1126/science.aaf8227

Quay, C. H. L., Weideneder, M., Chiffaudel, Y., Strunk, C. & Aprili, M. (2015, October). Quasiparticle spin resonance and coherence in superconducting aluminium. *Nature Communications*, *6*, 8660. Retrieved 2017-03-07, from `http://www.nature.com/ncomms/2015/151026/ncomms9660/full/ncomms9660.html` doi: 10.1038/ncomms9660

Roberts, B. W. (1976, July). Survey of superconductive materials and critical evaluation of selected properties. *Journal of Physical and Chemical Reference Data*, *5*(3), 581–822. Retrieved 2016-11-10, from `http://scitation.aip.org/content/aip/journal/jpcrd/5/3/10.1063/1.555540` doi: 10.1063/1.555540

Roditchev, D., Brun, C., Serrier-Garcia, L., Cuevas, J. C., Bessa, V. H. L., Milošević, M. V., … Cren, T. (2015, April). Direct observation of Josephson vortex cores. *Nature Physics*, *11*(4), 332–337. Retrieved 2017-02-20, from `http://www.nature.com/nphys/journal/v11/n4/abs/nphys3240.html` doi: 10.1038/nphys3240

Schuster, D. (2007). *Circuit quantum electrodynamics.*

Shim, W., Ham, J., Lee, K.-i., Jeung, W. Y., Johnson, M. & Lee, W. (2009, January). On-Film Formation of Bi Nanowires with Extraordinary Electron Mobility. *Nano Letters*, *9*(1), 18–22. Retrieved 2016-11-09, from `http://dx.doi.org/10.1021/nl8016829` doi: 10.1021/nl8016829

Shklyarevskii, O. I., Duif, A. M., Jansen, A. G. M. & Wyder, P. (1986, August). Superconductivity in Bi observed with point contacts. *Physical Review B*, *34*(3), 1956–1959. Retrieved 2016-11-10, from `http://link.aps.org/doi/10.1103/PhysRevB`

.34.1956 doi: 10.1103/PhysRevB.34.1956

Smith, G. E., Baraff, G. A. & Rowell, J. M. (1964, August). Effective g Factor of Electrons and Holes in Bismuth. *Physical Review*, *135*(4A), A1118–A1124. Retrieved 2016-10-14, from http://link.aps.org/doi/10.1103/PhysRev.135.A1118 doi: 10.1103/PhysRev.135.A1118

Song, J. C. W., Refael, G. & Lee, P. A. (2015, November). Linear magnetoresistance in metals: Guiding center diffusion in a smooth random potential. *Physical Review B*, *92*(18), 180204. Retrieved 2016-11-23, from http://link.aps.org/doi/10.1103/PhysRevB.92.180204 doi: 10.1103/PhysRevB.92.180204

Sun, Z., Enayat, M., Maldonado, A., Lithgow, C., Yelland, E., Peets, D. C., … Wahl, P. (2015, March). Dirac surface states and nature of superconductivity in Noncentrosymmetric BiPd. *Nature Communications*, *6*, 6633. Retrieved 2017-02-10, from http://www.nature.com/ncomms/2015/150330/ncomms7633/full/ncomms7633.html doi: 10.1038/ncomms7633

Takayama, A., Sato, T., Souma, S., Oguchi, T. & Takahashi, T. (2015, February). One-Dimensional Edge States with Giant Spin Splitting in a Bismuth Thin Film. *Physical Review Letters*, *114*(6). Retrieved 2017-02-14, from http://arxiv.org/abs/1502.03197 (arXiv: 1502.03197) doi: 10.1103/PhysRevLett.114.066402

Tian, M., Kumar, N., Chan, M. H. W. & Mallouk, T. E. (2008, July). Evidence of local superconductivity in granular Bi nanowires fabricated by electrodeposition. *Physical Review B*, *78*(4), 045417. Retrieved 2016-11-10, from http://link.aps.org/doi/10.1103/PhysRevB.78.045417 doi: 10.1103/PhysRevB.78.045417

Tian, M., Wang, J., Kumar, N., Han, T., Kobayashi, Y., Liu, Y., … Chan, M. H. W. (2006, December). Observation of Superconductivity in Granular Bi Nanowires Fabricated by Electrodeposition. *Nano Letters*, *6*(12), 2773–2780. Retrieved 2016-11-10, from http://dx.doi.org/10.1021/nl0618041 doi: 10.1021/nl0618041

Tian, M., Wang, J., Ning, W., Mallouk, T. E. & Chan, M. H. W. (2015, March). Surface Superconductivity in Thin Cylindrical Bi Nanowire. *Nano Letters*, *15*(3), 1487–1492. Retrieved 2016-11-10, from http://dx.doi.org/10.1021/nl503398d doi: 10.1021/nl503398d

Tinkham, M. (2004). *Introduction to Superconductivity: Second Edition*. Dover Publications. (Google-Books-ID: k6AO9nRYbioC)

Tkachov, G., Burset, P., Trauzettel, B. & Hankiewicz, E. M. (2015, July). Quantum interference of edge supercurrents in a two-dimensional topological insulator. *Physical Review B*, *92*(4). Retrieved 2016-11-18, from http://arxiv.org/abs/1409.7301 (arXiv: 1409.7301) doi: 10.1103/PhysRevB.92.045408

Trif, M., Golovach, V. N. & Loss, D. (2008, January). Spin dynamics in InAs nanowire quantum dots coupled to a transmission line. *Physical Review B*, *77*(4), 045434. Retrieved 2016-11-22, from http://link.aps.org/doi/10.1103/PhysRevB.77.045434 doi: 10.1103/PhysRevB.77.045434

van Houten, H., Williamson, J. G., Broekaart, M. E. I., Foxon, C. T. & Harris, J. J. (1988, February). Magnetoresistance in a GaAs-${\mathrm{Al}}_{\mathrm{x}}$${\mathrm{Ga}}_{1\mathrm{-}\mathrm{x}}$As heterostructure with double subband occupancy. *Physical Review B*, *37*(5), 2756–2758. Retrieved 2016-10-14, from http://link.aps.org/doi/10.1103/PhysRevB.37.2756 doi: 10.1103/PhysRevB.37.2756

Veldhorst, M., Snelder, M., Hoek, M., Molenaar, C. G., Leusink, D. P., Golubov, A. A., … Brinkman, A. (2013, February). Magnetotransport and induced superconductivity in Bi based three-dimensional topological insulators. *physica status solidi (RRL) – Rapid Research Letters*, *7*(1-2), 26–38. Retrieved 2016-11-23, from `http://onlinelibrary.wiley.com/doi/10.1002/pssr.201206408/abstract` doi: 10.1002/pssr.201206408

Wada, M., Murakami, S., Freimuth, F. & Bihlmayer, G. (2011, March). Well-localized edge states in two-dimensional topological insulators: ultrathin Bi films. *Physical Review B*, *83*(12). Retrieved 2017-02-10, from `http://arxiv.org/abs/1005.3912` (arXiv: 1005.3912) doi: 10.1103/PhysRevB.83.121310

Weitzel, B. & Micklitz, H. (1991, January). Superconductivity in granular systems built from well-defined rhombohedral Bi-clusters: Evidence for Bi-surface superconductivity. *Physical Review Letters*, *66*(3), 385–388. Retrieved 2016-11-10, from `http://link.aps.org/doi/10.1103/PhysRevLett.66.385` doi: 10.1103/PhysRevLett.66.385

Xi, X., Berger, H., Forró, L., Shan, J. & Mak, K. F. (2016, August). Gate tuning of electronic phase transitions in two-dimensional NbSe$_2$. *Physical Review Letters*, *117*(10). Retrieved 2016-11-10, from `http://arxiv.org/abs/1604.03455` (arXiv: 1604.03455) doi: 10.1103/PhysRevLett.117.106801

Yokoyama, T., Eto, M. & Nazarov, Y. V. (2014, May). Anomalous Josephson effect induced by spin-orbit interaction and Zeeman effect in semiconductor nanowires. *Physical Review B*, *89*(19). Retrieved 2017-02-14, from `http://arxiv.org/abs/1402.0305` (arXiv: 1402.0305) doi: 10.1103/PhysRevB.89.195407

Zhou, J., Jin, C., Seol, J. H., Li, X. & Shi, L. (2005, September). Thermoelectric properties of individual electrodeposited bismuth telluride nanowires. *Applied Physics Letters*, *87*(13), 133109. Retrieved 2016-11-17, from `http://scitation.aip.org/content/aip/journal/apl/87/13/10.1063/1.2058217` doi: 10.1063/1.2058217

Zhu, Z., Collaudin, A., Fauqué, B., Kang, W. & Behnia, K. (2012, January). Field-induced polarization of Dirac valleys in bismuth. *Nature Physics*, *8*(1), 89–94. Retrieved 2016-11-17, from `http://www.nature.com/nphys/journal/v8/n1/abs/nphys2111.html` doi: 10.1038/nphys2111

université
PARIS-SACLAY

ÉCOLE DOCTORALE
Physique
en Île-de-France
(EDPIF)

Title : Superconducting proximity effect in monocrystalline bismuth nanowires

Keywords : mesoscopic superconductivity, topoological insulators, bismuth nanowires

Abstract : The superconducting proximity effect is a phenomenon occurring at low temperatures that conveys superconducting properties to a phase coherent normal metal sample connected to superconducting electrodes. It is also a powerful tool in mesoscopic physics because it is sensitive to different transport regimes at low temperatures. In particular, we have used this effect to reveal the special electronic transport properties of single crystal Bi nanowires. In this system, the transport is dominated by surface states. Moreover, the presence of strong spin-orbit coupling in Bi at low dimensions deeply influences its electronic structure : it was predicted that (111) oriented Bi bilayer are insulating in the bulk, but conducting along the edges. This so called Quantum Spin Hall Effect (QSHE), gives rise to counterpropagating chiral edge states, that are protected against disorder as long as time reversal symmetry is present. Through the observation of the resilience of the critical current in several samples at high magnetic field, along with SQUID-like interference pattern at low magnetic field, we showed the existence of supercurrent carrying 1D edge states. The measurement of the current-phase relation using the asymetric SQUID technique on a previously characterized nanowire was realized and further demonstrates that these edge states are ballistic. These findings are consistent with tight-binding simulations that extend the known results for (111) Bi bilayer to nanowire-like system. The addition of an in-plane Zeeman field allows one to observe $0 - \pi$ transitions, thereby revealing spin-splitting induced Andreev level crossings. Finally, microwave spectroscopy measurement of the dynamical susceptibility in this system are initiated, that could reliably demonstrate the property of protection against disorder according to numerical simulations. By exploring Bi at low dimensions, this thesis paves the way towards the exploration of electronic states fully protected from disorder.

Université Paris-Saclay
Espace Technologique / Immeuble Discovery
Route de l'Orme aux Merisiers RD 128 / 91190 Saint-Aubin, France

ÉCOLE DOCTORALE
Physique
en île-de-France
(EDPIF)

Titre : Supraconductivité par effet de proximité dans des nanofils de bismuth monocrystallins

Keywords : supraconductivité mésoscopique, isolants topologiques, nanofils de bismuth

Résumé : La supraconductivité par effet de proximité est un phénomène apparaissant à basse températures qui confère des propriétés supraconductrices à un métal normal cohérent de phase connecté à des électrodes supraconductrices. C'est aussi un outil puissant de la physique mésoscopique, car il est sensible aux différents régimes de transport à basse température. En particulier, nous avons utilisé cet effet afin de révéler les propriétés électroniques spéciales de nanofils de Bi monocrystallins. Dans ce système, le transport est dominé par la surface. De plus, la présence de fort couplage spin-orbite dans le Bi à basse dimension influence profondément sa structure de bande : la bicouche de Bi orienté selon la direction (111) a été prédite d'être isolante dans le volume, mais conductrice sur les bords. Cet effet, appelé l'effet Hall quantique de spin donne lieu a deux états chiraux contra-propageants, qui sont insensibles au désordre tant que la symétrie par renversement du temps est préservée. A travers l'observation de la robustesse du courant critique à fort champ magnétique dans plusieurs échantillons, en même temps que des intérférences de type SQUID à bas champ magnétique, nous avons montré l'existence d'états de bord 1D portant le supercourant. La mesure de la relation courant-phase grace à la technique de SQUID asymétrique sur un nanofil caractérisé auparavant a été réalisée et démontre que ces canaux sont en fait ballistiques. Ces résultats sont compatibles avec des simulations de type liaisons fortes, qui étendent les résultats connus pour la bicouche de Bi (111) aux systèmes de type nanofil. L'ajout d'un champ Zeeman dans le plan permet d'observer des transitions $0-\pi$, révélant ainsi des croisements de niveaux induits par la séparation en spin des états d'Andreev. Enfin, des mesures de la susceptibilité dynamique de ce système via des mesures de spectroscopie micro-onde ont été mises en place, et pourraient démontrer de manière univoque la propriété de protection topologique contre le désordre, d'après nos simulations numériques.

Université Paris-Saclay
Espace Technologique / Immeuble Discovery
Route de l'Orme aux Merisiers RD 128 / 91190 Saint-Aubin, France